

9-24-2015 12:00 AM

Flows in Vibrating Channels

Sahab Zandi, *The University of Western Ontario*

Supervisor: Dr. Jerzy Maciej Floryan, *The University of Western Ontario*

A thesis submitted in partial fulfillment of the requirements for the Master of Engineering
Science degree in Mechanical and Materials Engineering

© Sahab Zandi 2015

Follow this and additional works at: <https://ir.lib.uwo.ca/etd>



Part of the [Mechanical Engineering Commons](#)

Recommended Citation

Zandi, Sahab, "Flows in Vibrating Channels" (2015). *Electronic Thesis and Dissertation Repository*. 3250.
<https://ir.lib.uwo.ca/etd/3250>

This Dissertation/Thesis is brought to you for free and open access by Scholarship@Western. It has been accepted for inclusion in Electronic Thesis and Dissertation Repository by an authorized administrator of Scholarship@Western. For more information, please contact wlsadmin@uwo.ca.

Flows in Vibrating Channels

(Thesis format: Monograph)

by

Sahab Zandi

Graduate Program in Mechanical and Materials Engineering

A thesis submitted in partial fulfillment
of the requirements for the degree of
Master of Engineering Science

The School of Graduate and Postdoctoral Studies
The University of Western Ontario
London, Ontario, Canada

© Sahab Zandi 2015

Abstract

A spectral algorithm based on the immersed boundary conditions (IBC) concept has been developed for the analysis of flows in channels bounded by vibrating walls. The vibrations take the form of travelling waves of arbitrary profile. The algorithm uses a fixed computational domain with the flow domain immersed in its interior. Boundary conditions enter the algorithm in the form of constraints. The spatial discretization uses a Fourier expansion in the stream-wise direction and a Chebyshev expansion in the wall-normal direction. Use of the Galileo transformation converts the unsteady problem into a steady one. An efficient solver which takes advantage of the structure of the coefficient matrix has been used. It is demonstrated that the method can be extended to more extreme geometries using the over-determined formulation. Various tests confirm the spectral accuracy of the algorithm. Pressure losses in these types of channels have been analyzed. Mechanisms of drag generation have been studied. Analytical solutions have been determined in the limit of long wavelength waves and small amplitude waves in order to simplify identification of these mechanisms. The numerical algorithm has also been validated with the help of analytical solutions. Detailed analyses of different cases, i.e. wave propagation along one wall and both walls have been carried out. Different wave profiles have been considered in order to find forms of waves which minimize pressure losses in vibrating channels. The results show dependence of the pressure losses on the phase speed of the waves, with the waves propagating in the downstream direction reducing the pressure gradient required to maintain a fixed flow rate. A drag increase is observed when the waves propagate with a phase speed similar to the flow velocity.

Keywords

Spectral discretization, vibrating walls, immersed boundary conditions method, Navier-Stokes equations, pressure-driven flows, efficient solvers, over-determined formulation, pressure losses, drag reduction, flow control.

Co-Authorship Statement

This dissertation is prepared in the monograph format. Sections 2, 3, and 4 are based on manuscripts that have been previously published or finalized for submission.

Sections 2 and 3: **S. Zandi**, A. Mohammadi & J. M. Floryan, “Spectrally-Accurate Algorithm for the Analysis of Flows in Two-Dimensional Vibrating Channels”, *Journal of Computational Physics* 301 (2015) 425–455, DOI: 10.1016/j.jcp.2015.08.025.

Section 4: **S. Zandi** & J. M. Floryan, “Pressure Losses in Vibrating Channels”, in preparation for submission to the *Journal of Fluid Mechanics*.

Dedication

To my parents and my sister for their endless love, encouragement and support.

Acknowledgments

It is a pleasure to thank the many people who made this thesis possible. I greatly appreciate the unparalleled assistance and encouragement of my supervisor Prof. J. M. Floryan. The completion of this dissertation would not have been possible without his incomparable assistance and invaluable guidance.

I would like to express my gratitude to the members of my advisory committee, Prof. C. Zhang and Prof. A. G. Straatman for their invaluable suggestions and constructive comments.

I would also like to thank all of my colleagues (past and present), Dr. Alireza Mohammadi, Dr. Hadi Vafadar Moradi, Md Nazmus Sakib, Amirreza Seddighi, Seyed Arman Abtahi and Alan Kalbfleisch for their friendship and encouragement. I am particularly grateful to Alireza not only for his insightful scientific comments but also because of support and motivation I have received from him.

Words are not enough to express my gratitude towards my family. Without the unconditional love, encouragement, tremendous patience and understanding of parents, Soheila and Masoud, and my sister, Saghar, I would not have been able to accomplish my goals. I wish I could show them how much I love and appreciate them.

Finally I would like to mention that the support from The University of Western Ontario and the Natural Sciences and Engineering Research Council (NSERC) of Canada is gratefully acknowledged.

Table of Contents

Abstract	ii
Co-Authorship Statement	iii
Dedication	iv
Acknowledgments	v
Table of Contents	vi
List of Figures	viii
List of Appendices	xiv
List of Abbreviations, Symbols, Nomenclature	xv
Section 1	1
1 Introduction	1
Section 2	6
2 Formulation of the Problem	6
2.1 Problem Formulation	6
Section 3	9
3 Spectrally-Accurate Algorithm	9
3.1 Field Equations Suitable for the Numerical Solution	9
3.2 Discretization of the field Equations	12
3.3 Discretization of the Boundary Conditions	17
3.4 Evaluation of the Pressure Field	21
3.5 Solution Process	24
3.6 The Linear Solver.....	26
3.7 Performance of the Algorithm	28
3.8 The Over-Determined Formulation.....	40
Section 4	49

4 Pressure Losses in Vibrating Channels.....	49
4.1 Determination of Forces.....	49
4.2 Mechanics of Drag Generation	51
4.3 Waves with Small Amplitudes.....	62
4.4 Arbitrary Waves	67
4.4.1 Sinusoidal Waves on One Wall.....	67
4.4.2 Sinusoidal Waves on Both Walls.....	75
4.4.3 Different Wave Profiles	77
Section 5	81
5 Conclusions	81
References	83
Appendices	88
Curriculum Vitae	99

List of Figures

Figure 2.1: Sketch of the flow domain.	7
Figure 3.1: Structure of the coefficient matrix L for $N_M = 5$ and $N_T = 31$. Black identifies the non-zero elements. Figure 3.1A displays the coefficient matrix before the re-arrangement whereas Figure 3.1B displays its structure after the re-arrangement (see Subsection 3.6). ..	28
Figure 3.2: Variations of the error Er (see Eq. (3.65)) for the wave shape described by Eq. (3.64) with the wave number $\alpha = 1$, Reynolds number $Re = 5$, phase speed $c = 1.3$ and wave amplitudes A shown on the graph.	30
Figure 3.3: Distribution of the real part of $D\Phi^{(n)}$ as a function of y for higher Fourier modes ($n > 15$) in the region very close to the lower wall for the wave shape described by Eq. (3.64) with the wave number $\alpha = 5$, amplitude $A = 0.05$, Reynolds number $Re = 5$ and phase speed $c = 1.3$ obtained using $N_M = 20$ Fourier modes and $N_T = 80$ Chebyshev polynomials.	31
Figure 3.4: Variations of the Chebyshev norm of $D\Phi^{(n)}$ as a function of the Fourier mode number determined for the wave shape described by Eq. (3.64) with the wave number $\alpha = 1$ and with different wave amplitudes A . Calculations were carried out for Reynolds number $Re = 5$ and wave phase speed $c = 1.3$ using $N_M = 20$ Fourier modes and $N_T = 80$ Chebyshev polynomials.	32
Figure 3.5: Variations of the $\ u_L\ _\infty, \ v_L + ch'_L\ _\infty$ norms as functions of the total number of Fourier modes N_M used in the calculation for the wave shape described by Eq. (3.64) with the wave number $\alpha = 1$ and with different amplitudes A . Calculations have been carried out for Reynolds number $Re = 5$ and phase speed $c = 1.3$ using $N_T = 80$ Chebyshev polynomials.	33
Figure 3.6: Distributions of the error in the enforcement of the boundary conditions along the vibrating wall, i.e. u_L and $v_L + ch'_L$, for the wave with shape described by Eq. (3.64) with the wave number $\alpha = 5$ and amplitude $A = 0.05$. Calculations were carried out for Reynolds	

number $Re = 5$ and phase speed $c = 1.3$ using $N_M = 20$ Fourier modes and $N_T = 80$ Chebyshev polynomials. 34

Figure 3.7: Fourier spectra of the error in the enforcement of the boundary conditions along the vibrating wall, i.e. Eq. (3.68), for the wave with shape described by Eq. (3.64) with wave number $\alpha = 5$ and amplitude $A = 0.05$. Calculations were carried out for the Reynolds number $Re = 5$ and phase speed $c = 1.3$ using $N_M = 20$ Fourier modes and $N_T = 80$ Chebyshev polynomials. The reader should note the absence of the first 20 Fourier modes. 35

Figure 3.8: Fourier spectra of $u_L(x)$ for the wave shape described by Eq. (3.64) with the amplitude $A = 0.04$ and wavelength $\lambda_x = 2\pi/3$. Solutions have been obtained in case A using $N_M = 10$ Fourier modes, in case B using $N_M = 20$ Fourier modes, and in case C using $N_M = 30$ Fourier modes. Calculations were carried out with Reynolds number $Re = 5$ and phase speed $c = 1.3$ using $N_T = 80$ Chebyshev polynomials. 36

Figure 3.9: Variations of the $\|u_L\|_\infty$ norm for the wave shape described by Eq. (3.64) as a function of the wave amplitude A for selected wave numbers α . Dashed and solid lines correspond to results obtained with $N_M = 15$ and $N_M = 20$ Fourier modes, respectively. Calculations have been carried out for the Reynolds number $Re = 5$ and phase speed $c = 1.3$ using $N_T = 80$ Chebyshev polynomials. 37

Figure 3.10: Variations of the $\|u_L\|_\infty$ norm for the wave shape described by Eq. (3.64) as a function of the wave number α for selected amplitudes A . Dashed and solid lines correspond to results obtained with $N_M = 15$ and $N_M = 20$ Fourier modes, respectively. Calculations have been carried out with Reynolds number $Re = 5$ and phase speed $c = 1.3$ using $N_T = 80$ Chebyshev polynomials. 38

Figure 3.11: Variations of the $\|u_L\|_\infty$ norm for the wave shape described by Eq. (3.64) with the wave number $\alpha = 2$, the amplitude $A = 0.06$ and the phase speed $c = 1.3$ as a function of Reynolds number computed using different numbers of Fourier modes N_M and $N_T = 80$ Chebyshev polynomials. 39

Figure 3.12: Variations of the $\|u_L\|_\infty$ norm for the wave shape described by Eq. (3.64) with amplitude $A = 0.04$, wave number $\alpha = 2$ and Reynolds number $Re = 5$ as a function of the

phase speed c determined using different numbers of Fourier modes N_M and $N_T = 80$ Chebyshev polynomials. 40

Figure 3.13: Structure of the coefficient matrix L_0 for $N_M = 5$, $M_M = 10$ and $N_T = 31$ resulting from the use of the over-determined IBC method. Black identifies the non-zero elements. Figure 3.13A displays the coefficient matrix before the re-arrangement whereas Figure 3.13B displays its structure after the re-arrangement (see Subsection 3.8). 43

Figure 3.14: Fourier spectra of the error in the enforcement of the boundary conditions along the vibrating wall (see Eq. (3.68)) for the wave with shape described by Eq. (3.64) with wave number $\alpha = 5$ and amplitude $A = 0.05$. Calculations have been carried out for $Re = 5$ and $c = 1.3$ using $N_M = 20$ Fourier modes, $M_M = 30$ boundary relations and $N_T = 80$ Chebyshev polynomials. 44

Figure 3.15: Variations of the $\|u_L\|_\infty$ norm as a function of the wave amplitude A for the wave shape described by Eq. (3.64) with wave number $\alpha = 2$ and phase speed $c = 1.3$ for $Re = 1$ resulting from the use of the over-determined method. Dashed and dotted lines correspond to results obtained using the SVD and QR factorization techniques, respectively. Calculations have been carried out using $N_M = 20$ Fourier modes and $N_T = 100$ Chebyshev polynomials. 45

Figure 3.16: Variations of the $\|u_L\|_\infty$ norm as a function of the wave amplitude A for the wave shape described by Eq. (3.64) with phase speed $c = 1.3$ and wave number $\alpha = 2$ for $Re = 1$ determined using the over-determined formulation. Dashed and dotted lines correspond to results obtained using SVD and QR factorization techniques, respectively. Calculations have been carried out using $N_T = 100$ Chebyshev polynomials and different numbers N_M of Fourier modes and an optimal number M_M of boundary relations. 46

Figure 3.17: Plots of the velocity field in a vibrating channel whose geometry is described by Eq. (3.75) with $\alpha = 1$, $A = 0.02$, $Re = 5$ and $c = 1.3$. The black dot represents a reference point moving with the phase speed. Figures 3.17 A–D correspond to times $t = t_0$, $t = t_0 + T/4$, $t = t_0 + T/2$, $t = t_0 + 3T/4$, respectively, where $T = 2\pi/\alpha c$ stands for a period of vibration and t_0 denotes the time when the black dot was located at $X = 0$. $N_T = 120$ Chebyshev polynomials and $N_M = 60$ Fourier modes have been used in the calculations.

.....	47
Figure 4.1: Variations of the critical wave speed of the long wavelength waves as a function of the wave amplitude A for waves with profile described by Eq. (4.7).	59
Figure 4.2: Variations of forces acting on the fluid at the lower wall in the limit of $\alpha \rightarrow 0$ as functions of the wave speed c for the wave form described by Eq. (4.7) with: (A) $A = 0.1$; (B) $A = 0.3$; (C) $A = 0.5$. Solid, dashed, dash-dotted lines and lines with circles on them correspond to $Re * F_{x,visc}$, $Re * F_{x,form}$, $Re * F_{x,inter}$, and $Re * F_{x,total}(= Re * (F_{x,visc} + F_{x,form} + F_{x,inter}))$, respectively.	60
Figure 4.3: Variations of the norm $\ dp_1/dx\ _{max}$ as a function of the wave number α for the flow Reynolds numbers $Re = 0.1$ (dashed lines) and $Re = 200$ (solid lines) and phase speed $c = 1.3$	62
Figure 4.4: Variations of $Re(dp_1/dx)$ as a function of phase speed c for the wave form defined by (4.45) for selected α and A . Dashed and solid lines correspond to $Re = 1$ and $Re = 200$, respectively.	68
Figure 4.5: Variations of $Re(dp_1/dx)$ as a function of the phase speed c for the wave profile defined by (4.45) with $Re = 200$ and $A = 0.03$, and different wave numbers α	69
Figure 4.6: Variations of forces per unit length of the channel acting on the fluid at (A) the lower and (B) the upper walls as functions of the wave speed c for the wave form described by Eq. (4.45) with Reynolds number $Re = 200$, wave amplitude $A = 0.03$, and wave number $\alpha = 2$. Dashed, dotted, and solid lines correspond to viscous forces $(F_{x,visc}, G_{x,visc})$, pressure forces $(F_{x,pres}, G_{x,pres})$, and total forces $(F_{x,total} = F_{x,visc} + F_{x,pres}, G_{x,total} = G_{x,visc} + G_{x,pres})$, respectively.	70
Figure 4.7: Plots of velocity field in a vibrating channel whose geometry is described by Eq. (4.45) with $\alpha = 2$, $A = 0.03$, $Re = 200$. Figures 4.7 A–C correspond to $c = 0$, $c = 0.58$, and $c = 1$, respectively.	70

Figure 4.8: Plots of $Re * p_T$ in a vibrating channel whose geometry is described by Eq. (4.45) with $\alpha = 2$, $A = 0.03$, $Re = 1$. Figures 4.8 A–C correspond to $c = 0$, $c = 0.58$, and $c = 1$, respectively. 72

Figure 4.9: Plots of $Re * p_T$ in a vibrating channel whose geometry is described by Eq. (4.45) with $\alpha = 2$, $A = 0.03$, $Re = 200$. Figures 4.9 A–C correspond to $c = 0$, $c = 0.58$, and $c = 1$, respectively. 72

Figure 4.10: Variations of $Re(dp_1/dx)$ as a function of the phase speed c and the wave number α for the wave form defined by (6.1) with $A = 0.03$ and: (A) $Re = 1$; (B) $Re = 100$; (C) $Re = 200$ 73

Figure 4.11: Distributions of (A) the x -component of the shear force $f_{x,visc}$ and (B) the x -component of the form force $f_{x,form}$ and (C) the x -component of the interaction force $f_{x,inter}$ acting on the fluid at the lower wall and (D) the x -component of the shear force $g_{x,visc}$ acting on the fluid at the upper wall for the wave profile described by (4.45) with $A = 0.03$, $Re = 1$, and $\alpha = 2$. The solid, dashed, and dotted lines correspond to $c = -5$, $c = 0$, and $c = 5$, respectively. Thick and thin lines identify local and mean values, respectively. 73

Figure 4.12: Distributions of (A) the x -component of the shear force $f_{x,visc}$ and (B) the x -component of the form force $f_{x,form}$ and (C) the x -component of the interaction force $f_{x,inter}$ acting on the fluid at the lower wall and (D) the x -component of the shear force $g_{x,visc}$ acting on the fluid at the upper wall for the wave profile described by (4.45) with $A = 0.03$, $Re = 100$, and $\alpha = 2$. The solid, dashed, and dotted lines correspond to $c = -5$, $c = 0$, and $c = 5$, respectively. Thick and thin lines identify local and mean values, respectively. 74

Figure 4.13: Distributions of (A) the x -component of the shear force $f_{x,visc}$ and (B) the x -component of the form force $f_{x,form}$ and (C) the x -component of the interaction force $f_{x,inter}$ acting on the fluid at the lower wall and (D) the x -component of the shear force $g_{x,visc}$ acting on the fluid at the upper wall for the wave profile described by (4.45) with $A = 0.03$, $Re = 200$, and $\alpha = 2$. The solid, dashed, and dotted lines correspond to $c = -5$, $c = 0$, and $c = 5$, respectively. Thick and thin lines identify local and mean values, respectively. 74

Figure 4.14: Variations of mean values of local forces as functions of the wave speed c . Conditions in Figures 4.14 A–C are the same as conditions in Figures 4.11–4.13, respectively. Solid, dashed, dotted, and dash-dotted lines and line with circles on it correspond to $f_{x,v,m}$, $f_{x,f,m}$, $f_{x,i,m}$, $g_{x,v,m}$, and $f_{x,t,m}(= f_{x,v,m} + f_{x,f,m} + f_{x,i,m} + g_{x,v,m})$, respectively. 75

Figure 4.15: Variations of $Re(dp_1/dx)$ as a function of the phase shift ϕ for the wave form defined by (4.45) for selected α and A and: (A) $c = -5$; (B) $c = 0$; (C) $c = 5$. Dashed and solid lines correspond to $Re = 1$ and $Re = 200$, respectively. 76

Figure 4.16: Variations of $Re(dp_1/dx)$ as a function of phase shift ϕ and the phase speed c for the wave form defined by (4.45) with $\alpha = 3$, $A = 0.03$ for $Re = 1$ 77

Figure 4.17: Triangular wave profiles used in the study. A , λ and $\alpha = 2\pi/\lambda$ denote the wave amplitude, wavelength and wave number, respectively. 77

Figure 4.18: Variations of $Re(dp_1/dx)$ as a function of a/λ for waves with triangular profiles (see Figure 4.17) for selected α and A with: (A) $c = -5$; (B) $c = 0$; (C) $c = 5$. Dashed and solid lines correspond to $Re = 1$ and $Re = 200$, respectively. The reader may note that $a < \lambda/2$ corresponds to the waves tilting upstream. 78

Figure 4.19: Channel with triangular waves at both walls. The parametrization of each wave is the same as in Figure 4.17. 79

Figure 4.20: Variations of $Re(dp_1/dx)$ as a function of the phase shift ϕ for wave forms defined in Figure 4.19 for $\alpha = 1$, $A = 0.01$, $a/\lambda = 0.1$ and: (A) $c = -5$; (B) $c = 0$; (C) $c = 5$. Cases A and B correspond to configurations A and B in Figure 4.19. Dashed and solid lines correspond to $Re = 1$ and $Re = 200$, respectively. 79

List of Appendices

Appendix A: Evaluation of the inner products.....	88
Appendix B: Definitions of functions used in Subsection 4.2.....	93
Appendix C: Definitions of functions used in Subsection 4.3.....	95
Appendix D: Copyright release.....	97

List of Abbreviations, Symbols, Nomenclature

Abbreviations

VOF	Volume of fluid
MAC	Marker and Cell
IBC	Immersed boundary conditions
RHS	Right-hand side
RF	Relaxation factor
FFT	Fast Fourier transform
SVD	Singular value decomposition

Nomenclature used in Section 2

h	Half of the average channel height
Re	The flow Reynolds number
u_{max}	Maximum of the streamwise velocity component of the reference flow
(t, X, Y)	Time-dependent physical coordinate system
ρ, ν	Density and kinematic viscosity
u_T, v_T	Velocity components in the x - and y - directions
u_0, v_0	Reference velocity components in the x - and y - directions

u_1, v_1	Modification velocity components in the x - and y - directions
p_T, p_0, p_1	Total pressure, reference pressure and pressure modification
Q_0, Ψ_0	Flow rate and stream function of the reference flow
Y_U, Y_L	Shapes of the waves at the upper and lower walls in the physical coordinate system
h_U, h_L	Functions used to define Shapes of the waves at the upper and lower walls in the physical coordinate system
$H_U^{(n)}, H_L^{(n)}$	Fourier coefficients of wave geometries at the upper and lower walls in the physical coordinate system
c	Wave speed
α	Wave number
N_A	Number of Fourier modes used in description of wave geometry
y_t, y_b	Upper and lower extremities of the flow domain
h'_U, h'_L	Derivative of h'_U, h'_L with respect to time
Q	The net flow rate through vibrating channel
U, L	Upper and lower walls (as subscript)
0,1	Reference flow and flow modifications (as subscript)
*	Complex conjugate (as superscript)
$\langle n \rangle$	Fourier mode (as superscript)

Nomenclature used in Section 3

(x, y)	Coordinate system after Galileo transformation
y_U, y_L	Shapes of the waves at the upper and the lower walls in the transformed coordinate system
Ψ_T, Ψ_0, Ψ_1	Total, reference and modification stream functions
U_T, V_T	Velocity components in the x - and y - directions in the moving reference frame
U_0, V_0	Reference velocity components in the x - and y - directions in the moving reference frame
U_1, V_1	Modification velocity components in the x - and y - directions in the moving reference frame
P_0, P_1	Total pressure, reference pressure and pressure modification in the moving reference frame
$\bar{\Psi}_T, \bar{\Psi}_1$	Total and modification stream functions in the moving reference frame
\bar{Q}	The flow rate through vibrating channel in the moving reference frame
(x, \hat{y})	Computational coordinate system
Γ	Constant of coordinate transformation for the IBC method
$\widehat{u_1 u_1}, \widehat{u_1 v_1}, \widehat{v_1 v_1}$	Velocity products in the physical space
\hat{y}_U, \hat{y}_L	Shapes of the waves at the upper and the lower walls in the computational coordinate system
$A_U^{(n)}, A_L^{(n)}$	Fourier coefficients of waves geometries at the upper and lower walls in the computational domain

$\Phi^{(n)}$	Modal function in the Fourier expansion representing the stream function
N_M	Number of Fourier modes used for discretization in the x -direction
$\widehat{uu}^{(n)}, \widehat{uv}^{(n)}, \widehat{vv}^{(n)}$	Modal function of velocity products $\widehat{u_1 u_1}, \widehat{u_1 v_1}, \widehat{v_1 v_1}$
D	Derivative with respect to the transverse direction
$G_k^{(n)}$	Chebyshev coefficients in Chebyshev expansion of $\Phi^{(n)}$
T_k	k th Chebyshev polynomials of the first kind
N_T	Order of Chebyshev polynomials used for discretization of the modal functions in the \hat{y} -direction
$G\widehat{uu}_k^{(n)}, G\widehat{uv}_k^{(n)}, G\widehat{vv}_k^{(n)}$	Coefficients of the Chebyshev expansions of the modal functions in the Fourier expansions representing velocity products
i	Imaginary unit
ω	Weight function
$\langle f, g \rangle$	Inner product of two functions
$F_U^{(n)}, F_L^{(n)}$	Coefficients of Fourier expansions for $u_0(\hat{y}_U(x))$ and $u_0(\hat{y}_L(x))$
$(w_U)_k^{(m)}, (w_L)_k^{(m)}$	Coefficients of the Fourier expansions for the Chebyshev polynomials evaluated at the upper and lower walls
$(d_U)_k^{(m)}, (d_L)_k^{(m)}$	Coefficients of the Fourier expansions for the first derivative of the Chebyshev polynomials evaluated at the upper and lower walls
N_S	Number of Fourier modes used to describe the Chebyshev polynomials and their derivatives evaluated at the upper and lower walls

N_f	Number of Fourier modes in the Fourier expansions for the modification velocity components evaluated along the walls
$\theta_U^{(n)}, \theta_L^{(n)}$	Coefficients of Fourier expansions for $\Psi_{0,U}(x)$ and $\Psi_{0,L}(x)$
A_p	Pressure gradient correction
$p_1^{(n)}$	Modal functions of Fourier expansions for the periodic part of the pressure modification
$\Pi_k^{(n)}$	Coefficients of Chebyshev expansions for $p_1^{(n)}(\hat{y})$
k	Iteration number
N_x	Number of grids along x -direction in (x, \hat{y}) plane
$\mathbf{L}, \mathbf{x}, \mathbf{R}$	Coefficients matrix, vector of unknowns and right-hand side vector for problem in (x, \hat{y}) plane
$\mathbf{A}, \mathbf{B}, \mathbf{C}, \mathbf{D}$	Different sections of the rearranged coefficients matrix \mathbf{L}
\mathbf{x}_1	Contains unknowns $G_k^{(n)}$ for $n \in \langle -N_M, N_M \rangle$ and $k \in \langle 4, N_T - 1 \rangle$
\mathbf{x}_2	Contains unknowns $G_k^{(n)}$ for $n \in \langle -N_M, N_M \rangle$ and $k \in \langle 0, 3 \rangle$
A	Wave amplitude
$\ D\Phi^{(n)}\ _\omega$	Chebyshev norm for $D\Phi^{(n)}$
$\ u_L\ _\infty, \ v_L + ch'_L\ _\infty$	L_∞ norm of error in the enforcement of the boundary conditions
$U_L^{(n)}, V_L^{(n)}$	Coefficients of the Fourier expansions for $\ u_L\ _\infty$ and $\ v_L + ch'_L\ _\infty$
λ	wavelength
M_M	Number of Fourier modes used for boundary constraints in over-

	determined formulation
L_0, x, z_0	Coefficients matrix, vector of unknowns and right-hand side vector for problem in (x, \hat{y}) plane using over-determined formulation
H, K_0	Different sections of the rearranged coefficients matrix L_0
L_0^+	Generalized inverse of L_0
Q, R, R_1	Matrices used in QR factorization method
U, S, V, S_1	Matrices used in SVD method
A, B, C_0, D_0	Different sections of the rearranged coefficients matrix L_0
t_0	Time when the black dot was located at $X = 0$ in Figure 3.17
T	Period of vibration
H	Conjugate transpose (as superscript)
T	Transpose (as superscript)

Nomenclature used in Section 4

n_U, n_L	Outwards normal unit vectors at the upper and lower walls
$n_{U,x}, n_{U,y}$	Components of n_U
$n_{L,x}, n_{L,y}$	Components of n_L
$\vec{\sigma}$	Stress tensor
$\sigma_{xx}, \sigma_{xy}, \sigma_{yx}, \sigma_{yy}$	Components of stress tensor
f, g	Distribution of the local forces action on the fluid at the lower and upper walls

f_x, f_y, g_x, g_y	Components of f and g
$f_{x,visc}, F_{x,visc}$	Distribution of the x -component of local and total viscous forces per unit length of the channel acting on the fluid at the lower wall
$f_{x,pres}, F_{x,pres}$	Distribution of the x -component of local and total pressure forces per unit length of the channel acting on the fluid at the lower wall
$f_{y,visc}, F_{y,visc}$	Distribution of the y -component of local and total viscous forces per unit length of the channel acting on the fluid at the lower wall
$f_{y,pres}, F_{y,pres}$	Distribution of the y -component of local and total pressure forces per unit length of the channel acting on the fluid at the lower wall
$g_{x,visc}, G_{x,visc}$	Distribution of the x -component of local and total viscous forces per unit length of the channel acting on the fluid at the upper wall
$g_{x,pres}, G_{x,pres}$	Distribution of the x -component of local and total pressure forces per unit length of the channel acting on the fluid at the upper wall
$g_{y,visc}, G_{y,visc}$	Distribution of the y -component of local and total viscous forces per unit length of the channel acting on the fluid at the upper wall
$g_{y,pres}, G_{y,pres}$	Distribution of the y -component of local and total pressure forces per unit length of the channel acting on the fluid at the upper wall
ξ, η	Horizontal and vertical coordinates in the transformed coordinate system
F_1, \dots, F_8	Coefficients given in Appendix B
G_1, \dots, G_3	Coefficients given in Appendix B
H_1, \dots, H_{11}	Coefficients given in Appendix B
$\tilde{u}_0, \tilde{u}_1, \tilde{v}_0, \tilde{v}_1, \tilde{p}_{-1}, \tilde{p}_0$	Terms in asymptotic expansions for velocity components and pressure in the limit of $\alpha \rightarrow 0$

\tilde{p}_{-1}	Normalized \tilde{p}_{-1} at a stationary point in the laboratory frame, say at $X = 0$
$F_{x,form}, F_{x,inter}$	Pressure form drag and pressure interaction drag acting on the fluid at the lower wall
$F_{x,total}$	Sum of $F_{x,visc}$ and $F_{x,pres}$
c_{cr}	Critical wave speed at which drag can be eliminated in the limit of $\alpha \rightarrow 0$
$c_{cr,v}$	Critical wave speed at which $F_{x,visc}$ reaches zero in the limit of $\alpha \rightarrow 0$
$c_{cr,pf}$	Critical wave speed at which $F_{x,form}$ reaches zero in the limit of $\alpha \rightarrow 0$
$c_{cr,pi}$	Critical wave speed at which $F_{x,inter}$ reaches zero in the limit of $\alpha \rightarrow 0$
$c_{cr,tot}$	Critical wave speed at which $F_{x,total}$ reaches zero in the limit of $\alpha \rightarrow 0$
γ	Lower bound of interval for integration
$\left\ \frac{dp_1}{dx} \right\ _{max}$	L_∞ norm of error in pressure gradient correction obtained using asymptotic and complete solutions
I_1, \dots, I_8	Coefficients given in Appendix C
L_1, \dots, L_3	Coefficients given in Appendix C
g_1, \dots, g_3	Coefficients given in Appendix C
$\tilde{u}_0, \tilde{u}_1, \tilde{u}_2, \tilde{v}_0, \tilde{v}_1, \tilde{v}_2$	Terms in asymptotic expansions for velocity components and pressure in the limit of $A \rightarrow 0$

$\tilde{p}_0, \tilde{p}_1, \tilde{p}_2$	
$\tilde{u}_1^{(1)}(\eta), \tilde{v}_1^{(1)}(\eta)$	Modal functions of $\tilde{u}_1(\xi, \eta), \tilde{v}_1(\xi, \eta), \tilde{p}_1(\xi, \eta)$
$\tilde{p}_1^{(1)}(\eta)$	
$\tilde{u}_1^{(-1)}(\eta), \tilde{v}_1^{(-1)}(\eta)$	Complex conjugates of $\tilde{u}_1^{(1)}(\eta), \tilde{v}_1^{(1)}(\eta), \tilde{p}_1^{(1)}(\eta)$
$\tilde{p}_1^{(-1)}(\eta)$	
$\tilde{u}_2^{(n)}(\eta), \tilde{v}_2^{(n)}(\eta)$	Modal functions of $\tilde{u}_2(\xi, \eta), \tilde{v}_2(\xi, \eta), \tilde{p}_2(\xi, \eta)$
$\tilde{p}_2^{(n)}(\eta)$	
A_{pc}	Contribution of $\tilde{p}_2(\xi, \eta)$ to the pressure gradient correction
$Re(dp_1/dx)$	Pressure gradient correction multiplied by Reynolds number
$f_{x,v}, f_{x,f}, f_{x,i}, g_{x,v}$	Short forms for $f_{x,visc}, f_{x,form}, f_{x,inter}, g_{x,visc}$
$f_{x,v,m}, f_{x,f,m}, f_{x,i,m}$	Mean values for $f_{x,visc}, f_{x,form}, f_{x,inter}, g_{x,visc}$, and $f_{x,total}$
$g_{x,v,m}, f_{x,t,m}$	
ϕ	Phase shift between the upper and lower waves
a, b	Lengths specified in Figure 4.17
a, c	Asymptotic and complete solutions (as subscript)

Section 1

1 Introduction

Determination of flows in channels with vibrating walls requires solution of the moving boundary problem. This class of problems has been of interest in many application areas including surface waves, interfacial problems, phase change problems, flow induced vibrations, peristaltic and pulsatile flows in the esophagus and flows through the vasculatures due to cardiac actions to name just a few. The available algorithms can be classified either as Lagrangian or Eulerian [1]. Mixed methods involving combinations of the Lagrangian and Eulerian techniques have also been pursued [1]. Each fluid element is followed individually in the Lagrangian algorithms resulting in a need for a coordinate system that moves with the fluid. Mesh tangling leads to significant restrictions on the overall applicability of these methods [1]. The Eulerian algorithms rely on the coordinate systems that are stationary in a laboratory frame of reference or may move in a prescribed manner. Such algorithms can be divided for convenience into the fixed grid methods, the adaptive grid methods and various mapping methods.

In the fixed grid methods, grid is fixed in the solution domain and locations of the moving boundaries are tracked using either surface [1, 2] or volume tracking procedures [1, 3]. The surface tracking relies on a set of points whose motion is tracked during the solution process allowing precise identification of the boundary locations; these boundaries are represented as a set of interpolated curves [3, 4]. The volume tracking algorithms on the other hand work by reconstructing the boundary whenever necessary instead of storing the boundary locations. The presence of a convenient marker within a computational cell and its quantity form the basis of the various reconstruction methodologies. Different versions of volume tracking algorithms exist, e.g. VOF (Volume of Fluid) [5], MAC (Marker and Cell) [6] and Level Set [7, 8] methods. These methods are based on the standard spatial discretization schemes with the low-order spatial accuracy which is consistent with the diffused boundary locations resulting from

the tracking procedures.

The adaptive grid methods use numerical mappings to adjust grids at each time step so that one of the grid lines always overlaps with the boundary location. The computational costs are very high due to grid reconstruction at each time step, e.g. the grid construction consumed about 75% of the computational cost for the problem discussed in [9]. The spatial discretization technique has a smaller effect on the overall computational costs. The need for high solution accuracy leads to numerous challenges as the total error has contributions from the grid generation as well as from the spatial and temporal discretizations of the field equations. Use of mappings based of the Schwarz-Christoffel transformation provides access to higher accuracy at a reasonable cost as one need to determine mapping parameters only and these parameters can be determined with the near spectral accuracy [10–12]. Analytical mapping of the irregular physical domain into a rectangular computational domain can help in improving the accuracy at the cost of increased complexity of the field equations [13, 14]. However, such mappings are available only for a limited class of geometries [1] and reconstruction of the coefficient matrix during each time step can add to the overall computational cost by a substantial margin [14–20].

The immersed or fictitious boundaries represent a new concept which has potential to increase the accuracy while maintaining the computational efficiency. This concept is due to Peskin [21] and has been developed in the context of cardiac dynamics; see [22, 23] for reviews. The common limitation is the spatial accuracy, as most of these methods are based on either low-order finite-difference, or finite-volume or finite-element techniques [22–26]. The second, less known limitation is the use of the local fictitious forces required to enforce the no-slip and no-penetration conditions. These forces locally affect the flow physics and this may lead to the incorrect estimates of derivatives of flow quantities, i.e. misrepresentation of the local wall shear. This problem is likely to be more pronounced in the case of methods with high spatial accuracy.

Spectral methods provide the lowest error for the spatial discretization but are generally limited to solution domains with regular geometries. The first spectrally accurate

implementation of the immersed boundary concept is given in [27]. We shall refer to this method as the immersed boundary conditions (IBC) method in the rest of this presentation. IBC method relies on a purely formal construction of boundary constraints in order to generate the required closing relations. Spatial discretization relies on the Fourier and Chebyshev expansions in the stream-wise and normal-to-the-wall directions, respectively, and, thus, provides the ability to reach the machine level accuracy. The method could be viewed as a gridless as it uses global basis functions which span the complete solution domain. The construction of boundary constraints relies on the representation of the physical boundaries in the spectral space and nullifying the relevant Fourier modes. The method involves two types of Fourier expansions, one for the field equations and one for the boundary relations and, thus, the rate of convergence of both expansions determines the limits of its applicability. The programming effort associated with accounting for geometry changes is reduced to specification of a set of Fourier coefficients which need to be provided as an input. The additional attractiveness of the IBC method is associated with the precise mathematical formalism, high accuracy and sharp identification of the location of time-dependent physical boundaries. The method has been extended to two-dimensional unsteady problems [28], moving boundary problems involving Laplace [29] and biharmonic [30] operators, the complete Navier-Stokes system [31], to operators involving different classes of non-Newtonian fluids [32, 33], to three-dimensional operators [34, 35] as well as to operators expressed in cylindrical coordinate systems [36]. Its accuracy has been improved through the use of the over-determined formulation [37]. The efficiency has been increased by an order of magnitude through the development of specialized solvers which account for the special structure of the coefficient matrix [38, 39]. The method has been used to identify the laminar drag-reducing grooves [16–20] and to study effects of various grooves on the flow stability [40–46].

This work is focused on the development of an efficient algorithm suitable for analysis of changes of the pressure gradient required to drive a specified flow rate through a vibrating channel. Vibrations in the form of travelling waves, such as those found in the peristaltic pumping, are of primary interest. The identification of the most effective forms of such waves is of interest.

Vibrating boundaries can be found in many engineering and biological applications. Effects of surface vibrations on fluid flows are very important in different fields and have been of interest for a long time. Fundamental knowledge on flows through vibrating conduits is important in various applications and is widely used in developing strategies for flow control.

We shall refer to the flow in vibrating channels as peristaltic flow. Peristaltic action is a vital process and can be seen in many parts of the human body. An example of this is the use of peristaltic action to push urine from the kidney to the bladder. Peristaltic action also helps to push food forward through the gullet. Bile moving from the gall-bladder to the duodenum is caused by peristaltic action as well as ovum movement in the fallopian tube. Along with biological processes, peristaltic action can be used for industrial processes. One example of this is in the design of roller pumps which allows for the pumping of fluids without pump components coming into contact with the fluid.

The numerous applications of peristaltic flow have led to many studies on the topic. The use of deformed conduit walls for flow control has been studied by several researchers [47] and has been extensively employed to control turbulent flows. Along with flow control, features that affect the reduction of friction have been studied to allow an optimal shape of deformation to be determined [48-55].

In peristaltic flow, the fluid motions are affected by the vibrations of flexible walls caused by the propagation of a traveling wave along the channel. Numerous studies have been published about this topic. The first study of non-steady peristaltic transport in a finite-length tube for an arbitrary wave is described in [56]. A novel pumping mechanism in a microchannel with moving wall contractions is studied in [57]. Analysis of peristaltic flow for Jeffrey fluid within a circular tube is provided by [58]. A model which involves slip effects on the peristaltic flow of a Maxwellian fluid is given by [59]. Analysis of effects of peristaltic waves in a curved channel on non-Newtonian fluid flows is provided by [60]. A more detailed analysis of peristaltic flow within an asymmetric channel is discussed in [61].

Most of the studies mentioned above are focused on pumping effects of peristaltic action. In the current work such pumping effects have not been studied; however, peristaltic action has been considered as a drag-reducing tool and effects of vibrations on drag reduction have been analyzed. It has been assumed that fluid is Newtonian, incompressible and viscous while flow remains laminar in the whole problem.

This work is focused on the problem of channel flow subjected to transverse solid wall vibrations in the form of travelling waves of arbitrary profiles. The analysis has primarily been motivated by the lack of information on the response of fluid flows to surface vibrations, and the possibility of using these vibrations in different aspects of flow control. Waves propagate along a channel where a laminar flow is driven by a constant pressure gradient. The waves' effect is assessed by determining the additional pressure gradient required to maintain the same mass flow rate as in the smooth channel. The Reynolds number is kept sufficiently small as computational cost increases with increasing its magnitude. Variations and distributions of surface forces acting on the fluid are investigated and mechanism of drag generation is studied with the help of analytical solutions in the limit of long wavelength waves and small amplitude waves. The critical wave speeds and their effects are illustrated. Unusual responses of flow are observed when wave propagates with speed similar to the flow velocity. The responses were also studied in [62]. This work provides a more thorough explanation for these responses and illustrates effects of these responses on drag variations. Also, effects of vibrations in the form of waves of different profiles, which have not been studied previously, are of primary interest.

This dissertation is organized as follows: Section 2 presents formulation of the problem; Section 3 presents a spectrally-accurate algorithm that is specifically developed for the analysis of flows in vibrating channels; Section 4 is devoted to parametrization of features of wave geometry that is relevant to pressure losses. Details of variations of drag in the limit of long wavelength waves and small amplitude waves as well as the analyses of mechanisms contributing to the formation of drag are given in this Section; Section 5 summarizes the main conclusions.

Section 2

2 Formulation of the Problem

This Section is focused on the development of physical formulation of the problem. Subsection 2.1 provides the physical formulation.

2.1 Problem Formulation

We shall use formulation described in Zandi *et al.* (2015). Consider steady, two-dimensional flow of a fluid confined in a channel bounded by two parallel walls extending to $\pm\infty$ in the X -direction and placed at a distance $2h$ apart as shown in Figure 2.1. The flow is driven in the positive X -direction by a pressure gradient resulting in the velocity and pressure fields, and the flow rate of the form

$$\mathbf{v}_0(X, Y) = (1 - Y^2, 0), \quad p_0(X, Y) = -2X/Re, \quad \Psi_0 = Y - \frac{Y^3}{3} + \frac{2}{3}, \quad Q_0 = \frac{4}{3} \quad (2.1)$$

where $\mathbf{v}_0 = (u_0, v_0)$ denotes the velocity vector scaled with the maximum of the X -velocity u_{max} , p_0 stands for the pressure scaled with ρu_{max}^2 where ρ stands for the density, Ψ_0 stands for the stream function, Q_0 denotes the flow rate, the Reynolds number is defined as $Re = u_{max}h/\nu$ where ν stands for the kinematic viscosity, and h has been used as the length scale. The flow is modified by imposing wall vibrations in the form of travelling waves with known amplitudes. The resulting time-dependent channel geometry is described as

$$Y_U(t, X) = 1 + h_U(X - ct) = 1 + \sum_{n=-N_A}^{n=N_A} H_U^{(n)} e^{in\alpha(X-ct)}, \quad (2.2a)$$

$$Y_L(t, X) = -1 + h_L(X - ct) = -1 + \sum_{n=-N_A}^{n=N_A} H_L^{(n)} e^{in\alpha(X-ct)} \quad (2.2b)$$

where h_U and h_L are known, the subscripts L and U refer to the lower and upper walls, respectively, N_A denotes the number of Fourier modes required to describe the shape of the wave, c and α denote the wave phase speed and its wave number, respectively, and

$H_U^{(-n)} = H_U^{(n)*}$ and $H_L^{(-n)} = H_L^{(n)*}$ are the reality conditions with $*$ denoting the complex conjugates. Our interests are in waves that do not affect the mean channel opening and, thus, coefficients of modes zero in (2.2) have been set to zero, i.e. $H_U^{(0)} = H_L^{(0)} = 0$. In general, (2.2) cannot accurately describe shapes with discontinuities due to the Gibbs phenomenon [63–65], but the error can be controlled by using a proper filtering method [66].

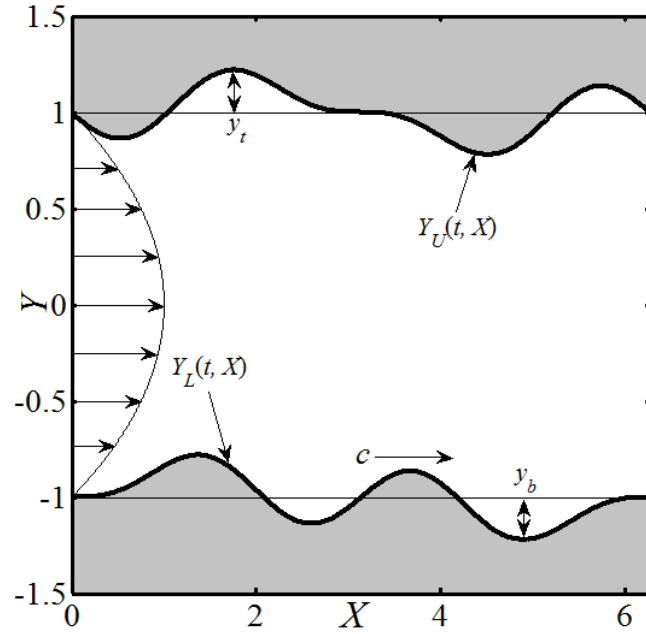


Figure 2.1: Sketch of the flow domain.

We shall represent all flow quantities as sums of the reference flow and the vibration-induced modifications, i.e.

$$\begin{aligned} u_T(t, X, Y) &= u_0(Y) + u_1(t, X, Y), & v_T(t, X, Y) &= v_1(t, X, Y), \\ p_T(t, X, Y) &= p_0(X) + p_1(t, X, Y). \end{aligned} \tag{2.3}$$

In the above, (u_T, v_T) and p_T denote the complete velocity and pressure fields, respectively, and (u_1, v_1) and p_1 denote the velocity and pressure field modifications caused by the vibrations, respectively. Substitution of (2.3) into the Navier-Stokes and continuity equations and use of (2.1) lead to the field equations for the flow modifications of the form

$$\frac{\partial u_1}{\partial t} + (u_0 + u_1) \frac{\partial u_1}{\partial X} + v_1 \frac{du_0}{dY} + v_1 \frac{\partial u_1}{\partial Y} = -\frac{\partial p_1}{\partial X} + Re^{-1} \left(\frac{\partial^2 u_1}{\partial X^2} + \frac{\partial^2 u_1}{\partial Y^2} \right), \quad (2.4a)$$

$$\frac{\partial v_1}{\partial t} + (u_0 + u_1) \frac{\partial v_1}{\partial X} + v_1 \frac{\partial v_1}{\partial Y} = -\frac{\partial p_1}{\partial Y} + Re^{-1} \left(\frac{\partial^2 v_1}{\partial X^2} + \frac{\partial^2 v_1}{\partial Y^2} \right), \quad (2.4b)$$

$$\frac{\partial u_1}{\partial X} + \frac{\partial v_1}{\partial Y} = 0 \quad (2.4c)$$

subject to boundary conditions of the form

$$u_T(t, X, Y_U(t, X)) = 0, \quad v_T(t, X, Y_U(t, X)) = \frac{\partial Y_U(t, X)}{\partial t} = -ch'_U(X - ct), \quad (2.4d,e)$$

$$u_T(t, X, Y_L(t, X)) = 0, \quad v_T(t, X, Y_L(t, X)) = \frac{\partial Y_L(t, X)}{\partial t} = -ch'_L(X - ct) \quad (2.4f,g)$$

where h/u_{max} has been used as the time scale, ∂ denotes partial differentiation and prime denotes differentiation with respect to the argument. We are interested in determining if the surface vibrations can lead to a reduction of the pressure gradient required to maintain the specified flow rate. Accordingly, we impose the mass flow rate constraint of the form

$$Q(t, X)|_{mean} = \left(\int_{Y_L(t, x)}^{Y_U(t, x)} u(t, X, Y) dY \right) \Big|_{mean} = \frac{4}{3}, \quad (2.4h)$$

i.e. the net flow rate through the vibrating channel at any X -location must be the same as through the stationary reference channel.

Section 3

3 Spectrally-Accurate Algorithm

Subsection 3.1 describes the form of the field equation suitable for the numerical solution. Subsection 3.2 discusses discretization of the field equations. Subsection 3.3 provides a description of the proper construction of the boundary constraints. Subsection 3.4 illustrates the evaluation of the pressure field. Subsection 3.5 discusses the iterative solution procedure. Subsection 3.6 describes the linear solver used in the solution. Subsection 3.7 provides descriptions of various numerical tests which demonstrate the spectral accuracy of the algorithm. Subsection 3.8 describes improvements resulting from the over-determined formulation.

3.1 Field Equations Suitable for the Numerical Solution

We shall use solution method described in Zandi *et al.* (2015). Introduction of the Galileo transformation of the form

$$y = Y, \quad x = X - ct, \quad (3.1)$$

converts the unsteady problem (2.4) into the steady problem of the form

$$(u_0 + u_1 - c) \frac{\partial u_1}{\partial x} + v_1 \frac{du_0}{dy} + v_1 \frac{\partial u_1}{\partial y} = -\frac{\partial p_1}{\partial x} + Re^{-1} \left(\frac{\partial^2 u_1}{\partial x^2} + \frac{\partial^2 u_1}{\partial y^2} \right), \quad (3.2a)$$

$$(u_0 + u_1 - c) \frac{\partial v_1}{\partial x} + v_1 \frac{\partial v_1}{\partial y} = -\frac{\partial p_1}{\partial y} + Re^{-1} \left(\frac{\partial^2 v_1}{\partial x^2} + \frac{\partial^2 v_1}{\partial y^2} \right), \quad (3.2b)$$

$$\frac{\partial u_1}{\partial x} + \frac{\partial v_1}{\partial y} = 0, \quad (3.2c)$$

$$y = y_U(x): \quad u_1 = -u_0, \quad v_1 = -ch'_U(x), \quad (3.2d)$$

$$y = y_L(x): \quad u_1 = -u_0, \quad v_1 = -ch'_L(x), \quad (3.2e)$$

$$Q(x)|_{mean} = \left(\int_{y_L(x)}^{y_U(x)} u_T(x, y) dy \right) \Big|_{mean} = \frac{4}{3} \quad (3.2f)$$

where the locations of the boundaries are given as

$$y_U(x) = 1 + h_U(x) = 1 + \sum_{n=-N_A}^{n=N_A} H_U^{(n)} e^{inax}, \quad (3.3a)$$

$$y_L(x) = -1 + h_L(x) = -1 + \sum_{n=-N_A}^{n=N_A} H_L^{(n)} e^{inax}. \quad (3.3b)$$

The reader may note that $Q(x)$ is a periodic function of x and its mean value corresponds to the 0th mode of its Fourier expansion. The continuity equation can be satisfied identically by introducing functions Ψ_T, Ψ_1 defined as

$$u_T = u_0 + u_1 = \frac{\partial \Psi_T}{\partial y} = \frac{d\Psi_0}{dy} + \frac{\partial \Psi_1}{\partial y}, \quad v_T = v_1 = -\frac{\partial \Psi_1}{\partial x}, \quad \Psi_T = \Psi_0 + \Psi_1. \quad (3.4)$$

Pressure can be eliminated by taking the derivative of (3.2a) with respect to y and the derivative of (3.2b) with respect to x and subtracting the resulting equations. The use of (3.4) leads to the flow problem of the form

$$-Re^{-1} \nabla^2 (\nabla^2 \Psi_1) + (u_0 - c) \frac{\partial}{\partial x} \nabla^2 \Psi_1 - \frac{d^2 u_0}{dy^2} \frac{\partial \Psi_1}{\partial x} = - \left(\frac{\partial \Psi_1}{\partial y} \frac{\partial}{\partial x} - \frac{\partial \Psi_1}{\partial x} \frac{\partial}{\partial y} \right) \nabla^2 \Psi_1, \quad (3.5)$$

$$y = y_U(x): \quad \frac{\partial \Psi_1}{\partial y} = -u_0, \quad \frac{\partial \Psi_1}{\partial x} = ch'_U(x), \quad (3.6a,b)$$

$$y = y_L(x): \quad \frac{\partial \Psi_1}{\partial y} = -u_0, \quad \frac{\partial \Psi_1}{\partial x} = ch'_L(x), \quad (3.7a,b)$$

$$Q(x)|_{mean} = [(\Psi_0 + \Psi_1)|_{y_U(x)} - (\Psi_0 + \Psi_1)|_{y_L(x)}] \Big|_{mean} = \frac{4}{3}. \quad (3.8)$$

Condition (3.7b) can be written in a different form by noting that variations of Ψ_T along the lower wall can be expressed as

$$d\Psi_{T,L} = \left(\frac{\partial \Psi_T}{\partial x} dx + \frac{\partial \Psi_T}{\partial y} dy \right) \Big|_{y_L(x)} = c \frac{dy_L}{dx} dx. \quad (3.9)$$

Integration along the wall results in

$$\Psi_{T,L}(x) = c[y_L(x) - y_L(x_0)] \quad (3.10)$$

where the constant of integration has been selected by assuming that $\Psi_{T,L}(x_0) = 0$ with x_0 representing an arbitrary point on the lower wall. A similar analysis carried out for the upper wall leads to an alternative form of (3.6b), i.e.

$$\Psi_{T,U}(x) = c[y_U(x) - y_L(x_0)] - 2c + \frac{4}{3} \quad (3.11)$$

where the constraint (3.8) has been used in order to determine the integration constant. Equations (3.5), (3.6a), (3.7a), (3.10) and (3.11) represent an alternative problem formulation. This particular formulation is better suited for the theoretical analysis while (3.5)–(3.8) is better suited for the numerical solution [20].

The flow problem can be formulated using the velocity with respect to the moving reference frame, i.e. $U_1 = u_1 - c$, $V_1 = v_1$. Equations (3.2) assume the following form

$$(U_0 + U_1) \frac{\partial U_1}{\partial x} + V_1 \frac{dU_0}{dy} + V_1 \frac{\partial U_1}{\partial y} = -\frac{\partial P_1}{\partial x} + Re^{-1} \left(\frac{\partial^2 U_1}{\partial x^2} + \frac{\partial^2 U_1}{\partial y^2} \right), \quad (3.12a)$$

$$(U_0 + U_1) \frac{\partial V_1}{\partial x} + V_1 \frac{\partial V_1}{\partial y} = -\frac{\partial P_1}{\partial y} + Re^{-1} \left(\frac{\partial^2 V_1}{\partial x^2} + \frac{\partial^2 V_1}{\partial y^2} \right), \quad (3.12b)$$

$$\frac{\partial U_1}{\partial x} + \frac{\partial V_1}{\partial y} = 0, \quad (3.12c)$$

$$y = y_U(x): \quad U_1 = -U_0 - c, \quad V_1 = -ch'_U(x), \quad (3.12d)$$

$$y = y_L(x): \quad U_1 = -U_0 - c, \quad V_1 = -ch'_L(x), \quad (3.12e)$$

$$\bar{Q}(x)|_{mean} = \left(\int_{y_L(x)}^{y_U(x)} U(x, y) dy \right) \Big|_{mean} = \frac{4}{3} - 2c. \quad (3.12f)$$

Introducing the functions $\bar{\Psi}_T = \Psi_0 + \bar{\Psi}_1$ defined as

$$U_T = U_0 + U_1 = \frac{d\Psi_0}{dy} + \frac{\partial \bar{\Psi}_1}{\partial y}, \quad V_T = V_1 = -\frac{\partial \bar{\Psi}_1}{\partial x} \quad (3.13)$$

and eliminating the pressure lead to the flow problem of the form

$$-Re^{-1}\nabla^2(\nabla^2\bar{\Psi}_1) + U_0 \frac{\partial}{\partial x} \nabla^2\bar{\Psi}_1 - \frac{d^2U_0}{dy^2} \frac{\partial\bar{\Psi}_1}{\partial x} = -\left(\frac{\partial\bar{\Psi}_1}{\partial y} \frac{\partial}{\partial x} - \frac{\partial\bar{\Psi}_1}{\partial x} \frac{\partial}{\partial y}\right) \nabla^2\bar{\Psi}_1, \quad (3.14a)$$

$$y = y_U(x): \quad \frac{\partial\bar{\Psi}_1}{\partial y} = -c - u_0, \quad \frac{\partial\bar{\Psi}_1}{\partial x} = ch'_U(x), \quad (3.14b)$$

$$y = y_L(x): \quad \frac{\partial\bar{\Psi}_1}{\partial y} = -c - u_0, \quad \frac{\partial\bar{\Psi}_1}{\partial x} = ch'_L(x), \quad (3.14c)$$

$$[(\Psi_0 + \bar{\Psi}_1)|_{y_U(x)} - (\Psi_0 + \bar{\Psi}_1)|_{y_L(x)}]_{mean} = \frac{4}{3} - 2c. \quad (3.14d)$$

Evaluation of $\bar{\Psi}_T$ at the walls results in

$$\bar{\Psi}_T(y_U) = \frac{4}{3} - 2c, \quad \bar{\Psi}_T(y_L) = 0. \quad (3.14e)$$

We shall address the dependence of the algorithm performance on the formulation used later in this presentation.

3.2 Discretization of the field Equations

We seek a spectrally accurate solution to the above problem with the channel geometry expressed by (3.3). The immersed boundary conditions (IBC) method is used to deal with the complexities associated with the irregular geometry. In this method, a fixed computational domain with the physical domain immersed in its interior is used and the flow boundary conditions are replaced with constraints. The size of the computational domain in the y -direction cannot be smaller than $-1 - y_b < y < 1 + y_t$ where y_t, y_b denote locations of extremities of the upper and lower walls, respectively (see Figure 2.1). The locations of these extremities determine the minimum y -expanse of the computational domain which needs to be used and a transformation of the form

$$\hat{y} = 2 \left[\frac{y - (1 + y_t)}{y_t + y_b + 2} \right] + 1, \quad (3.15)$$

maps this domain into $[-1, 1]$ to facilitate the use of the standard form of Chebyshev polynomials. The flow problem expressed using \hat{y} rather than the y coordinate has the form

$$-Re^{-1} \left(\Gamma^4 \frac{\partial^4 \psi_1}{\partial \hat{y}^4} + 2\Gamma^2 \frac{\partial^2}{\partial x^2} \left(\frac{\partial^2 \psi_1}{\partial \hat{y}^2} \right) + \frac{\partial^4 \psi_1}{\partial x^4} \right) +$$

$$(u_0 - c) \frac{\partial}{\partial x} \left(\frac{\partial^2 \psi_1}{\partial x^2} + \Gamma^2 \frac{\partial^2 \psi_1}{\partial \hat{y}^2} \right) - \Gamma^2 \frac{d^2 u_0}{d\hat{y}^2} \frac{\partial \psi_1}{\partial x} = \quad (3.16a)$$

$$- \Gamma \frac{\partial}{\partial \hat{y}} \left(\frac{\partial u_1 \widehat{u_1}}{\partial x} + \Gamma \frac{\partial u_1 \widehat{v_1}}{\partial \hat{y}} \right) + \frac{\partial}{\partial x} \left(\frac{\partial u_1 \widehat{v_1}}{\partial x} + \Gamma \frac{\partial v_1 \widehat{v_1}}{\partial \hat{y}} \right),$$

$$\hat{y} = \hat{y}_U(x): \quad \frac{\partial \psi_1}{\partial \hat{y}} = -\Gamma^{-1} u_0, \quad (3.16b)$$

$$\Psi_{T,U}(x) = c\Gamma^{-1}[\hat{y}_U(x) - \hat{y}_L(x_0)] - 2c + \frac{4}{3} \text{ or } \frac{\partial \psi_1}{\partial x} = c\Gamma^{-1} \frac{d\hat{y}_U(x)}{dx}, \quad (3.16c)$$

$$\hat{y} = \hat{y}_L(x): \quad \frac{\partial \psi_1}{\partial \hat{y}} = -\Gamma^{-1} u_0, \quad (3.16d)$$

$$\Psi_{T,L}(x) = c\Gamma^{-1}[\hat{y}_L(x) - \hat{y}_L(x_0)] \quad \text{or } \frac{\partial \psi_1}{\partial x} = c\Gamma^{-1} \frac{d\hat{y}_L(x)}{dx}, \quad (3.16e)$$

$$Q(x)|_{mean} = [(\Psi_0 + \Psi_1)|_{\hat{y}_U(x)} - (\Psi_0 + \Psi_1)|_{\hat{y}_L(x)}]|_{mean} = \frac{4}{3}, \quad (3.16f)$$

$$\hat{y}_U = \sum_{n=-N_A}^{N_A} A_U^{(n)} e^{inax} \text{ with } A_U^{(0)} = 1 - \Gamma y_t, \quad A_U^{(n)} = \Gamma H_U^{(n)} \text{ for } n \neq 0, \quad (3.16g)$$

$$\hat{y}_L = \sum_{n=-N_A}^{N_A} A_L^{(n)} e^{inax} \text{ with } A_L^{(0)} = 1 + \Gamma(-2 - y_t), A_L^{(n)} = \Gamma H_L^{(n)} \text{ for } n \neq 0 \quad (3.16h)$$

where $\Gamma = \frac{d\hat{y}}{dy} = \frac{2}{y_t + y_b + 2}$ and $A_U^{(n)} = A_U^{(-n)*}$ and $A_L^{(n)} = A_L^{(-n)*}$ represent the reality conditions. We shall keep two forms of (3.16c) and (3.16e) as the use of boundary conditions in the form of derivatives is more computationally efficient (see Subsection 3.5) while the specification of Ψ_T along the walls is more convenient for the enforcement of the flow rate constraint [20].

The x -periodicity of the solution domain suggests expressing the unknown Ψ_1 as a Fourier expansion of the form

$$\Psi_1(x, \hat{y}) = \sum_{n=-\infty}^{\infty} \Phi^{(n)}(\hat{y}) e^{in\alpha x} \approx \sum_{n=-N_M}^{N_M} \Phi^{(n)}(\hat{y}) e^{in\alpha x} \quad (3.17)$$

where $\Phi^{(n)}$ are the modal functions satisfying the reality conditions of the form $\Phi^{(n)} = \Phi^{(-n)*}$ and N_M is the number of Fourier modes used in the solution.

The discretization of the field equations begins with the substitution of (3.17) into (3.16a). The resulting equation can be expressed in terms of a system of modal equations if the nonlinear terms on the right hand side of (3.16a) can be expressed as Fourier expansions. Such expansions can be written in the following form

$$\begin{aligned} [\widehat{u_1 u_1}, \widehat{u_1 v_1}, \widehat{v_1 v_1}](x, \hat{y}) &= \sum_{n=-\infty}^{\infty} [\widehat{u u}^{(n)}, \widehat{u v}^{(n)}, \widehat{v v}^{(n)}](\hat{y}) e^{in\alpha x} \approx \\ &\sum_{n=-N_M}^{N_M} [\widehat{u u}^{(n)}, \widehat{u v}^{(n)}, \widehat{v v}^{(n)}](\hat{y}) e^{in\alpha x}. \end{aligned} \quad (3.18)$$

Substitution of (3.18) into (3.16a) and separation of Fourier modes lead to the modal equations of the form

$$\begin{aligned} -Re^{-1}[\Gamma^4 D^4 - 2\Gamma^2(n\alpha)^2 D^2 + (n\alpha)^4] \Phi^{(n)} + \\ in\alpha(u_0 - c)[\Gamma^2 D^2 - (n\alpha)^2] \Phi^{(n)} - in\alpha \Gamma^2 D^2 u_0 \Phi^{(n)} = \\ -\Gamma D[in\alpha \widehat{u u}^{(n)} + \Gamma D \widehat{u v}^{(n)}] + in\alpha[in\alpha \widehat{u v}^{(n)} + \Gamma D \widehat{v v}^{(n)}] \end{aligned} \quad (3.19)$$

where $-N_M < n < N_M$, $D = d/d\hat{y}$. These equations are coupled explicitly through the nonlinear terms and coupled implicitly through the boundary conditions which we shall discuss later.

The differential system (3.19) needs to be converted into an algebraic system before the actual computations can begin. Discretization begins with representing $\Phi^{(n)}$ in terms of Chebyshev expansions of the form

$$\Phi^{(n)}(\hat{y}) = \sum_{k=0}^{\infty} G_k^{(n)} T_k(\hat{y}) \approx \sum_{k=0}^{N_T-1} G_k^{(n)} T_k(\hat{y}) \quad (3.20)$$

where T_k denotes the Chebyshev polynomial of the first kind of k^{th} order, $G_k^{(n)}$ denotes the unknown coefficients of the expansion and N_T denotes the number of Chebyshev polynomials retained in the solution. The nonlinear terms on the right hand side of (3.19) have to be expressed in terms of similar expansions, i.e.

$$\begin{aligned} [\widehat{u}\widehat{u}^{(n)}, \widehat{u}\widehat{v}^{(n)}, \widehat{v}\widehat{v}^{(n)}](\hat{y}) &= \sum_{k=0}^{\infty} [G\widehat{u}\widehat{u}_k^{(n)}, G\widehat{u}\widehat{v}_k^{(n)}, G\widehat{v}\widehat{v}_k^{(n)}] T_k(\hat{y}) \approx \\ &\sum_{k=0}^{N_T-1} [G\widehat{u}\widehat{u}_k^{(n)}, G\widehat{u}\widehat{v}_k^{(n)}, G\widehat{v}\widehat{v}_k^{(n)}] T_k(\hat{y}) \end{aligned} \quad (3.21)$$

where $G\widehat{u}\widehat{u}_k^{(n)}, G\widehat{u}\widehat{v}_k^{(n)}, G\widehat{v}\widehat{v}_k^{(n)}$ are considered to be known. The reader may note that these coefficients need to be recomputed at the beginning of each iteration. We shall address this issue later in the presentation. The derivatives of $\Phi^{(n)}(\hat{y})$ are evaluated using the formula

$$D^n \Phi^{(n)} = \sum_{k=0}^{N_T-1} G_k^{(n)} D^n T_k(\hat{y}). \quad (3.22)$$

Similar formulae are used for the \hat{y} derivatives of $\widehat{u}\widehat{u}^{(n)}, \widehat{u}\widehat{v}^{(n)}, \widehat{v}\widehat{v}^{(n)}$. Substitution of (3.20)–(3.21) into (3.19) and the use of (3.22) results in modal equations of the form

$$\begin{aligned} \sum_{k=0}^{N_T-1} \{ -Re^{-1} [\Gamma^4 D^4 T_k - 2\Gamma^2 (n\alpha)^2 D^2 T_k + (n\alpha)^4 T_k] + \\ in\alpha [\Gamma^2 (u_0 - c) D^2 T_k - (n\alpha)^2 (u_0 - c) T_k] - \\ in\alpha \Gamma^2 (D^2 u_0) T_k \} G_k^{(n)} = \\ \sum_{k=0}^{N_T-1} [-in\alpha \Gamma G\widehat{u}\widehat{u}_k^{(n)} D T_k - \Gamma^2 G\widehat{u}\widehat{v}_k^{(n)} D^2 T_k - \\ (n\alpha)^2 G\widehat{u}\widehat{v}_k^{(n)} T_k + in\alpha \Gamma G\widehat{v}\widehat{v}_k^{(n)} D T_k]. \end{aligned} \quad (3.23)$$

The Galerkin procedure is used to extract algebraic equations for $G_k^{(n)}$. This procedure involves projecting the residuum on the basis functions and setting it to zero and, in practical terms, involves multiplying (3.23) by $T_j(\hat{y})$, $j = [0, N_T-1]$ and integrating with the weight factor of $\omega = (1 - \hat{y}^2)^{-1/2}$. This process results in

$$\begin{aligned}
& \sum_{k=0}^{N_T-1} \{ -Re^{-1} [\Gamma^4 \langle T_j, D^4 T_k \rangle - 2\Gamma^2 (n\alpha)^2 \langle T_j, D^2 T_k \rangle + (n\alpha)^4 \langle T_j, T_k \rangle] + \\
& \quad in\alpha [\Gamma^2 \langle T_j, (u_0 - c) D^2 T_k \rangle - (n\alpha)^2 \langle T_j, (u_0 - c) T_k \rangle] - \\
& \quad in\alpha \Gamma^2 \langle T_j, (D^2 u_0) T_k \rangle \} G_k^{(n)} = \\
& \quad -in\alpha \Gamma \sum_{k=0}^{N_T-1} G \widehat{u}_k^{(n)} \langle T_j, D T_k \rangle - \Gamma^2 \sum_{k=0}^{N_T-1} G \widehat{u}_k^{(n)} \langle T_j, D^2 T_k \rangle - \\
& \quad (n\alpha)^2 \sum_{k=0}^{N_T-1} G \widehat{u}_k^{(n)} \langle T_j, T_k \rangle + in\alpha \Gamma \sum_{k=0}^{N_T-1} G \widehat{v}_k^{(n)} \langle T_j, D T_k \rangle,
\end{aligned} \tag{3.24}$$

where $\langle \cdot \rangle$ denotes the inner product defined as $\langle f(\hat{y}), g(\hat{y}) \rangle = \int_{-1}^1 f(\hat{y}) g(\hat{y}) \omega(\hat{y}) d\hat{y}$. The use of the orthogonality properties of the form [66, 67]

$$\langle T_j, T_k \rangle = \begin{cases} 0 & \text{for } j \neq k, \\ \pi & \text{for } j = k = 0, \\ \pi/2 & \text{for } j = k > 0, \end{cases} \tag{3.25}$$

permits analytical evaluation of the integrals. In order to take full advantage of the orthogonality properties, the derivatives of the Chebyshev polynomials in (3.24) are expressed in terms of the Chebyshev polynomials by taking advantage of the following relations [66, 67]

$$T_0(\hat{y}) = 1, \quad T_1(\hat{y}) = \hat{y}, \quad T_{k+1}(\hat{y}) = 2\hat{y}T_k(\hat{y}) - T_{k-1}(\hat{y}) \tag{3.26a}$$

$$D^n T_0(\hat{y}) = 0 \text{ for } n \geq 1, \quad D T_1(\hat{y}) = 1, \quad D^n T_1(\hat{y}) = 0 \text{ for } n \geq 2 \tag{3.26b}$$

$$D^n T_{k+1}(\hat{y}) = 2n D^{n-1} T_k(\hat{y}) + 2\hat{y} D^n T_k(\hat{y}) - D^n T_{k-1}(\hat{y}) \text{ for } n \geq 1.$$

A detailed description of the evaluation of various inner products appearing in Eq. (3.24) is given in Appendix A.

3.3 Discretization of the Boundary Conditions

The boundary conditions are imposed using the tau method [66]. Four equations resulting from the discretization of each modal equation (i.e. Eq. (3.24)) and corresponding to the highest Chebyshev polynomials are eliminated in order to provide space for the inclusion of the boundary conditions. The development of the form of these conditions suitable for their implementation in the IBC method is described below.

The flow boundary conditions are to be enforced along the walls located inside the computational domain. We shall discuss the construction of constraints equivalent to these conditions using the upper wall as an example. The construction for the lower wall is similar. Boundary conditions (3.16b,c) require the evaluation of u_0 along the wall whose shape is defined by (3.16g). The resulting values of u_0 represent periodic functions of x and can be expressed in terms of a Fourier series as

$$u_0(\hat{y}_U(x)) = \sum_{n=-2N_A}^{2N_A} F_U^{(n)} e^{inax} \quad (3.27)$$

where the summation extends over the range $-2N_A \leq n \leq 2N_A$ due to the quadratic dependence of u_0 on \hat{y}_U . Since $y = a\hat{y} + b$ where $a = \Gamma^{-1}$, $b = -\Gamma^{-1} + 1 + y_t$, it follows that

$$u_0(\hat{y}_U(x)) = -a^2 \hat{y}_U^2(x) - 2ab\hat{y}_U(x) + 1 - b^2. \quad (3.28)$$

The first term on the RHS of (3.28) has the form

$$a^2 \hat{y}_U^2(x) = a^2 \sum_{n=-2N_A}^{2N_A} \sum_{m=-N_A}^{N_A} A_U^{(m)} A_U^{(n-m)} e^{inax} \quad (3.29)$$

where the non-zero values of $A_U^{(k)}$ occur only for $|k| \leq N_A$. Substitution of (3.16g), (3.28) and (3.29) into (3.27) and separating Fourier modes gives explicit expressions for the expansion coefficients of the form

$$F_U^{(n)} = -a^2 \sum_{m=-N_A}^{N_A} A_U^{(m)} A_U^{(n-m)} - 2abA_U^{(n)} \quad 1 \leq |n| \leq 2N_A, \quad (3.30a)$$

$$F_U^{(0)} = -a^2 \sum_{m=-N_A}^{N_A} A_U^{(m)} A_U^{(m)*} - 2abA_U^{(0)} + (1 - b^2) \quad n = 0 \quad (3.30b)$$

The unknowns appearing in (3.16b,c) need to be expressed using their discretized form i.e.

$$\frac{\partial \psi_1}{\partial \hat{y}} = \sum_{n=-N_M}^{N_M} D \Phi^{(n)}(\hat{y}_U(x)) e^{in\alpha x} = \quad (3.31a)$$

$$\sum_{n=-N_M}^{N_M} \sum_{k=0}^{N_T-1} G_k^{(n)} D T_k(\hat{y}_U(x)) e^{in\alpha x},$$

$$\frac{\partial \psi_1}{\partial x} = \sum_{n=-N_M}^{N_M} in\alpha \Phi^{(n)}(\hat{y}_U(x)) e^{in\alpha x} = \quad (3.31b)$$

$$\sum_{n=-N_M}^{N_M} \sum_{k=0}^{N_T-1} in\alpha G_k^{(n)} T_k(\hat{y}_U(x)) e^{in\alpha x}$$

where the derivative form of (3.16c) has been used as this is computationally more efficient. Chebyshev polynomials and their derivatives evaluated along the wall represent periodic functions of x and, thus, can be expressed using Fourier expansions of the form

$$T_k(\hat{y}_U(x)) = \sum_{m=-N_s}^{N_s} (w_U)_k^{(m)} e^{im\alpha x}, D T_k(\hat{y}_U(x)) = \sum_{m=-N_s}^{N_s} (d_U)_k^{(m)} e^{im\alpha x} \quad (3.32a,b)$$

where $N_s = (N_T - 1)N_A$ as the highest order polynomials being used are of order $\hat{y}_U^{N_T-1}$. The evaluation of coefficients of the above expansions begins by noting that

$$(w_U)_0^{(0)} = 1, (w_U)_0^{(m)} = 0 \text{ for } |m| \geq 1, (w_U)_1^{(m)} = A_U^{(m)} \text{ for } |m| \geq 0. \quad (3.33a,b)$$

Coefficients with higher indices can be determined using a recurrence relation of the form $T_{k+1}(\hat{y}) = 2\hat{y}T_k(\hat{y}) - T_{k-1}(\hat{y})$ resulting in

$$(w_U)_{k+1}^{(m)} = 2 \sum_{n=-N_A}^{N_A} A_U^{(n)} (w_U)_k^{(m-n)} - (w_U)_{k-1}^{(m)} \quad \text{for } k > 1. \quad (3.33c)$$

Similarly,

$$(d_U)_0^{(m)} = 0 \text{ for } |m| \geq 0, (d_U)_1^{(0)} = 1, (d_U)_1^{(m)} = 0 \text{ for } |m| \geq 1, \quad (3.34a-c)$$

$$(d_U)_2^{(m)} = 4A_U^{(m)} \text{ for } |m| \geq 0,$$

and the use of the recurrence relation of the form $DT_{k+1}(\hat{y}) = 2T_k(\hat{y}) + 2\hat{y}DT_k(\hat{y}) - DT_{k-1}(\hat{y})$ gives

$$(d_U)_{k+1}^{(m)} = 2 \sum_{n=-N_A}^{N_A} A_U^{(n)} (d_U)_k^{(m-n)} - (d_U)_{k-1}^{(m)} + 2w_k^{(m)} \quad \text{for } k > 2. \quad (3.34d)$$

Substitution of the above relations into (3.31) gives

$$\frac{\partial \Psi_1}{\partial \hat{y}} = \sum_{n=-N_M}^{N_M} \sum_{k=0}^{N_T-1} \sum_{m=-N_S}^{N_S} G_k^{(n)} (d_U)_k^{(m)} e^{i(n+m)\alpha x} = \quad (3.35a)$$

$$\sum_{h=-N_S-N_M}^{N_S+N_M} \sum_{n=-N_M}^{N_M} \sum_{k=0}^{N_T-1} G_k^{(n)} (d_U)_k^{(h-n)} e^{ih\alpha x},$$

$$\frac{\partial \Psi_1}{\partial x} = i\alpha \sum_{n=-N_M}^{N_M} \sum_{k=0}^{N_T-1} \sum_{m=-N_S}^{N_S} n G_k^{(n)} (w_U)_k^{(m)} e^{i(n+m)\alpha x} = \quad (3.35b)$$

$$i\alpha \sum_{h=-N_S-N_M}^{N_S+N_M} \sum_{n=-N_M}^{N_M} \sum_{k=0}^{N_T-1} n G_k^{(n)} (w_U)_k^{(h-n)} e^{ih\alpha x}$$

where $h = n + m$. It can be deduced from (3.33) and (3.34) that $(w_U)_k^{(h-n)}$ and $(d_U)_k^{(h-n)}$ take the non-zero values only for $|h - n| \leq N_S$. Redefining the indices $n \rightarrow m$ and $h \rightarrow n$ in (3.35) and substituting them together with (3.27) into (3.16b,c) lead to boundary relations of the form

$$\sum_{m=-N_M}^{N_M} \sum_{k=0}^{N_T-1} G_k^{(m)} (d_U)_k^{(n-m)} = -\Gamma^{-1} F_U^{(n)} \quad 0 \leq |n| \leq N_f, \quad (3.36a)$$

$$\sum_{m=-N_M}^{N_M} \sum_{k=0}^{N_T-1} -im\alpha G_k^{(m)} (w_U)_k^{(n-m)} = -c\Gamma^{-1}(i\alpha) A_U^{(n)} \quad 1 \leq |n| \leq N_f \quad (3.36b)$$

where $N_f = (N_T - 1)N_A + N_M$. A similar process applied at the lower wall leads to the following relations

$$\sum_{m=-N_M}^{N_M} \sum_{k=0}^{N_T-1} G_k^{(m)} (d_L)_k^{(n-m)} = -\Gamma^{-1} F_L^{(n)} \quad 0 \leq |n| \leq N_f, \quad (3.37a)$$

$$\sum_{m=-N_M}^{N_M} \sum_{k=0}^{N_T-1} -im\alpha G_k^{(m)} (w_L)_k^{(n-m)} = -c\Gamma^{-1}(i\alpha) A_L^{(n)} \quad 1 \leq |n| \leq N_f. \quad (3.37b)$$

The reader may note that (3.36b) and (3.37b) do not provide conditions for $n = 0$ and this is due to the character of the boundary conditions for v_1 . The required conditions

can be constructed on the basis of boundary conditions (3.16c,e) written in terms of Ψ_T . These conditions are re-written in the following form

$$\Psi_{1,U}(x) = c\Gamma^{-1}[\hat{y}_U(x) - \hat{y}_L(x_0)] - 2c + \frac{4}{3} - \Psi_{0,U}(x), \quad (3.38a)$$

$$\Psi_{1,L}(x) = c\Gamma^{-1}[\hat{y}_L(x) - \hat{y}_L(x_0)] - \Psi_{0,L}(x). \quad (3.38b)$$

Values of Ψ_0 evaluated along the lower and upper walls represent known periodic functions of x which can be expressed as Fourier expansions of the form

$$\Psi_{0,U}(x) = \sum_{n=-3N_A}^{3N_A} \theta_U^{(n)} e^{inax}, \quad \Psi_{0,L}(x) = \sum_{n=-3N_A}^{3N_A} \theta_L^{(n)} e^{inax} \quad (3.39a,b)$$

where summations extend over the range $-3N_A \leq n \leq 3N_A$ due to the cubic nonlinearity of Ψ_0 . Coefficients $\theta_U^{(n)}$ and $\theta_L^{(n)}$ can be readily determined. Substituting (3.39) and (3.16g,h) into (3.38) and taking $x_0 = 0$ results in

$$\begin{aligned} \Psi_{1,U} = c\Gamma^{-1} \sum_{n=-N_M}^{N_M} A_U^{(n)} e^{inax} - c\Gamma^{-1} \sum_{n=-N_M}^{N_M} A_L^{(n)} - 2c + \frac{4}{3} - \\ \sum_{n=-N_M}^{N_M} \theta_U^{(n)} e^{inax}, \end{aligned} \quad (3.40a)$$

$$\Psi_{1,L} = c\Gamma^{-1} \sum_{n=-N_M}^{N_M} A_L^{(n)} e^{inax} - c\Gamma^{-1} \sum_{n=-N_M}^{N_M} A_L^{(n)} - \sum_{n=-N_M}^{N_M} \theta_L^{(n)} e^{inax}. \quad (3.40b)$$

Ψ_1 can be expressed at the walls using (3.17), (3.20) and (3.33) in the form

$$\Psi_{1,U} = \sum_{n=-N_f}^{N_f} \sum_{m=-N_M}^{N_M} \sum_{k=0}^{N_T-1} G_k^{(m)}(w_U)_k^{(n-m)} e^{inax}, \quad (3.41a)$$

$$\Psi_{1,L} = \sum_{n=-N_f}^{N_f} \sum_{m=-N_M}^{N_M} \sum_{k=0}^{N_T-1} G_k^{(m)}(w_L)_k^{(n-m)} e^{inax}. \quad (3.41b)$$

Substitution of (3.41) into (3.40) and extraction of the zeroth mode provide the two missing boundary relations of the form

$$\begin{aligned} \sum_{m=-N_M}^{N_M} \sum_{k=0}^{N_T-1} G_k^{(m)}(w_U)_k^{(m)*} = \\ -\theta_U^{(0)} + c\Gamma^{-1} A_U^{(0)} - c\Gamma^{-1} \sum_{n=-N_M}^{N_M} A_L^{(n)} - 2c + \frac{4}{3}, \end{aligned} \quad (3.42a)$$

$$\sum_{m=-N_M}^{N_M} \sum_{k=0}^{N_T-1} G_k^{(m)} (w_L)_k^{(m)*} = -\theta_L^{(0)} + c\Gamma^{-1} A_L^{(0)} - c\Gamma^{-1} \sum_{n=-N_M}^{N_M} A_L^{(n)}. \quad (3.42b)$$

The discretization of the field variables uses only N_M modes, where $N_M < N_f$ and, thus, only N_M relations of types (3.36), (3.37) can be enforced (relations (3.42) always have to be enforced). In the basic formulation, i.e. the so-called classical formulation [37], boundary relations corresponding to the lowest Fourier modes are used as the closing conditions; relations not used provide a measure of error in the enforcement of the flow boundary conditions as well as a test for the consistency of the method. Direct enforcement of a larger number of boundary relations leads to an over-determined formulation of the IBC method which is advantageous in the case of more extreme geometries [37]. This formulation will be discussed in Subsection 3.7.

3.4 Evaluation of the Pressure Field

The governing equations describing flow in the (x, \hat{y}) plane have the form

$$u_1 \partial_x u_1 + \Gamma v_1 \partial_{\hat{y}} u_1 + \Gamma v_1 D u_0 + (u_0 - c) \partial_x u_1 = -\partial_x p_1 + Re^{-1} (\partial_x^2 u_1 + \Gamma^2 \partial_{\hat{y}}^2 u_1), \quad (3.43a)$$

$$u_1 \partial_x v_1 + \Gamma v_1 \partial_{\hat{y}} v_1 + (u_0 - c) \partial_x v_1 = -\Gamma \partial_{\hat{y}} p_1 + Re^{-1} (\partial_x^2 v_1 + \Gamma^2 \partial_{\hat{y}}^2 v_1), \quad (3.43b)$$

$$\partial_x u_1 + \Gamma \partial_{\hat{y}} v_1 = 0. \quad (3.43c)$$

Introduction of velocity products defined as

$$\partial_x \widehat{u_1 u_1} = 2u_1 \partial_x u_1, \quad \partial_x \widehat{u_1 v_1} = u_1 \partial_x v_1 + v_1 \partial_x u_1, \quad \partial_{\hat{y}} \widehat{v_1 v_1} = 2v_1 \partial_{\hat{y}} v_1 \quad (3.44a-c)$$

leads to the field equations of the form

$$\partial_x \widehat{u_1 u_1} + \Gamma \partial_{\hat{y}} \widehat{u_1 v_1} + \Gamma v_1 D u_0 + (u_0 - c) \partial_x u_1 = -\partial_x p_1 + Re^{-1} (\partial_x^2 u_1 + \Gamma^2 \partial_{\hat{y}}^2 u_1), \quad (3.45a)$$

$$\partial_x \widehat{u_1 v_1} + \Gamma \partial_{\hat{y}} \widehat{v_1 v_1} + (u_0 - c) \partial_x v_1 = -\Gamma \partial_{\hat{y}} p_1 + Re^{-1} (\partial_x^2 v_1 + \Gamma^2 \partial_{\hat{y}}^2 v_1). \quad (3.45b)$$

Equation (3.45a) permits evaluation of the x -pressure gradient, i.e.

$$\begin{aligned} \partial_x p_1 = \\ -\partial_x \widehat{u_1 u_1} - \Gamma \partial_{\hat{y}} \widehat{u_1 v_1} - \Gamma v_1 D u_0 - (u_0 - c) \partial_x u_1 + Re^{-1} (\partial_x^2 u_1 + \Gamma^2 \partial_{\hat{y}}^2 u_1). \end{aligned} \quad (3.46)$$

The velocity components and the pressure modification can be represented as follows where A_p denotes the pressure gradient correction and $\sum_{n=-N_M}^{n=N_M} p_1^{(n)}(\hat{y}) e^{in\alpha x}$ describes the periodic part of the pressure modification:

$$\begin{aligned} u_1(x, \hat{y}) &= \Gamma \sum_{n=-N_M}^{N_M} D \Phi^{(n)}(\hat{y}) e^{in\alpha x}, \\ v_1(x, \hat{y}) &= -i\alpha \sum_{n=-N_M}^{N_M} n \Phi^{(n)}(\hat{y}) e^{in\alpha x}, \\ p_1(x, \hat{y}) &= A_p x + \sum_{n=-N_M}^{n=N_M} p_1^{(n)}(\hat{y}) e^{in\alpha x}. \end{aligned} \quad (3.47a-c)$$

Substitution of (3.47) and (3.18) into (3.46) and separation of Fourier modes result in

$$\begin{aligned} A_p + in\alpha p_1^{(n)}(\hat{y}) &= -in\alpha \widehat{u u}^{(n)}(\hat{y}) - \Gamma D \widehat{u v}^{(n)}(\hat{y}) + in\alpha \Gamma D u_0(\hat{y}) \Phi^{(n)}(\hat{y}) - \\ &\quad in\alpha \Gamma (u_0 - c)(\hat{y}) D \Phi^{(n)}(\hat{y}) + Re^{-1} [-n^2 \alpha^2 \Gamma D \Phi^{(n)}(\hat{y}) + \Gamma^3 D^3 \Phi^{(n)}(\hat{y})]. \end{aligned} \quad (3.48)$$

Equation (3.48) written for mode zero provides the expression for the evaluation of the pressure gradient correction, i.e.

$$A_p = Re^{-1} \Gamma^3 D^3 \Phi^{(0)}(\hat{y}) - \Gamma D \widehat{u v}^{(0)}(\hat{y}). \quad (3.49)$$

Equation (3.48) written for $n \neq 0$ gives the expression for the evaluation of $p_1^{(n)}(\hat{y})$, i.e.

$$\begin{aligned} p_1^{(n)}(\hat{y}) &= (in\alpha)^{-1} \{ -in\alpha \widehat{u u}^{(n)}(\hat{y}) - \Gamma D \widehat{u v}^{(n)}(\hat{y}) + in\alpha \Gamma D u_0(\hat{y}) \Phi^{(n)}(\hat{y}) - \\ &\quad in\alpha \Gamma (u_0 - c)(\hat{y}) D \Phi^{(n)}(\hat{y}) + Re^{-1} [-n^2 \alpha^2 \Gamma D \Phi^{(n)}(\hat{y}) + \Gamma^3 D^3 \Phi^{(n)}(\hat{y})] \}. \end{aligned} \quad (3.50)$$

Modal functions $p_1^{(n)}(\hat{y})$ can be expressed in terms of the Chebyshev polynomials as

$$p_1^{(n)}(\hat{y}) \approx \sum_{k=0}^{N_T-1} \Pi_k^{(n)} T_k(\hat{y}). \quad (3.51)$$

Insertion of (3.52), (3.20), and (3.21) into (3.50), taking the inner product with $T_j(\hat{y})$, and use of the orthogonality properties result in

$$\begin{aligned} \Pi_j^{(n)} = 2(in\alpha\pi C_j)^{-1} \sum_{k=0}^{N_T-1} \{ & -in\alpha G \widehat{u} \widehat{u}_k^{(n)} \langle T_j, T_k \rangle - \Gamma G \widehat{u} \widehat{v}_k^{(n)} \langle T_j, DT_k \rangle + \\ & in\alpha \Gamma G_k^{(n)} [\langle T_j, Du_0 T_k \rangle - \langle T_j, (u_0 - c) DT_k \rangle] + \\ & \Gamma Re^{-1} G_k^{(n)} [-n^2 \alpha^2 \langle T_j, DT_k \rangle + \Gamma^2 \langle T_j, D^3 T_k \rangle] \}, \text{ for } \begin{cases} n \neq 0, \\ 0 \leq j \leq N_T - 1, \end{cases} \end{aligned} \quad (3.52)$$

$$\text{where } C_j = \begin{cases} 2 & \text{for } j = 0, \\ 1 & \text{for } j \neq 0. \end{cases}$$

One needs to use the y -momentum equation to evaluate $p_1^{(0)}(\hat{y})$. Substitution of (3.47) and (3.18) into (3.45b) and separation of Fourier modes give

$$\begin{aligned} \Gamma D p_1^{(n)}(\hat{y}) = & -in\alpha \widehat{u} \widehat{v}^{(n)}(\hat{y}) - \Gamma D \widehat{v} \widehat{v}^{(n)}(\hat{y}) - n^2 \alpha^2 (u_0 - c)(\hat{y}) \Phi^{(n)}(\hat{y}) + \\ & Re^{-1} [in^3 \alpha^3 \Phi^{(n)}(\hat{y}) - in\alpha \Gamma^2 D^2 \Phi^{(n)}(\hat{y})]. \end{aligned} \quad (3.53)$$

Equation (3.53) written for mode zero takes the form

$$\Gamma D p_1^{(0)}(\hat{y}) = -\Gamma D \widehat{v} \widehat{v}^{(0)}(\hat{y}) \quad (3.54)$$

which, after integration, becomes

$$p_1^{(0)}(\hat{y}) = -\widehat{v} \widehat{v}^{(0)}(\hat{y}) + c_1 \quad (3.55)$$

where c_1 is the integration constant. Substitution of (3.51) and (3.21) into (3.55) and taking the inner product of the resultant relation with $T_j(\hat{y})$ provide the expression for the evaluation of $\Pi_j^{(0)}$, i.e.

$$\Pi_j^{(0)} = -2(C_j\pi)^{-1} \sum_{k=0}^{N_T-1} G\widehat{v}_k^{(0)} \langle T_j, T_k \rangle + 2c_1(C_j\pi)^{-1} \langle T_j, T_0 \rangle, \quad \text{for } 0 \leq j \leq N_T - 1. \quad (3.56)$$

The complete pressure field can be represented as

$$p_T(x, \hat{y}) = (-2Re^{-1} + A_p)x + \sum_{n=-N_M}^{N_M} \sum_{k=0}^{N_T-1} \Pi_k^{(n)} T_k(\hat{y}) e^{inax} + \text{const}, \quad (3.57)$$

where *const* stands for an arbitrary constant.

3.5 Solution Process

The solution process relies on iterations and yields new approximations of $\Phi^{(n)}(\hat{y})$, denoted as $[\Phi^{(n)}(\hat{y})]^{(k)}$, at each iteration where the superscript k denotes the iteration number. The nonlinear terms on the right hand side of (3.19) are taken from the previous iteration (these terms are ignored during the first iteration) resulting in the first order fixed point method. The iteration process can be summarized as

$$[\Phi^{(n)}]^{(k+1)} = [\Phi^{(n)}]^{(k)} + RF \left\{ [\Phi^{(n)}]^{(comp)} - [\Phi^{(n)}]^{(k)} \right\} \quad (3.58)$$

where the superscript *comp* identifies the solution computed at the new iteration, and the process is controlled using the under-relaxation parameter *RF*. Typically, $RF < 0.1$ is used with its value decreasing with an increase of the wave amplitude and the Reynolds number. Iterations are stopped when the convergence criterion of the form

$$\left| [\Phi^{(n)}]^{(k+1)} - [\Phi^{(n)}]^{(k)} \right| / \left| [\Phi^{(n)}]^{(k+1)} \right| < CONV \quad (3.59)$$

is satisfied, where $\left| [\Phi^{(n)}]^{(k+1)} - [\Phi^{(n)}]^{(k)} \right|$ is the L^2 norm of the difference between the solution vectors computed at two consecutive iterations and $\left| [\Phi^{(n)}]^{(k+1)} \right|$ is the L^2 norm of the current solution vector. $CONV = 10^{-14}$ was used in all tests of the algorithm while $CONV = 10^{-10}$ is sufficient for studies of effects of different physical parameters.

The nonlinear terms on the right hand side of (3.19) need to be updated at the end of each iteration step. It is more efficient to evaluate the required products by transferring data to the physical space, carrying out the multiplications there and transferring the results back into the Fourier space [66]. The new values of the velocity components of the form

$$\begin{aligned} u_1(x, \hat{y}) &= \Gamma \sum_{n=-N_M}^{N_M} D\Phi^{(n)}(\hat{y}) e^{inax}, \\ v_1(x, \hat{y}) &= -i\alpha \sum_{n=-N_M}^{N_M} n\Phi^{(n)}(\hat{y}) e^{inax} \end{aligned} \quad (3.60a,b)$$

are computed on a suitable grid in the (x, \hat{y}) plane. $2N_x + 2$ equidistant points, where $N_x = \frac{3}{2}N_M$, are used along the x -direction in order to remove the aliasing error with the last point removed due to periodicity, and N_T points are used in the \hat{y} -direction with the first and last points overlapping with the borders of the computational domain. Chebyshev points defined as $\hat{y}_j = \cos(\frac{j\pi}{N_T-1})$, where $j = 1, 2, \dots, N_T - 2$, are used in the interior of the domain. This process results in the formation of two matrices containing values of u_1 and v_1 and their multiplication yields the desired products, i.e. $\widehat{u_1 u_1}, \widehat{u_1 v_1}, \widehat{v_1 v_1}$. These products need to be expressed using Fourier expansions (3.18) which necessitates the determination of the modal functions $\widehat{uu}^{(n)}, \widehat{uv}^{(n)}, \widehat{vv}^{(n)}$. This is accomplished using the Fast Fourier Transform (FFT) at each \hat{y} -location; $2N_x + 1$ data points are used in the x -direction resulting in values of $2N_x + 1$ modal functions. Modal functions with indices in the range $[-N_M, N_M]$ are retained and the remaining ones are discarded as part of the aliasing error control process [66]. The last step involves expressing each modal function in terms of a Chebyshev expansion, i.e. the evaluation of coefficients $G\widehat{uu}_k^{(n)}, G\widehat{uv}_k^{(n)}, G\widehat{vv}_k^{(n)}$. Since values of these functions are available at the \hat{y} -grid points, one can write equation of type (3.21) for each point resulting in a system of linear equation whose numerical solution determines the unknown expansion coefficients. The number of grid points determines the maximum length of the Chebyshev expansion. No de-aliasing is required in the Chebyshev direction if a sufficient number of polynomials are used.

3.6 The Linear Solver

A linear algebraic problem for $G_k^{(n)}$ has to be solved at each iteration step. The problem has two types of intermodal coupling, i.e. coupling due to nonlinear terms and coupling due to boundary conditions. The former has been eliminated by the use of nonlinear terms from the previous iteration. The latter remains and, as result, one needs to solve a very large linear system involving all modal functions at each iteration step. A very efficient linear solver which takes advantage of the structure of the coefficient matrix following [38] is described below.

Governing equation (3.24) with the boundary conditions and closing constraint can be represented in matrix notation as

$$\mathbf{L}\mathbf{x} = \mathbf{R}(\mathbf{x}) \quad (3.61)$$

where \mathbf{L} denotes the coefficient matrix of size $p \times p$ with $p = (2N_M + 1)N_T$, \mathbf{x} is a p -dimensional vector of unknown Chebyshev coefficients $G_k^{(n)}$ and \mathbf{R} stands for the p -dimensional right-hand side vector which contains nonlinearities. This system is solved repeatedly during the iteration process.

Storage requirements can be reduced and the solution efficiency can be improved by taking advantage of the special structure of matrix \mathbf{L} . The structure of \mathbf{L} for $N_M = 5$ and $N_T = 31$ is shown in Figure 3.1 where all non-zero components have been marked in black and the unknowns have been organized according to the mode number $-N_M, \dots, 0, \dots, N_M$. The upper triangular blocks correspond to the modal equations and are uncoupled. The only coupling between blocks is provided thorough the boundary relations which are marked as black horizontal lines. In the first step \mathbf{L} is re-organized; the entries corresponding to the boundary relations are moved to the bottom of \mathbf{L} forming a block diagonal matrix \mathbf{L}_1 of size $q \times p$, where $q = (2N_M + 1)(N_T - 4)$ and a full matrix \mathbf{L}_2 of size $r \times p$, where $r = 4(2N_M + 1)$. In order to extract the largest possible square matrix \mathbf{A} (of size $q \times q$) from \mathbf{L}_1 , the unknown Chebyshev coefficients corresponding to the four lowest polynomials are placed at the end of the vector of unknowns. The resultant square matrix \mathbf{A} of size $q \times q$ has a block diagonal structure

with each block of size $(N_T - 4) \times (N_T - 4)$. The rectangular matrix \mathbf{B} of size $q \times r$ also has a block diagonal form with blocks of size $(N_T - 4) \times 4$ whereas the full rectangular matrix \mathbf{C} has size $r \times q$ and the full square matrix \mathbf{D} has size $r \times r$. Matrices \mathbf{B} and \mathbf{D} contain coefficients corresponding to $G_0^{(n)}, G_1^{(n)}, G_2^{(n)}$, and $G_3^{(n)}$, while information associated with the remaining coefficients is stored in matrices \mathbf{A} and \mathbf{C} .

Equation (3.24) can now be re-written in the form

$$\mathbf{A}\mathbf{x}_1 + \mathbf{B}\mathbf{x}_2 = \mathbf{R}_1, \quad \mathbf{C}\mathbf{x}_1 + \mathbf{D}\mathbf{x}_2 = \mathbf{R}_2 \quad (3.62a,b)$$

where vector \mathbf{x}_1 contains unknowns $G_k^{(n)}$ for $n \in \langle -N_M, N_M \rangle, k \in \langle 4, N_T - 1 \rangle$, and vector \mathbf{x}_2 contains unknowns $G_k^{(n)}$ for $n \in \langle -N_M, N_M \rangle, k \in \langle 0, 3 \rangle$. The solution of (3.62) can be written as

$$\mathbf{x}_2 = [\mathbf{D} - \mathbf{C}\mathbf{A}^{-1}\mathbf{B}]^{-1}(\mathbf{R}_2 - \mathbf{C}\mathbf{A}^{-1}\mathbf{R}_1), \quad \mathbf{x}_1 = \mathbf{A}^{-1}[\mathbf{R}_1 - \mathbf{B}\mathbf{x}_2]. \quad (3.63a,b)$$

The above procedure results in a substantial reduction in memory usage as one needs to store only the diagonal blocks of matrices \mathbf{A} and \mathbf{B} . The efficiency gains result from the construction of $\mathbf{A}^{-1}, \mathbf{C}\mathbf{A}^{-1}, \mathbf{C}\mathbf{A}^{-1}\mathbf{B}, \mathbf{A}^{-1}\mathbf{R}_1$ and $\mathbf{A}^{-1}\mathbf{B}$ block by block rather than working with complete matrices. The use of complex conjugate properties of the modal functions provides further efficiencies.

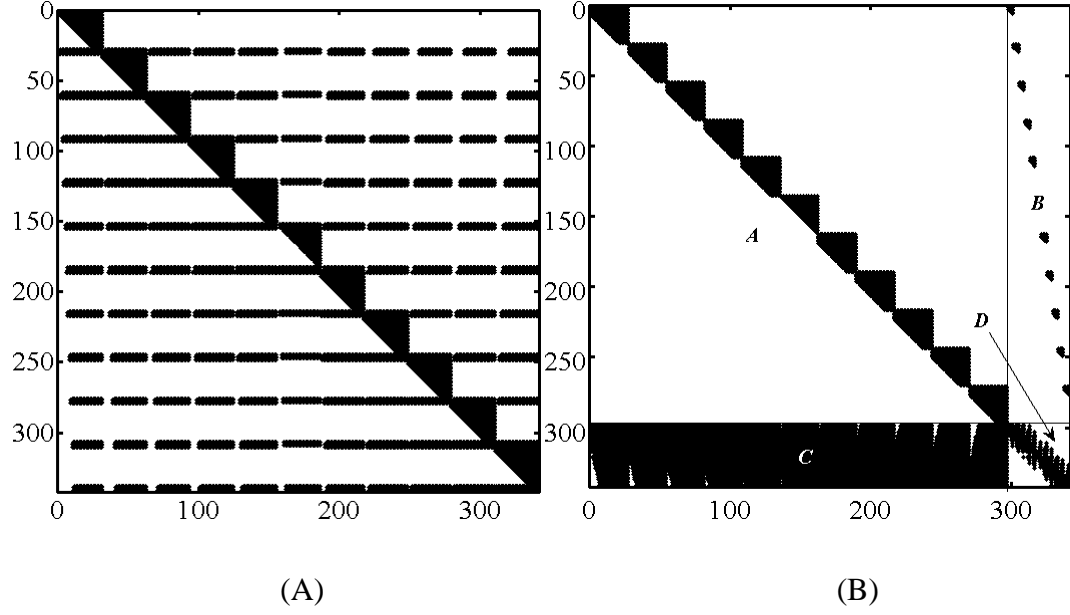


Figure 3.1: Structure of the coefficient matrix L for $N_M = 5$ and $N_T = 31$. Black identifies the non-zero elements. Figure 3.1A displays the coefficient matrix before the re-arrangement whereas Figure 3.1B displays its structure after the re-arrangement (see Subsection 3.6).

3.7 Performance of the Algorithm

This Subsection discusses results of various tests carried out in order to demonstrate the performance of the algorithm as well as to characterize the effects of numerical and physical parameters on the accuracy of the solution.

For simplicity, the majority of the reported tests deal with a sinusoidal wave propagating along the lower wall resulting in the channel geometry of the form

$$Y_U = 1, \quad Y_L = -1 + A \cos[\alpha(X - ct)] \quad (3.64a,b)$$

where A and α are the amplitude and the wave number of the wave, and c denotes its phase speed.

In a spectrally accurate algorithm, the solution converges exponentially as the number of Chebyshev polynomials N_T and the number of Fourier modes N_M increase. The solution error is defined as

$$Er = \max_{\text{solution domain}} |u(x, y) - u_{ref}(x, y)| \quad (3.65)$$

where the reference solution $u_{ref}(x, y)$ has been determined numerically using $N_T = 80$ Chebyshev polynomials and $N_M = 20$ Fourier modes. While the reference solution is not exact, the relevant numerical error is below machine level accuracy and, thus, the actual solution and the numerical test solution are the same within the double precision accuracy used in the tests. The Chebyshev expansions are guaranteed to be spectrally accurate [66] but, nevertheless, explicit tests to demonstrate that this accuracy is preserved in the IBC method have been carried out. Figure 3.2 displays variations of Er as a function of N_T while using $N_M = 20$ Fourier modes for the streamwise discretization and demonstrates the exponential decrease of Er with an increase of N_T . It has been verified that the number of Fourier modes used in this test reduces the x -discretization error below machine level accuracy and, thus, Er is a function of N_T only.

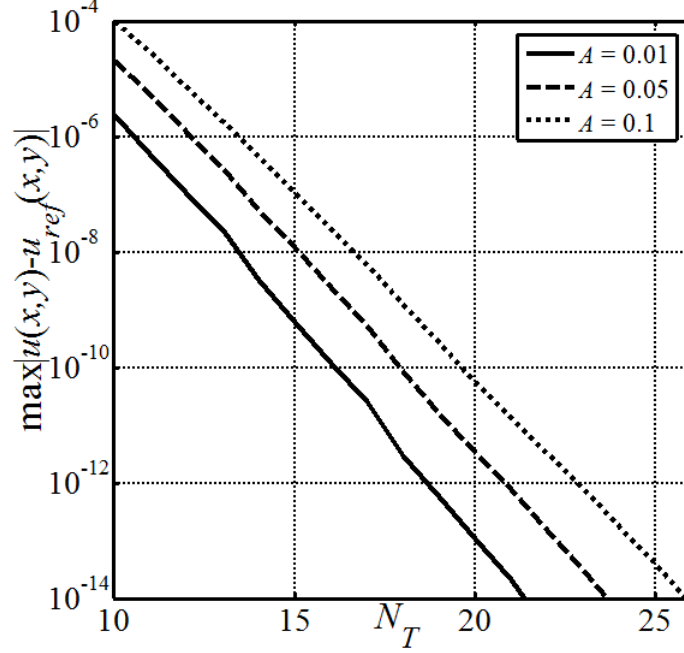


Figure 3.2: Variations of the error Er (see Eq. (3.65)) for the wave shape described by Eq. (3.64) with the wave number $\alpha = 1$, Reynolds number $Re = 5$, phase speed $c = 1.3$ and wave amplitudes A shown on the graph.

The above conclusions regarding the accuracy of Chebyshev expansions are subject to one constraint. The accuracy of the streamwise discretization depends on the convergence of the Fourier expansion (3.17) for the field variable and the Fourier expansions (3.36)–(3.37) for the boundary relations. If one of these expansions is slowly convergent, one may need to use more Fourier modes. Distributions of the real part of $D\Phi^{(n)}$ displayed in Figure 3.3 demonstrate that modal functions for higher modes are nearly zero everywhere except close to the vibrating wall where they form boundary layers. The need to resolve such layers may require the use of a greater number of Chebyshev polynomials than deemed necessary purely on the basis of spectral convergence. The convergence of the Fourier expansions (3.36)–(3.37) slows down for the short wavelength waves and, thus, the analysis of such waves requires the use of a greater number of Fourier modes. This, in turn, leads to the need for a greater number of Chebyshev polynomials. The elimination of spurious oscillations outside the boundary layers provides an easy method for verification if a sufficient number of Chebyshev polynomials have been used.

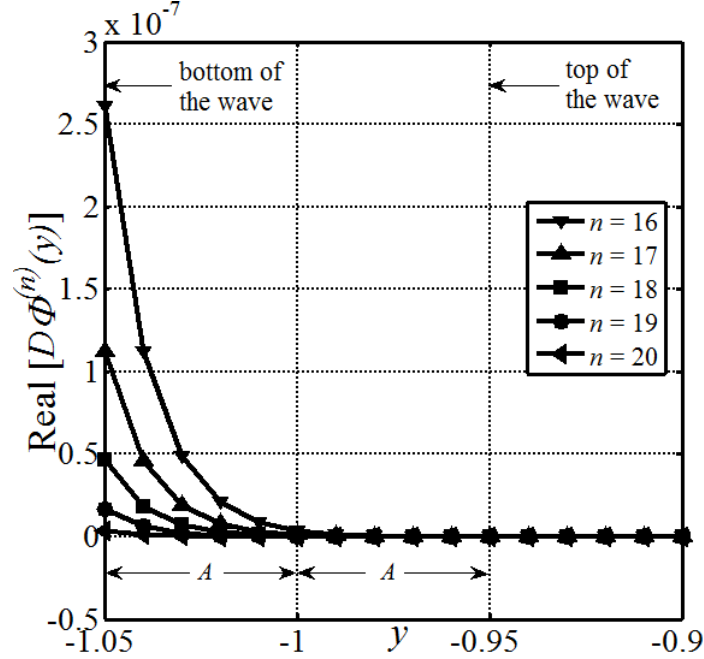


Figure 3.3: Distribution of the real part of $D\Phi^{(n)}$ as a function of y for higher Fourier modes ($n > 15$) in the region very close to the lower wall for the wave shape described by Eq. (3.64) with the wave number $\alpha = 5$, amplitude $A = 0.05$, Reynolds number $Re = 5$ and phase speed $c = 1.3$ obtained using $N_M = 20$ Fourier modes and $N_T = 80$ Chebyshev polynomials.

We shall now discuss the convergence of the Fourier expansions. Magnitudes of the modal functions $D\Phi^{(n)}$ can be measured using Chebyshev norms defined as

$$\|D\Phi^{(n)}\|_{\omega} = \left\{ \int_{-1}^1 D\Phi^{(n)}(\hat{y}) \cdot D\Phi^{(n)*}(\hat{y}) \cdot \omega(\hat{y}) \cdot d\hat{y} \right\}^{1/2}. \quad (3.66)$$

The results displayed in Figure 3.4 demonstrate the exponential decrease of the Chebyshev norm with the mode number n which confirms the spectral convergence of the x -discretization. Both $\Phi^{(n)}$ and $D\Phi^{(n)}$ are physically relevant as they represent velocity components; only $D\Phi^{(n)}$ has been used in the testing as the error in the determination of the function is smaller than in the determination of its derivative.

The overall accuracy of the IBC method is dominated by the accuracy in the enforcement of the boundary conditions [30, 35]. Conditions (2.4f,g) state that u_T and $v_T + ch'_L$ are to

be zero along the lower wall and, thus, their values, denoted as u_L and $v_L + ch'_L$, provide a means for assessing the error of the whole method. It is convenient to use the L^∞ norm of u_T and $v_T + ch'_L$, i.e.

$$\|u_L\|_\infty = \sup|u_L(x, y_L(x))|, \quad \|v_L + ch'_L\|_\infty = \sup|v_L(x, y_L(x)) + ch'_L(x)|, \quad (3.67a,b)$$

where $0 \leq x \leq 2\pi/\alpha$, as an explicit measure of the error. Figure 3.5 displays variations of both norms as a function of the number of Fourier modes N_M used in the computations. These norms decrease exponentially with an increase of N_M and this demonstrates the spectral convergence of the algorithm.

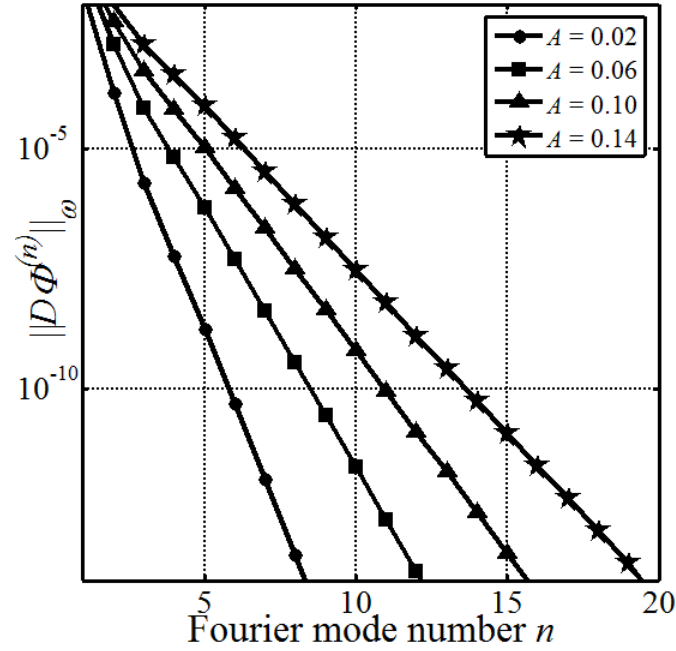


Figure 3.4: Variations of the Chebyshev norm of $D\Phi^{(n)}$ as a function of the Fourier mode number determined for the wave shape described by Eq. (3.64) with the wave number $\alpha = 1$ and with different wave amplitudes A . Calculations were carried out for Reynolds number $Re = 5$ and wave phase speed $c = 1.3$ using $N_M = 20$ Fourier modes and $N_T = 80$ Chebyshev polynomials.

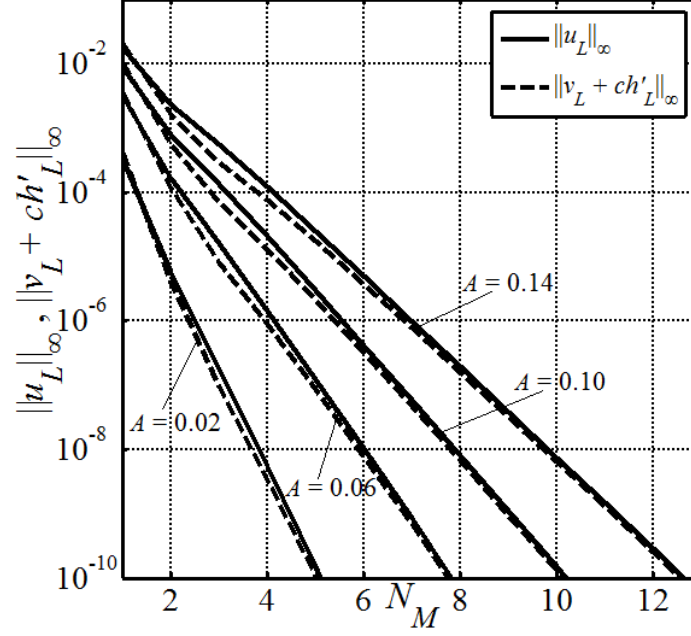


Figure 3.5: Variations of the $\|u_L\|_\infty$, $\|v_L + ch'_L\|_\infty$ norms as functions of the total number of Fourier modes N_M used in the calculation for the wave shape described by Eq. (3.64) with the wave number $\alpha = 1$ and with different amplitudes A . Calculations have been carried out for Reynolds number $Re = 5$ and phase speed $c = 1.3$ using $N_T = 80$ Chebyshev polynomials.

Distributions of errors along the vibrating wall provide useful information about the properties of the method. This error is dominated by the Fourier expansion truncation, i.e. it is dominated by the higher modal functions. Locations of the error maxima coincide with the location of the maximum channel opening as documented by the distributions of u_L and $v_L + ch'_L$ over one wavelength displayed in Figure 3.6. Data presented in Figure 3.3 demonstrate that the maxima of the modal functions $D\Phi^{<n>}$ occur around the edge of the solution domain; distributions of $\Phi^{<n>}$, which are not shown, have the same form. This means that the flow field around the crest of the wave is less affected by higher Fourier modes when compared to the flow field in the valley position. As a result, the truncation of the Fourier expansion has a greater effect in the valley position than in the crest position. This effect is more pronounced for waves with shorter wavelengths as the boundary layers in the distributions of the modal functions are thinner.

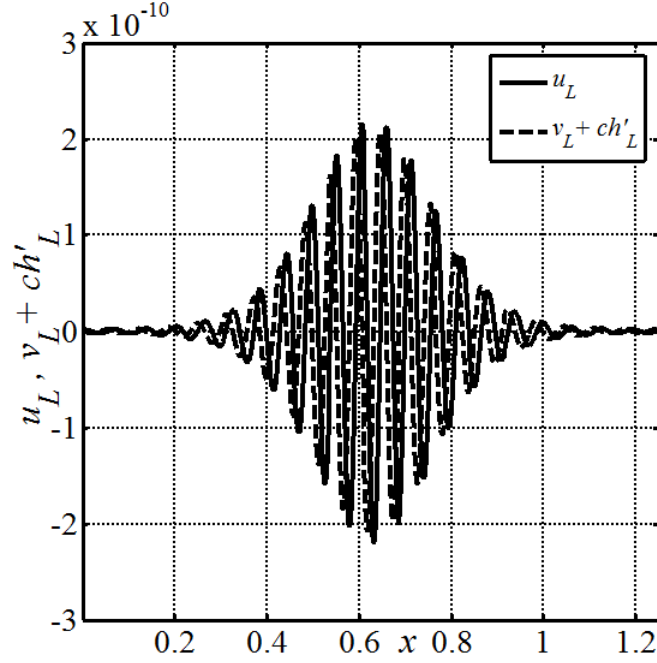


Figure 3.6: Distributions of the error in the enforcement of the boundary conditions along the vibrating wall, i.e. u_L and $v_L + ch'_L$, for the wave with shape described by Eq. (3.64) with the wave number $\alpha = 5$ and amplitude $A = 0.05$. Calculations were carried out for Reynolds number $Re = 5$ and phase speed $c = 1.3$ using $N_M = 20$ Fourier modes and $N_T = 80$ Chebyshev polynomials.

The Fourier spectra of the boundary error are defined as

$$u_L(x) = \sum_{n=-\infty}^{\infty} U_L^{(n)} e^{inax}, \quad v_L(x) + ch'_L(x) = \sum_{n=-\infty}^{\infty} V_L^{(n)} e^{inax} \quad (3.68a,b)$$

and their distributions are shown in Figure 3.7. These spectra should not contain any harmonics of order lower than or equal to the number of Fourier modes used in the enforcement of the boundary conditions (2.4f,g). The results displayed in Figure 3.7 demonstrate the absence of the first 20 Fourier modes in the computations carried out using $N_M = 20$ Fourier modes consistent with the construction of the boundary relations.

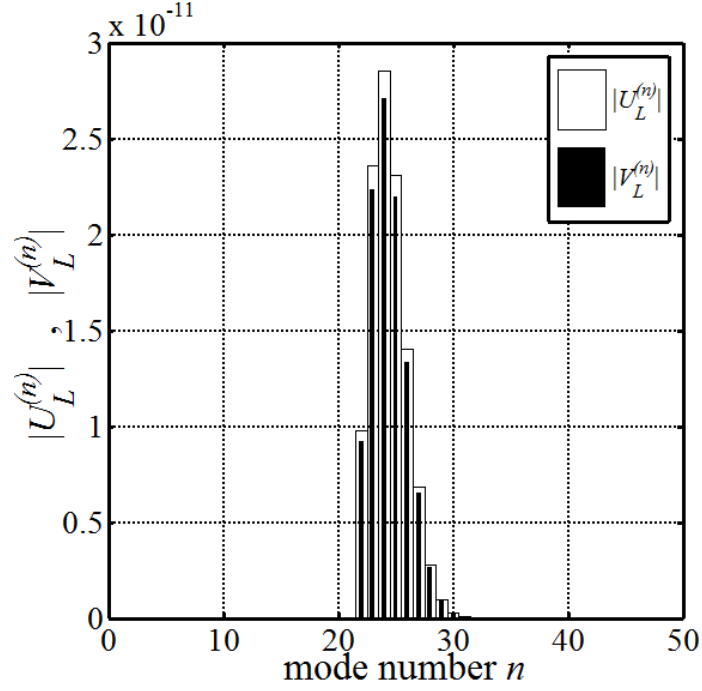


Figure 3.7: Fourier spectra of the error in the enforcement of the boundary conditions along the vibrating wall, i.e. Eq. (3.68), for the wave with shape described by Eq. (3.64) with wave number $\alpha = 5$ and amplitude $A = 0.05$. Calculations were carried out for the Reynolds number $Re = 5$ and phase speed $c = 1.3$ using $N_M = 20$ Fourier modes and $N_T = 80$ Chebyshev polynomials. The reader should note the absence of the first 20 Fourier modes.

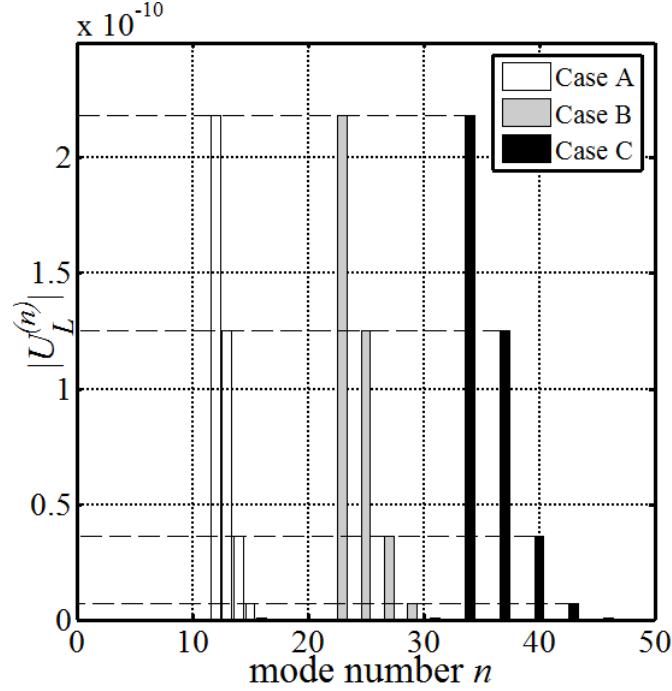


Figure 3.8: Fourier spectra of $u_L(x)$ for the wave shape described by Eq. (3.64) with the amplitude $A = 0.04$ and wavelength $\lambda_x = 2\pi/3$. Solutions have been obtained in case A using $N_M = 10$ Fourier modes, in case B using $N_M = 20$ Fourier modes, and in case C using $N_M = 30$ Fourier modes. Calculations were carried out with Reynolds number $Re = 5$ and phase speed $c = 1.3$ using $N_T = 80$ Chebyshev polynomials.

In order to show that the algorithm does not produce spurious subharmonics, a wave with wavelength $\lambda_x = 2\pi/3$ has been analyzed using three different numerical setups. In case A, the shape of the wave has been represented by the principal Fourier mode with the wave number $\alpha = 3$ and the solution has been obtained using $N_M = 10$ Fourier modes. In case B, the same shape has been represented by the second Fourier mode of an expansion with the principal mode corresponding to the wave number $\alpha = 1.5$ and the solution has been obtained using $N_M = 20$ Fourier modes in order to provide space for all modes used in case A. Finally, in case C, the shape was represented by the third Fourier mode of an expansion with the principal mode corresponding to the wave number $\alpha = 1$ and the solution has been obtained using $N_M = 30$ Fourier modes. Cases B and C admitted subharmonics of $1/2$ and $1/3$ types, respectively, but the results displayed in Figure 3.8 show that the algorithm has not produced any spurious subharmonics.

Variations of the error in the enforcement of the boundary conditions as a function of the wave parameters, i.e. the amplitude A and the wave number α , are shown in Figures 3.9 and 3.10. Only variations of $\|u_L\|_\infty$ are shown as this represents a more demanding test. The error remains at machine level as long as A and α assume values below certain critical thresholds. When either A or α increases beyond this threshold, the error starts to increase rapidly. These thresholds can be increased by increasing the number of Fourier modes and the number of Chebyshev polynomials used in the computations. One may need to use an excessively large N_M and N_T in order to significantly increase the threshold and this places limitations on the applicability of the proposed method when dealing with waves of large amplitudes and short wavelengths. An over-determined formulation discussed in Subsection 3.8 provides a more efficient alternative.

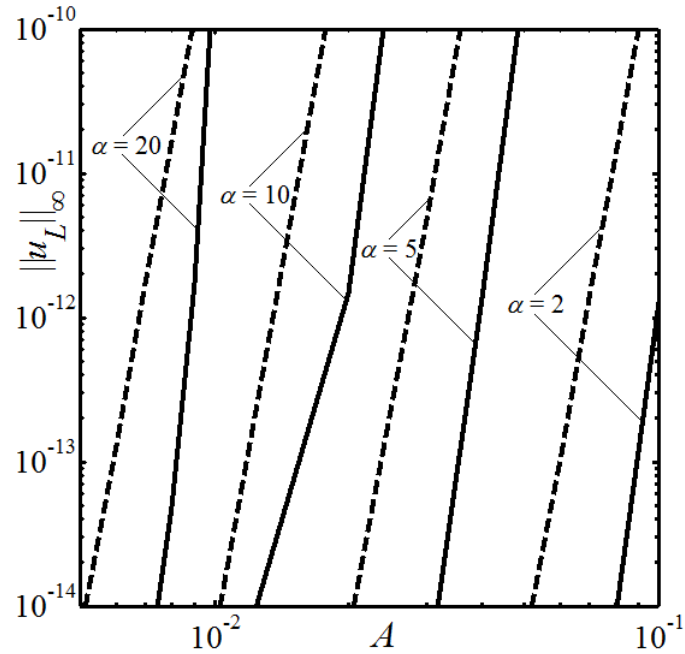


Figure 3.9: Variations of the $\|u_L\|_\infty$ norm for the wave shape described by Eq. (3.64) as a function of the wave amplitude A for selected wave numbers α . Dashed and solid lines correspond to results obtained with $N_M = 15$ and $N_M = 20$ Fourier modes, respectively. Calculations have been carried out for the Reynolds number $Re = 5$ and phase speed $c = 1.3$ using $N_T = 80$ Chebyshev polynomials.

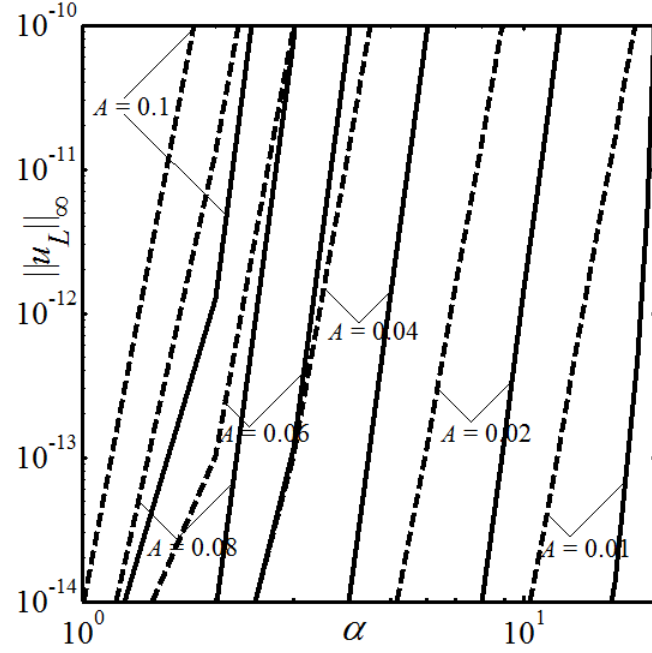


Figure 3.10: Variations of the $\|u_L\|_\infty$ norm for the wave shape described by Eq. (3.64) as a function of the wave number α for selected amplitudes A . Dashed and solid lines correspond to results obtained with $N_M = 15$ and $N_M = 20$ Fourier modes, respectively. Calculations have been carried out with Reynolds number $Re = 5$ and phase speed $c = 1.3$ using $N_T = 80$ Chebyshev polynomials.

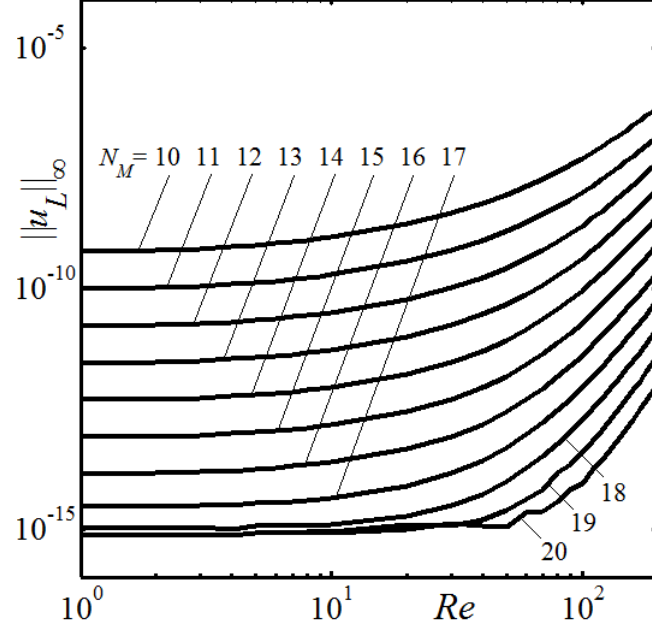


Figure 3.11: Variations of the $\|u_L\|_\infty$ norm for the wave shape described by Eq. (3.64) with the wave number $\alpha = 2$, the amplitude $A = 0.06$ and the phase speed $c = 1.3$ as a function of Reynolds number computed using different numbers of Fourier modes N_M and $N_T = 80$ Chebyshev polynomials.

Figure 3.11 illustrates variations of $\|u_L\|_\infty$ as a function of the Reynolds number Re . The error change is marginal as long as Re remains smaller than a certain threshold. As Re increases above this threshold, the error rises rapidly but its magnitude can be controlled through an increase in the number of Fourier modes. Variations of the error as a function of the phase speed c shown in Figure 3.12 demonstrate a similar behavior. The minimum error occurs for the wave propagating with a phase speed similar to the flow velocity. When the wave phase speed increases above the maximum flow velocity or the wave propagates in the negative x -direction, the error increases with an increase in the magnitude of c . This error can be easily controlled by increasing the number of Fourier modes N_M .

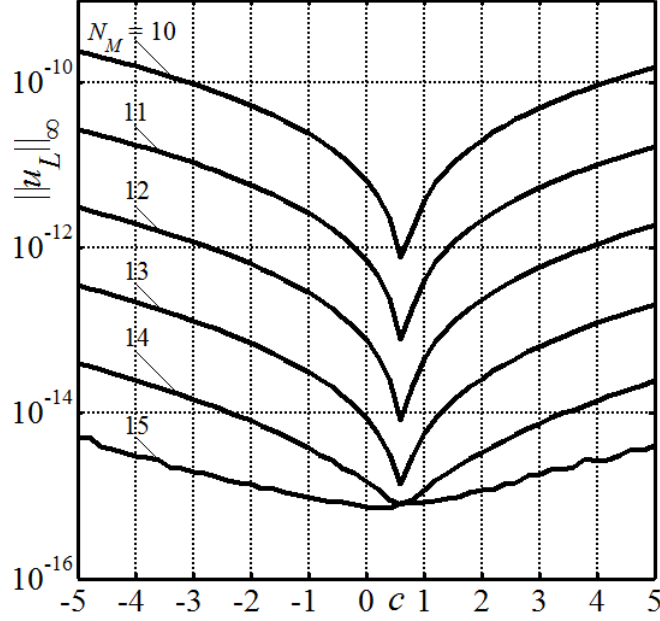


Figure 3.12: Variations of the $\|u_L\|_\infty$ norm for the wave shape described by Eq. (3.64) with amplitude $A = 0.04$, wave number $\alpha = 2$ and Reynolds number $Re = 5$ as a function of the phase speed c determined using different numbers of Fourier modes N_M and $N_T = 80$ Chebyshev polynomials.

3.8 The Over-Determined Formulation

Results displayed in Figures 3.9–3.10 demonstrate a rapid increase of the error when the wave amplitude increases above a certain critical threshold, with the value of this threshold depending on the wave amplitude. As the algorithm involves the use of two Fourier expansions, one for the field variables and one for the boundary conditions, it can be concluded that the convergence rate of the expansion representing the boundary conditions slows down as the geometry becomes more extreme. This suggests that the use of more Fourier modes in the expansion for the boundary conditions could increase the accuracy but adopting this method leads to an over-determined formulation [37].

The over-determined system is created using $4(2M_M + 1)$ boundary constraints of type (3.36), (3.37), and (3.42), where $|n| = 0, \dots, M_M$ and $N_f \geq M_M \geq N_M$ with M_M being the number of Fourier modes used for the representation of the field variables (Eq. (3.17)).

The system reduces to the same form as in Subsection 3.3 if $M_M = N_M$. The over-determined linear system has the form

$$\mathbf{L}_0 \mathbf{x} = \mathbf{z}_0, \quad (3.69)$$

where \mathbf{L}_0 is a $r \times p$ coefficient matrix with $p = (2N_M + 1)N_T$ and $r = p + 8(M_M - N_M)$ and \mathbf{x} is a known p -dimensional column vector and \mathbf{z}_0 is a r -dimensional right-hand side vector. The structure of \mathbf{L}_0 for $N_M = 5$, $M_M = 10$, and $N_T = 31$ is shown in Figure 3.13A where all non-zero components have been marked using black. The matrix is organized by placing entries corresponding to the field equations in matrix \mathbf{H} of size $q \times p$, $q = (2N_M + 1)(N_T - 4)$, and entries corresponding to the boundary constraints in matrix \mathbf{K}_0 of size $(r - q) \times p$. \mathbf{H} has a block-diagonal structure with each block having the size $(N_T - 4) \times N_T$; \mathbf{K}_0 is full as it provides the coupling between different Fourier modes.

System (3.69) can be solved only in the least squares sense. The solution can be written in the form of

$$\mathbf{x} = \mathbf{L}_0^+ \mathbf{z}_0 \quad (3.70)$$

where \mathbf{L}_0^+ represents the generalized inverse (or pseudo-inverse) of \mathbf{L}_0 . In the present work, the QR factorization, as well as the singular value decomposition (SVD), are used to evaluate \mathbf{L}_0^+ .

In the QR factorization method, the matrix $\mathbf{L}_0 \in \mathbb{C}^{r \times p}$ is split into a product of a unitary matrix $\mathbf{Q} \in \mathbb{C}^{r \times r}$ and another matrix $\mathbf{R} \in \mathbb{C}^{r \times p}$ in such a way that

$$\mathbf{L}_0 = \mathbf{Q}\mathbf{R} = \mathbf{Q} \begin{pmatrix} \mathbf{R}_1 \\ \mathbf{0} \end{pmatrix} \quad (3.71a)$$

where $\mathbf{R}_1 \in \mathbb{C}^{p \times p}$ is an upper-triangular matrix. \mathbf{L}_0^+ can be represented as

$$\mathbf{L}_0^+ = (\mathbf{R}_1^{-1} \quad \mathbf{0}) \mathbf{Q}^H \quad (3.71b)$$

where $\mathbf{L}_0^+ \in \mathbb{C}^{p \times r}$ and the superscript H denotes the conjugate transpose.

According to the SVD method, for any matrix $\mathbf{L}_0 \in \mathbb{C}^{r \times p}$ of rank h there exist unitary matrices $\mathbf{U} \in \mathbb{C}^{r \times r}$ and $\mathbf{V} \in \mathbb{C}^{p \times p}$ such that

$$\mathbf{L}_0 = \mathbf{U} \mathbf{S} \mathbf{V}^H, \quad \mathbf{S} = \begin{pmatrix} \mathbf{S}_1 & \mathbf{0} \\ \mathbf{0} & \mathbf{0} \end{pmatrix} \quad (3.72a)$$

where $\mathbf{S} \in \mathbb{C}^{r \times p}$, $\mathbf{S}_1 = \text{diag}(\sigma_1, \sigma_2, \sigma_3, \dots, \sigma_h)$ and

$$\sigma_1 \geq \sigma_2 \geq \sigma_3 \geq \dots \geq \sigma_h > 0 \quad (3.72b)$$

are the singular values of \mathbf{L}_0 . The pseudo-inverse can be expressed in the form of

$$\mathbf{L}_0^+ = \mathbf{V} \begin{pmatrix} \mathbf{S}_1^{-1} & \mathbf{0} \\ \mathbf{0} & \mathbf{0} \end{pmatrix} \mathbf{U}^H. \quad (3.72c)$$

The construction of the efficient solver begins with the re-arrangement of matrix \mathbf{L}_0 [39]. The largest square matrix \mathbf{A} of the size $q \times q$ is extracted from \mathbf{H} in a manner similar to that described in Subsection 3.6 resulting in the matrix structure illustrated in Figure 3.13B. The \mathbf{A} and \mathbf{B} matrices have block-diagonal structures, while the rectangular matrices \mathbf{C}_0 and \mathbf{D}_0 are of sizes $(r - q) \times q$ and $(r - q) \times (p - q)$, respectively (see Figure 3.13B). The system (3.69) can now be written in the following form

$$\mathbf{A} \mathbf{x}_1 + \mathbf{B} \mathbf{x}_2 = (\mathbf{z}_0)_1, \quad \mathbf{C}_0 \mathbf{x}_1 + \mathbf{D}_0 \mathbf{x}_2 = (\mathbf{z}_0)_2 \quad (3.73a,b)$$

where vectors \mathbf{x}_1 and \mathbf{x}_2 contain unknowns $G_k^{(n)}$, $n \in \langle -N_M, N_M \rangle$, for $k \in \langle 4, N_T - 1 \rangle$ and $k \in \langle 0, 3 \rangle$, respectively. The right hand side vector is presented as $[(\mathbf{z}_0)_1 \quad (\mathbf{z}_0)_2]^T = \mathbf{z}_0$ where vectors $(\mathbf{z}_0)_1$ and $(\mathbf{z}_0)_2$ have sizes q and $r - q$, respectively. The solution of (3.73) has the form

$$\mathbf{x}_2 = (\mathbf{D}_0 - \mathbf{C}_0 \mathbf{A}^{-1} \mathbf{B})^+ [(\mathbf{z}_0)_2 - \mathbf{C}_0 \mathbf{A}^{-1} (\mathbf{z}_0)_1], \quad \mathbf{x}_1 = \mathbf{A}^{-1} [(\mathbf{z}_0)_1 - \mathbf{B} \mathbf{x}_2] \quad (3.74a,b)$$

where $\mathbf{A}^{-1}(\mathbf{z}_0)_1$ and $\mathbf{A}^{-1} \mathbf{B}$ can be computed block by block in order to reduce the computational time and memory requirements. One should note that the part of the system corresponding to the field equations is solved exactly while the part corresponding to the boundary constraints is solved in the least squares sense.

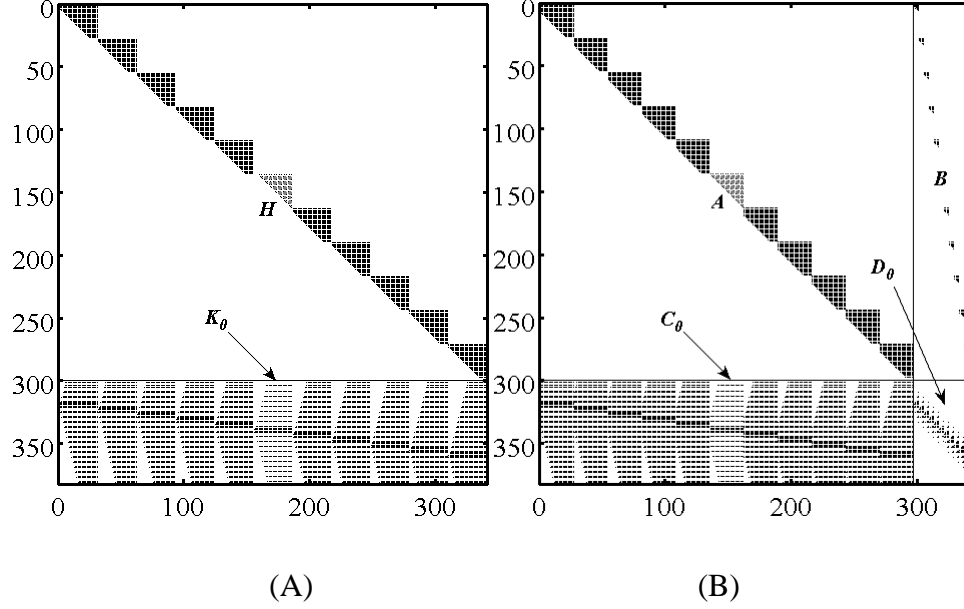


Figure 3.13: Structure of the coefficient matrix L_0 for $N_M = 5$, $M_M = 10$ and $N_T = 31$ resulting from the use of the over-determined IBC method. Black identifies the non-zero elements. Figure 3.13A displays the coefficient matrix before the re-arrangement whereas Figure 3.13B displays its structure after the re-arrangement (see Subsection 3.8).

Figure 3.14 displays Fourier spectra of the boundary error along the vibrating wall (see Eq. (3.68)) for the same conditions as in Figure 3.7. It can be seen that the error is distributed over several modes including modes with $n < N_M$ which is expected from the least squares solution. Figure 3.15 illustrates variations of the error as a function of the wave amplitude A obtained using SVD and QR methods. If one considers the maximum acceptable error to be at the level of 10^{-6} , the over-determined formulation expands the range of applicability of the IBC method by approximately 40% when measured in terms of the wave amplitude A . There is no advantage to using either SVD or QR techniques. The same results demonstrate that there is an optimal value of M_M which provides the best accuracy at a minimal cost as an increase in the number of boundary relations used in the computations beyond this value does not improve the accuracy of the results (see Figure 3.15); the optimal M_M is approximately equal to $1.5N_M$. Figure 3.16 illustrates error variations as a function of the wave amplitude resulting from the use of different numbers of Fourier modes N_M combined with the optimal number of boundary relations.

These results demonstrate a significant expansion in the applicability of the IBC method provided by the over-determined formulation.

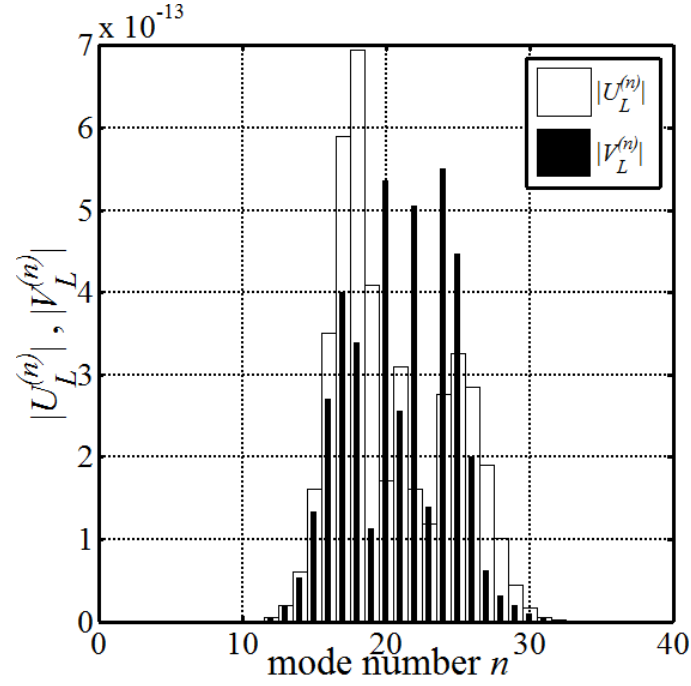


Figure 3.14: Fourier spectra of the error in the enforcement of the boundary conditions along the vibrating wall (see Eq. (3.68)) for the wave with shape described by Eq. (3.64) with wave number $\alpha = 5$ and amplitude $A = 0.05$. Calculations have been carried out for $Re = 5$ and $c = 1.3$ using $N_M = 20$ Fourier modes, $M_M = 30$ boundary relations and $N_T = 80$ Chebyshev polynomials.

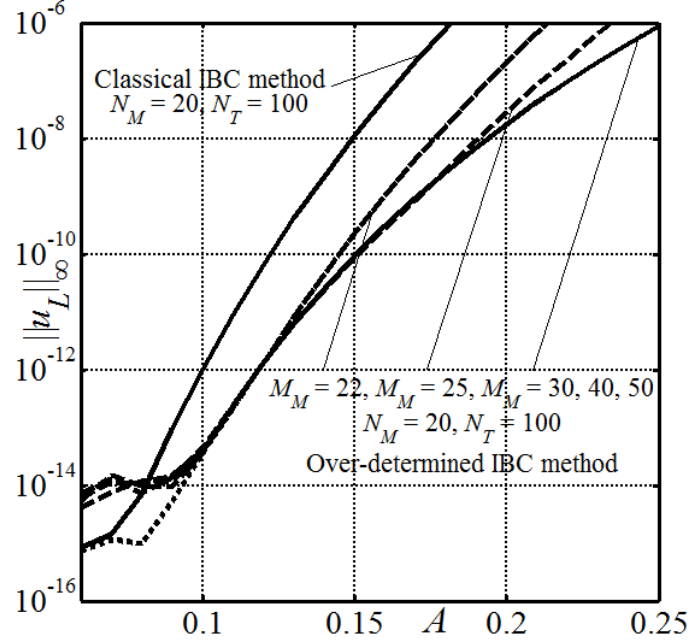


Figure 3.15: Variations of the $\|u_L\|_\infty$ norm as a function of the wave amplitude A for the wave shape described by Eq. (3.64) with wave number $\alpha = 2$ and phase speed $c = 1.3$ for $Re = 1$ resulting from the use of the over-determined method. Dashed and dotted lines correspond to results obtained using the SVD and QR factorization techniques, respectively. Calculations have been carried out using $N_M = 20$ Fourier modes and $N_T = 100$ Chebyshev polynomials.

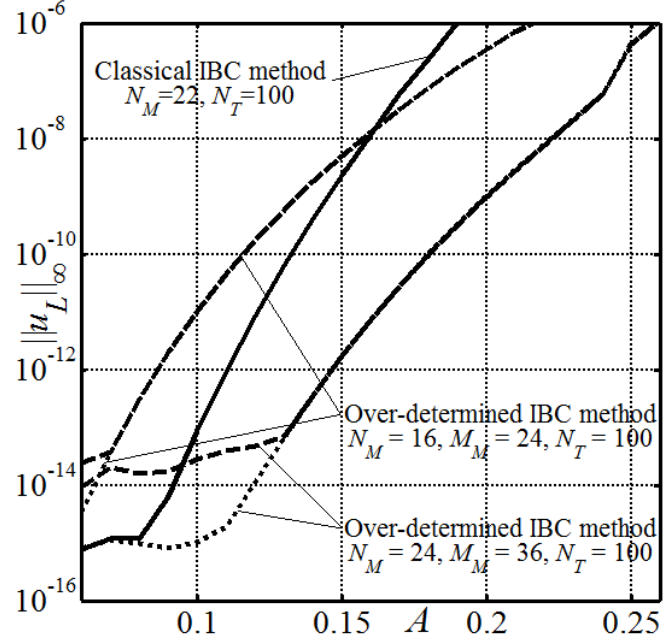
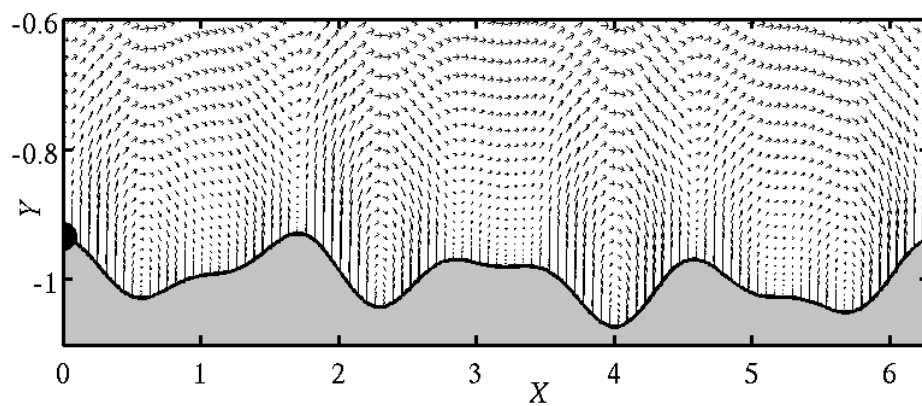


Figure 3.16: Variations of the $\|u_L\|_\infty$ norm as a function of the wave amplitude A for the wave shape described by Eq. (3.64) with phase speed $c = 1.3$ and wave number $\alpha = 2$ for $Re = 1$ determined using the over-determined formulation. Dashed and dotted lines correspond to results obtained using SVD and QR factorization techniques, respectively. Calculations have been carried out using $N_T = 100$ Chebyshev polynomials and different numbers N_M of Fourier modes and an optimal number M_M of boundary relations.

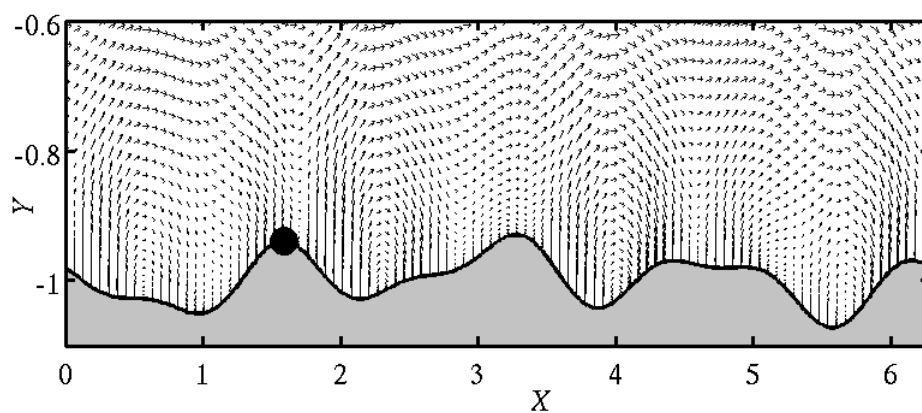
Figure 3.17 illustrates the velocity field in a channel where the lower wall vibrates resulting in the channel geometry of the form

$$\begin{aligned}
 Y_U &= 1, \\
 Y_L &= -1 + A \sin[\alpha(X - ct)] + 2A \cos[4\alpha(X - ct)] + A \cos[7\alpha(X - ct)].
 \end{aligned}
 \tag{3.75}$$

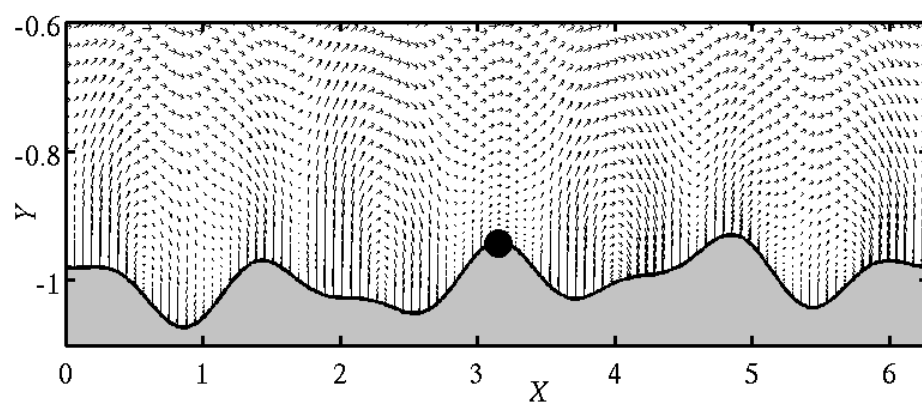
The velocity vector plot demonstrates the algorithm's abilities to deal with complex vibrations.



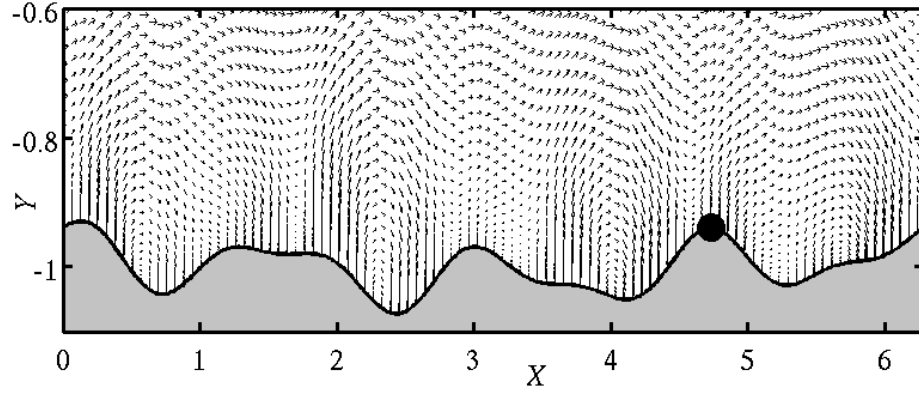
(A)



(B)



(C)



(D)

Figure 3.17: Plots of the velocity field in a vibrating channel whose geometry is described by Eq. (3.75) with $\alpha = 1$, $A = 0.02$, $Re = 5$ and $c = 1.3$. The black dot represents a reference point moving with the phase speed. Figures 3.17 A–D correspond to times $t = t_0$, $t = t_0 + T/4$, $t = t_0 + T/2$, $t = t_0 + 3T/4$, respectively, where $T = 2\pi/\alpha c$ stands for a period of vibration and t_0 denotes the time when the black dot was located at $X = 0$. $N_T = 120$ Chebyshev polynomials and $N_M = 60$ Fourier modes have been used in the calculations.

Section 4

4 Pressure Losses in Vibrating Channels

Subsection 4.1 describes the determination of forces. Subsection 4.2 discusses the mechanics of drag generation in vibrating channels and provides solution for the long wavelength waves. Subsection 4.3 provides a solution for the small amplitude waves. Subsection 4.4 is devoted to parametrization of features of wave geometry that is relevant to pressure losses.

4.1 Determination of Forces

We shall use the solution method described in details in Section 3. Analysis of drag requires determination of forces acting on the fluid at the walls. It begins with the specification of the outwards normal unit vectors of the form

$$\begin{aligned}\mathbf{n}_U &= (n_{U,x}, n_{U,y}) = (-h'_U, 1) \left[1 + (h'_U)^2 \right]^{-\frac{1}{2}}, \\ \mathbf{n}_L &= (n_{L,x}, n_{L,y}) = (h'_L, -1) \left[1 + (h'_L)^2 \right]^{-\frac{1}{2}}.\end{aligned}\tag{4.1}$$

The stress tensor is of the form

$$\vec{\sigma} = \begin{bmatrix} \sigma_{xx} & \sigma_{xy} \\ \sigma_{yx} & \sigma_{yy} \end{bmatrix} = \begin{bmatrix} -p_0 - p_1 + 2Re^{-1} \frac{\partial u_1}{\partial x} & Re^{-1} \left(\frac{du_0}{dy} + \frac{\partial u_1}{\partial y} + \frac{\partial v_1}{\partial x} \right) \\ Re^{-1} \left(\frac{du_0}{dy} + \frac{\partial u_1}{\partial y} + \frac{\partial v_1}{\partial x} \right) & -p_0 - p_1 + 2Re^{-1} \frac{\partial v_1}{\partial y} \end{bmatrix},\tag{4.2}$$

the stresses $\mathbf{f} = (f_x, f_y)$ and $\mathbf{g} = (g_x, g_y)$ acting on the lower and upper walls, respectively, are evaluated as

$$\mathbf{f} = \mathbf{n}_L \cdot \vec{\sigma}|_{y_L(x)} \quad , \quad \mathbf{g} = \mathbf{n}_U \cdot \vec{\sigma}|_{y_U(x)}\tag{4.3}$$

with their components are written as

$$Re f_x = Re(f_{x,visc} + f_{x,pres}) =$$

$$\left[2n_{L,x} \frac{\partial u_1}{\partial x} \Big|_{y_L(x)} + n_{L,y} \left(\frac{du_0}{dy} + \frac{\partial u_1}{\partial y} + \frac{\partial v_1}{\partial x} \right) \Big|_{y_L(x)} \right] - Re[n_{L,x}(p_0 + p_1)|_{y_L(x)}], \quad (4.4a)$$

$$Re f_y = Re(f_{y,visc} + f_{y,pres}) =$$

$$\left[n_{L,x} \left(\frac{du_0}{dy} + \frac{\partial u_1}{\partial y} + \frac{\partial v_1}{\partial x} \right) \Big|_{y_L(x)} + 2n_{L,y} \frac{\partial v_1}{\partial y} \Big|_{y_L(x)} \right] - Re[n_{L,y}(p_0 + p_1)|_{y_L(x)}], \quad (4.4b)$$

$$Re g_x = Re(g_{x,visc} + g_{x,pres}) =$$

$$\left[2n_{U,x} \frac{\partial u_1}{\partial x} \Big|_{y_U(x)} + n_{U,y} \left(\frac{du_0}{dy} + \frac{\partial u_1}{\partial y} + \frac{\partial v_1}{\partial x} \right) \Big|_{y_U(x)} \right] -$$

$$Re[n_{U,x}(p_0 + p_1)|_{y_U(x)}], \quad (4.4c)$$

$$Re g_y = Re(g_{y,visc} + g_{y,pres}) =$$

$$\left[n_{U,x} \left(\frac{du_0}{dy} + \frac{\partial u_1}{\partial y} + \frac{\partial v_1}{\partial x} \right) \Big|_{y_U(x)} + 2n_{U,y} \frac{\partial v_1}{\partial y} \Big|_{y_U(x)} \right] -$$

$$Re[n_{U,y}(p_0 + p_1)|_{y_U(x)}] \quad (4.4d)$$

where $f_{x,visc}$, $f_{y,visc}$, $g_{x,visc}$, $g_{y,visc}$ arise due to the friction, and $f_{x,pres}$, $f_{y,pres}$, $g_{x,pres}$, $g_{y,pres}$ are generated by the pressure. The total force per unit length of the channel acting at the lower wall $F = ((F_{x,visc} + F_{x,pres}), (F_{y,visc} + F_{y,pres}))$ can be expressed as

$$Re F_{x,visc} = Re \left\{ \int_0^{\frac{2\pi}{\alpha}} f_{x,visc} \left[1 + (h'_L)^2 \right]^{\frac{1}{2}} dx \right\} / \lambda, \quad (4.5a-b)$$

$$Re F_{x,pres} = Re \left\{ \int_0^{\frac{2\pi}{\alpha}} f_{x,pres} \left[1 + (h'_L)^2 \right]^{\frac{1}{2}} dx \right\} / \lambda,$$

$$Re F_{y,visc} = Re \left\{ \int_0^{\frac{2\pi}{\alpha}} f_{y,visc} \left[1 + (h'_L)^2 \right]^{\frac{1}{2}} dx \right\} / \lambda, \quad (4.5c-d)$$

$$Re F_{y,pres} = Re \left\{ \int_0^{\frac{2\pi}{\alpha}} f_{y,pres} \left[1 + (h'_L)^2 \right]^{\frac{1}{2}} dx \right\} / \lambda,$$

with the required integrations to be done numerically. Expressions for the total force for one wavelength per unit length of the channel acting on the upper wall $G = ((G_{x,visc} + G_{x,pres}), (G_{y,visc} + G_{y,pres}))$ can be written in a similar manner.

4.2 Mechanics of Drag Generation

A pressure gradient needs to be applied along the channel in order to produce a desired flow rate. We shall refer to this pressure gradient as a pressure loss. The introduction of surface vibration may increase or decrease this pressure loss depending on the vibration amplitude, phase speed, wavelength and flow conditions. The pressure gradient correction can be represented in the form of

$$\frac{\partial p_1}{\partial x} = \frac{\partial p_T}{\partial x} - \frac{\partial p_0}{\partial x} \quad (4.6)$$

where a negative $\partial p_1 / \partial x$ corresponds to an increase of losses while the positive value corresponds to drag decrease.

It is convenient to use small wave number approximation ($\alpha \rightarrow 0$) to discuss the physical processes leading to the drag generation as this approximation yields an analytic solution.

Consider problem (3.2) expressed in terms of the total flow quantities and with a sinusoidal wave propagating along the lower wall resulting in the shape of the flow domain of the form

$$y_U(x) = 1, \quad y_L(x) = -1 + A \cos(\alpha x). \quad (4.7a)$$

The boundary conditions and the flow rate constraint take the form of

$$y = y_U(x): \quad u_T = v_T = 0, \quad (4.7b)$$

$$y = y_L(x): \quad u_T = 0, \quad v_T = c A \alpha \sin(\alpha x), \quad (4.7c)$$

$$\left(\int_{y_L(x)}^{y_U(x)} u_T \, dy \right) \Big|_{mean} = \frac{4}{3}. \quad (4.7d)$$

The solution domain is regularized using transformation of the form

$$\xi = \alpha x, \quad \eta = (y - 1) \left[1 - \frac{1}{2} A \cos(\alpha x) \right]^{-1} + 1 \quad (4.8)$$

which maps the original irregular domain into $\eta \in \langle -1, 1 \rangle$ and introduces a wavelength-based scale in the x -direction which accounts for the flow modulation due to the wave motion. Field equations after transformation take the form

$$\begin{aligned} \frac{\partial^2 u_T}{\partial \eta^2} + [F_1 - F_2(u_T - c) - F_3 v_T] \frac{\partial u_T}{\partial \eta} + F_4 \frac{\partial^2 u_T}{\partial \xi \partial \eta} + \\ F_5 \frac{\partial^2 u_T}{\partial \xi^2} - F_6(u_T - c) \frac{\partial u_T}{\partial \xi} - F_6 \frac{\partial p_T}{\partial \xi} - F_2 \frac{\partial p_T}{\partial \eta} = 0, \end{aligned} \quad (4.9a)$$

$$\begin{aligned} \frac{\partial^2 v_T}{\partial \eta^2} + [F_1 - F_2(u_T - c) - F_3 v_T] \frac{\partial v_T}{\partial \eta} + F_4 \frac{\partial^2 v_T}{\partial \xi \partial \eta} + \\ F_5 \frac{\partial^2 v_T}{\partial \xi^2} - F_6(u_T - c) \frac{\partial v_T}{\partial \xi} - F_3 \frac{\partial p_T}{\partial \eta} = 0, \end{aligned} \quad (4.9b)$$

$$\alpha \frac{\partial u_T}{\partial \xi} + F_7 \frac{\partial u_T}{\partial \eta} + F_8 \frac{\partial v_T}{\partial \eta} = 0, \quad (4.9c)$$

with definitions of the coefficients given in Appendix B. The boundary conditions and the constraint take the form

$$\begin{aligned} u(\xi, 1) = v(\xi, 1) = 0, \quad u(\xi, -1) = 0, \quad v(\xi, -1) = c A \alpha \sin(\xi), \\ \left(\frac{1}{2} G_1 \int_{-1}^1 u_T \, d\eta \right) \Big|_{mean} = \frac{4}{3}. \end{aligned} \quad (4.10a-d)$$

The unknowns can be represented as expansions of the form

$$(u_T, v_T) = (\tilde{u}_0, \tilde{v}_0) + \alpha(\tilde{u}_1, \tilde{v}_1) + O(\alpha^2), \quad p_T = \alpha^{-1}\tilde{p}_{-1} + \tilde{p}_0 + O(\alpha) \quad (4.11)$$

and the flow rate constraint can be expressed as

$$\left(G_1 \int_{\eta=-1}^{\eta=1} [\tilde{u}_0 + \alpha\tilde{u}_1 + O(\alpha^2)] d\eta \right) \Big|_{mean} = \frac{8}{3}. \quad (4.12)$$

The variable coefficients in (4.9) are replaced by their small- α approximations (see Appendix B), (4.11) is substituted into (4.9)-(4.10) and terms of the same orders of magnitude are separated resulting in a sequence of problems with the leading order system being of the form

$$\frac{\partial^2 \tilde{u}_0}{\partial \eta^2} - \frac{1}{2} Re G_1 \tilde{v}_0 \frac{\partial \tilde{u}_0}{\partial \eta} - \frac{1}{4} Re G_1^2 \frac{\partial \tilde{p}_{-1}}{\partial \xi} + \frac{1}{4} Re A \sin(\xi) G_1 (\eta - 1) \frac{\partial \tilde{p}_{-1}}{\partial \eta} = 0, \quad (4.13a)$$

$$\frac{\partial \tilde{p}_{-1}}{\partial \eta} = 0, \quad \frac{\partial \tilde{v}_0}{\partial \eta} = 0, \quad (4.13b-c)$$

$$\tilde{u}_0(\xi, \pm 1) = \tilde{v}_0(\xi, \pm 1) = 0, \quad \left(G_1 \int_{\eta=-1}^{\eta=1} \tilde{u}_0 d\eta \right) \Big|_{mean} = \frac{8}{3}. \quad (4.13d-e)$$

Its solution can be written as

$$\frac{d\tilde{p}_{-1}}{d\xi} = -16Re^{-1}G_1^{-3} + c \, 12 A Re^{-1}G_1^{-3} \cos(\xi), \quad (4.14a)$$

$$\tilde{u}_0 = 2(1 - \eta^2)G_1^{-1} - c \frac{3}{2} A (1 - \eta^2) \cos(\xi)G_1^{-1}, \quad \tilde{v}_0 = 0. \quad (4.14b-c)$$

Integration of (4.14a) gives expression for pressure of the form

$$Re \tilde{p}_{-1} = -\left(4 + \frac{A^2}{2}\right) B(\xi) - \left(8 - \frac{A^2}{2} - 3A \cos(\xi)\right) A \sin(\xi) \left(1 - \frac{A^2}{4}\right)^{-2} G_1^{-2} - \\ c \left\{ -\frac{9}{4} A^2 B(\xi) + \left(\frac{-3A^2 - 24}{4} + \frac{6 + 3A^2}{4} A \cos(\xi) \right) A \sin(\xi) \left(1 - \frac{A^2}{4}\right)^{-2} G_1^{-2} \right\}, \quad (4.14d)$$

where

$$B(\xi) = \left(1 - \frac{A^2}{4}\right)^{-\frac{5}{2}} \left[\arctan \left(\left(1 + \frac{A}{2}\right)^{\frac{1}{2}} \left(1 - \frac{A}{2}\right)^{-\frac{1}{2}} \tan \left(\frac{\xi}{2}\right) \right) + \pi \left\lfloor \frac{\xi + \pi}{2\pi} \right\rfloor \right]. \quad (4.14e)$$

In the above, symbol $\lfloor \dots \rfloor$ stands for the floor function which needs to be added in order to remove spurious discontinuities associated with the arctan function (Jeffrey & Rich 1994). Pressure has been normalized by assuming that $\tilde{p}_{-1} = 0$ at $\xi = 0$. As this point moves in the laboratory frame (it moves as $X = ct$), it is preferable to normalize pressure by selecting its value at a stationary point in the laboratory frame, say at $X = 0$. Pressure normalized in this manner is denoted as $\tilde{\tilde{p}}_{-1}$ and can be expressed as

$$Re \tilde{\tilde{p}}_{-1}(X, t) = Re \tilde{p}_{-1}[\alpha(X - ct)] - Re \tilde{p}_{-1}(-\alpha ct). \quad (4.15)$$

Useful information about \tilde{p}_{-1} can be gained by noting that $d\tilde{p}_{-1}/d\xi$ in (4.14a) is an even function of ξ , expressing it as a Fourier expansion and integrating this expansion with respect to ξ term by term to arrive at the following expression in the moving frame

$$Re \tilde{p}_{-1} = \left(1 - \frac{A^2}{4}\right)^{-\frac{5}{2}} \left[-2 \left(1 + \frac{A^2}{8}\right) + \frac{9}{8} c A^2 \right] \xi + \\ A \left(1 - \frac{A^2}{4}\right)^{-\frac{5}{2}} \left[-3 + \frac{3}{2} c \left(1 + \frac{A^2}{2}\right) \right] \sin(\xi) + \dots \quad (4.16a)$$

and an alternative expression in the laboratory frame

$$Re \tilde{\tilde{p}}_{-1} = \left(1 - \frac{A^2}{4}\right)^{-\frac{5}{2}} \left[-2 \left(1 + \frac{A^2}{8}\right) + \frac{9}{8} c A^2 \right] \alpha X + \\ 2A \left(1 - \frac{A^2}{4}\right)^{-\frac{5}{2}} \left[-3 + \frac{3}{2} c \left(1 + \frac{A^2}{2}\right) \right] \sin \frac{\alpha X}{2} \cos \left(\frac{\alpha X}{2} - \alpha ct \right) + \dots \quad (4.16b)$$

The mean pressure gradient can be directly computed from (4.16).

The next order system has the form

$$\begin{aligned} \frac{\partial^2 \tilde{u}_1}{\partial \eta^2} - \frac{1}{2} Re G_1 \frac{\partial \tilde{u}_0}{\partial \eta} \tilde{v}_1 - \frac{1}{4} Re G_1^2 \frac{\partial \tilde{p}_0}{\partial \xi} + \frac{1}{4} Re A \sin(\xi) G_1 (\eta - 1) \frac{\partial \tilde{p}_0}{\partial \eta} = \\ - \frac{1}{4} Re A \sin(\xi) G_1 (\eta - 1) (\tilde{u}_0 - c) \frac{\partial \tilde{u}_0}{\partial \eta} + \frac{1}{4} Re G_1^2 (\tilde{u}_0 - c) \frac{\partial \tilde{u}_0}{\partial \xi}, \end{aligned} \quad (4.17a)$$

$$\frac{\partial \tilde{p}_0}{\partial \eta} = 0, \quad \frac{\partial \tilde{v}_1}{\partial \eta} = \frac{1}{2} A (\eta - 1) \sin(\xi) \frac{\partial \tilde{u}_0}{\partial \eta} - \frac{1}{2} G_1 \frac{\partial \tilde{u}_0}{\partial \xi}, \quad (4.17b-c)$$

$$\tilde{u}_1(\xi, 1) = \tilde{v}_1(\xi, 1) = 0, \quad \tilde{u}_1(\xi, -1) = 0, \quad \tilde{v}_1(\xi, -1) = c A \sin(\xi), \quad (4.17d-f)$$

$$\left(\int_{\eta=-1}^{\eta=1} \tilde{u}_1 d\eta \right) \Big|_{mean} = 0 \quad (4.17g)$$

and its solution can be written as

$$\begin{aligned} \frac{d \tilde{p}_0}{d \xi} = \frac{96}{35} A \sin(\xi) G_1^{-3} - \frac{c}{35} A \sin(\xi) G_1^{-2} [(36A \cos(\xi) + 216) G_1^{-1} + 28] + \\ \frac{c^2}{35} A \sin(\xi) G_1^{-2} [(-27A^2 \cos^2(\xi) + 162A \cos(\xi)) G_1^{-1} - 21A \cos(\xi) + 84], \end{aligned} \quad (4.18a)$$

$$\begin{aligned} \tilde{u}_1 = Re A \sin(\xi) G_1^{-1} H_8 + c Re A \sin(\xi) [G_1^{-1} A \cos(\xi) H_5 + G_1^{-1} H_6 + H_7] + \\ c^2 Re A \sin(\xi) \left[G_1^{-1} A^2 \cos^2(\xi) H_1 + G_1^{-1} A \cos(\xi) H_2 + \frac{3}{4} A \cos(\xi) H_3 - \frac{3}{4} H_4 \right], \end{aligned} \quad (4.18b)$$

$$\tilde{v}_1 = -2A \sin(\xi) G_1^{-1} H_{11} - c 2G_1^{-1} A \sin(\xi) [H_9 - A \cos(\xi) H_{10}], \quad (4.18c)$$

$$\begin{aligned} Re \tilde{p}_0 = Re \left\{ -\frac{48}{35} G_1^{-2} + \frac{12}{35} \left(1 - \frac{A}{2} \right)^{-2} - \right. \\ \left. \frac{c}{35} \left[-128 G_1^{-2} - 8A \cos(\xi) G_1^{-2} + 2(A + 16) \left(1 - \frac{A}{2} \right)^{-2} \right] + \right. \\ \left. \frac{c^2}{35} \left[(-84 - 12A \cos(\xi)) G_1^{-2} + 3(7 + A) \left(1 - \frac{A}{2} \right)^{-2} - 6 \ln \frac{G_1}{2-A} \right] \right\} \end{aligned} \quad (4.18d)$$

with definitions of the relevant coefficients given in Appendix B. Pressure has been normalized with condition $\tilde{p}_0 = 0$ at $\xi = 0$. Normalization with respect to the laboratory frame can be determined in a similar process to (4.15). It can be shown that \tilde{p}_0 does not contribute to the mean pressure gradient as

$$\left. \frac{d\tilde{p}_0}{d\xi} \right|_{mean} = \frac{1}{2\pi} \int_{-\pi}^{\pi} \frac{d\tilde{p}_0}{d\xi} d\xi = 0 \quad (4.19)$$

which leads to the final expression for the mean pressure gradient of the form

$$Re \left. \frac{dp_T}{dx} \right|_{mean} = -2 \left(1 - \frac{A^2}{4} \right)^{-\frac{5}{2}} \left(1 + \frac{A^2}{8} - \frac{9}{16} c A^2 \right) + O(\alpha^2). \quad (4.20)$$

The pressure gradient correction required in order to maintain the same flow rate in the presence of the waves has the form

$$Re \frac{dp_1}{dx} = Re \left(\frac{dp_T}{dx} - \frac{dp_0}{dx} \right) = -2 \left(1 - \frac{A^2}{4} \right)^{-\frac{5}{2}} \left(1 + \frac{A^2}{8} - \frac{9}{16} c A^2 \right) + 2 + O(\alpha^2). \quad (4.21)$$

Since $A < 2$, the first bracket on the right hand side of (4.21) is always positive and, thus, the pressure gradient correction is negative in the absence of the waves ($c = 0$), i.e. the stationary grooves always increase drag. Drag can be reduced with the waves that propagate in the positive x -direction. The wave speed which completely eliminates drag is referred to as the critical wave speed c_{cr} and is defined as

$$c_{cr} = \frac{16}{9} A^{-2} \left(1 + \frac{A^2}{8} \right). \quad (4.22)$$

Use of waves with $c > c_{cr}$ creates pumping effect sufficient to move the fluid without the need to apply an external pressure gradient.

We shall now describe mechanisms responsible for changes in the drag. In the case of smooth walls the drag is generated only by viscous shear. In the case of stationary corrugations ($c = 0$), pressure contributes to the drag due to the interaction between the surface topography and the pressure field. At the same time, corrugations increase the wetted surface area and alter the distribution of the wall shear stress (Mohammadi & Floryan, 2012b). Moving surface waves ($c \neq 0$) create more complex situation as described below.

Determination of forces acting on the fluid at the walls begins with the specification of the outwards normal unit vectors, i.e.

$$\mathbf{n}_U = (0, 1), \quad \mathbf{n}_L = [-A \alpha \sin(\xi) + O(\alpha^3), -1 + O(\alpha^2)]. \quad (4.23)$$

In the case of the lower wall, use of (4.23) and (4.4a) leads to the x -component of the shear stress of the form

$$\begin{aligned} Re f_{x,visc} = G_1^{-2}[-8 + 6 c A \cos(\xi)] + Re \alpha G_1^{-1} \left\{ \frac{32}{105} A \sin(\xi) G_1^{-1} - \right. \\ \left. c A \sin(\xi) \left[\frac{124}{105} A \cos(\xi) G_1^{-1} - \frac{152}{105} G_1^{-1} + \frac{16}{15} \right] - \right. \\ \left. c^2 A \sin(\xi) \left[-\frac{5}{7} A^2 \cos^2(\xi) G_1^{-1} + \frac{38}{35} A \cos(\xi) G_1^{-1} - \right. \right. \\ \left. \left. \frac{7}{10} A \cos(\xi) - \frac{1}{5} \right] \right\} + O(\alpha^2), \end{aligned} \quad (4.24)$$

and demonstrates that its distribution is fixed with respect to the moving wave. Integration of (4.24) over one wavelength gives the x -component of the shear force per unit length of the channel of the form

$$Re F_{x,visc} = \left(1 - \frac{A^2}{4}\right)^{-\frac{3}{2}} \left(-2 + c \frac{3}{4} A^2\right) + O(\alpha^2). \quad (4.25)$$

The second term on the right hand side of (4.24) does not contribute to this force due to being an odd function of ξ . Equation (4.25) demonstrates that the positive c reduces the magnitude of the shear force until it reaches zero at

$$c_{cr,v} = \frac{8}{3} A^{-2} \quad (4.26)$$

with further increase of c resulting in $F_{x,visc}$ assisting with the fluid pumping. It is interesting to note that $c_{cr,v}$ is never smaller than $2/3$; reduction of A leads to larger $c_{cr,v}$. Distribution of the x -component of the normal stress generated by the pressure has the form

$$Re f_{x,pres} = Re A \sin(\xi) [\tilde{p}_{-1} + \alpha \tilde{p}_0 + O(\alpha^2)] \quad (4.27)$$

and its integration over one wavelength, say from γ to $\gamma + 2\pi$, gives the x -component of the pressure force. Substitution of (4.16a) and (4.18d) into (4.27) and integration show that terms omitted in (4.16a) as well as \tilde{p}_0 do not contribute to $F_{x,pres}$ (integrals of $\sin(\xi)\sin(n\xi)$ with $n > 1$ over one period are zero; integrals of odd functions are zero). As a result $F_{x,pres}$ can be expressed as

$$\begin{aligned} Re F_{x,pres} = Re(F_{x,form} + F_{x,inter}) = \\ A \left(1 - \frac{A^2}{4}\right)^{-\frac{5}{2}} \left[2 + \frac{A^2}{4} - \frac{9}{8}cA^2\right] \cos(\gamma) - \\ A^2 \left(1 - \frac{A^2}{4}\right)^{-\frac{5}{2}} \left[\frac{3}{2} - c\left(\frac{3}{8}A^2 + \frac{3}{4}\right)\right] + O(\alpha^2), \end{aligned} \quad (4.28)$$

where the first term on the right hand side is associated with the mean pressure gradient and is referred to as the form drag (Mohammadi & Floryan, 2012b). This force is a periodic function of γ with the amplitude given by the curly bracket and its sign depends on the segment of the wave being considered, i.e. depends on the value of γ . Positive c decreases its magnitude until it reaches zero at

$$c_{cr,pf} = \frac{4}{9}A^{-2} \left(4 + \frac{A^2}{2}\right). \quad (4.29)$$

Further increase of c changes direction of this force and it begins to assist with the fluid movement rather than opposing it (This argument is correct only if $\cos(\gamma) < 0$). The second term on the right hand side of (4.28) arises out of the interaction of the periodic part of \tilde{p}_{-1} with the surface wave and is referred to as the interaction drag (Mohammadi & Floryan, 2012b). Positive c reduces the magnitude of this force until it reaches zero at

$$c_{cr,pi} = 3 \left(\frac{3}{4}A^2 + \frac{3}{2}\right)^{-1}. \quad (4.30)$$

Further increase of c results in the change of direction so that this force assists with the fluid movement.

Sum of $F_{x,visc}$ and $F_{x,pres}$ gives the x -component of the total force which is reduced when c increases and reaches zero at

$$c_{cr,tot} = A^{-2} \left\{ 4 - A \left(1 - \frac{A^2}{4} \right)^{-1} \left[\left(4 + \frac{A^2}{2} \right) \cos(\gamma) - 3A \right] \right\} \times \\ \left\{ \frac{3}{2} - \left(1 - \frac{A^2}{4} \right)^{-1} \left[\frac{9}{4} A \cos(\gamma) - \left(\frac{3}{4} A^2 + \frac{3}{2} \right) \right] \right\}^{-1}. \quad (4.31)$$

Figure 4.1 displays variations of the critical wave speeds as functions of A .

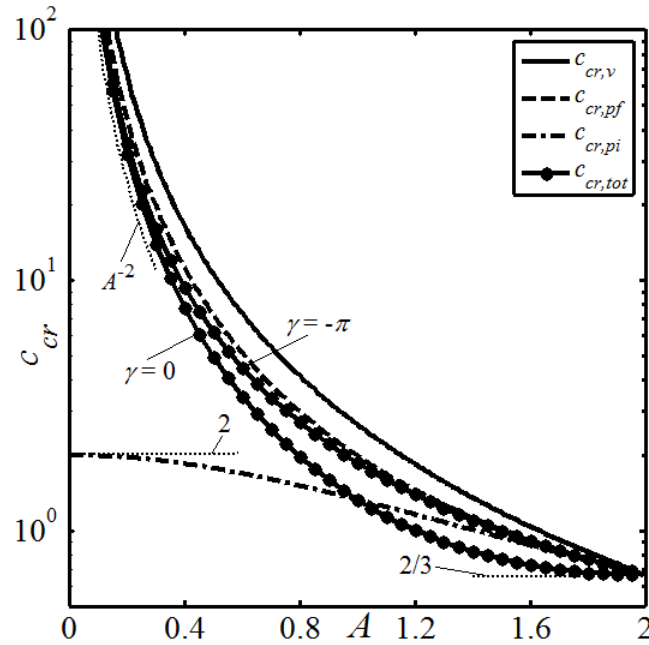


Figure 4.1: Variations of the critical wave speed of the long wavelength waves as a function of the wave amplitude A for waves with profile described by Eq. (4.7).

The reader may note that the critical wave speeds are never smaller than $2/3$ and $c_{cr,v}$, $c_{cr,pf}$, $c_{cr,tot}$ increase rapidly when $A \rightarrow 0$. Point $A = 0$ represents a limit point for which c plays no role. Figure 4.2 displays variations of the total surface force and all its components as functions of c for selected values of A . It can be seen that these forces, regardless of their origin, assist with the fluid motion if c is large enough.

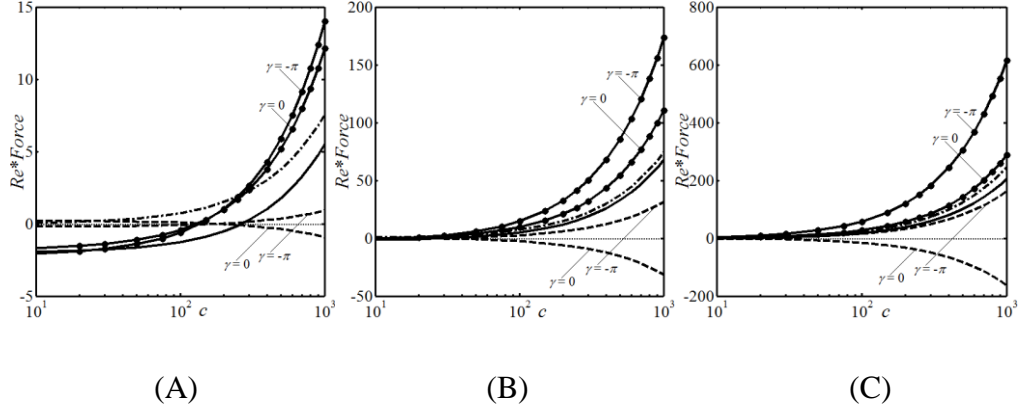


Figure 4.2: Variations of forces acting on the fluid at the lower wall in the limit of $\alpha \rightarrow 0$ as functions of the wave speed c for the wave form described by Eq. (4.7) with: (A) $A = 0.1$; (B) $A = 0.3$; (C) $A = 0.5$. Solid, dashed, dash-dotted lines and lines with circles on them correspond to $Re * F_{x,visc}$, $Re * F_{x,form}$, $Re * F_{x,inter}$, and $Re * F_{x,total}(= Re * (F_{x,visc} + F_{x,form} + F_{x,inter}))$, respectively.

We shall conclude this discussion by describing the y -component of surface forces acting on the fluid. We start with (4.23) and (4.4b) to get the y -component of the shear stress

$$Re f_{y,visc} = \alpha A G_1^{-2} [8 \sin(\xi) - 3c A \sin(2\xi)] + O(\alpha^2) \quad (4.32)$$

and note that its distribution is fixed with respect to the wave. Integration of (4.32) over one wavelength demonstrates that $F_{y,visc} = O(\alpha^2)$, i.e. viscous forces can be neglected at this level of approximation. The y -component of the normal stress generated by the pressure has the form

$$Re f_{y,pres} = Re[\alpha^{-1} \tilde{p}_{-1} + \tilde{p}_0 + O(\alpha)]. \quad (4.33)$$

Substitution of (4.18d) and (4.16a) into (4.33) and integration over one wavelength show that only the linear term from \tilde{p}_{-1} as well as \tilde{p}_0 bring nonzero contributions to the total force per unit length of the channel, i.e.

$$Re F_{y,pres} = -\alpha^{-1} 2(\gamma + \pi) \left(1 - \frac{A^2}{4}\right)^{-\frac{5}{2}} \left(1 + \frac{A^2}{8} - c \frac{9}{16} A^2\right) -$$

$$\begin{aligned}
& \frac{12}{35} Re \left[\left(1 - \frac{A^2}{4}\right)^{-\frac{3}{2}} - \left(1 - \frac{A}{2}\right)^{-2} \right] + \\
& c \frac{2}{35} Re \left[\left(16 + \frac{A^2}{2}\right) \left(1 - \frac{A^2}{4}\right)^{-\frac{3}{2}} - (16 + A) \left(1 - \frac{A}{2}\right)^{-2} \right] - \\
& c^2 \frac{3}{35} Re \left[\left(7 + \frac{A^2}{2}\right) \left(1 - \frac{A^2}{4}\right)^{-\frac{3}{2}} - (7 + A) \left(1 - \frac{A}{2}\right)^{-2} + \right. \\
& \left. 2 \ln \left[\left(1 + \left(1 - \frac{A^2}{4}\right)^{\frac{1}{2}}\right) (2 - A)^{-1} \right] \right] + O(\alpha). \tag{4.34}
\end{aligned}$$

The dominant (first) term on the right hand side is reduced to zero at $c = (16/9)A^{-2}(1 + A^2/8)$. Variations of the second term are more complex as it is a quadratic function of c . The reader may note the dependence of $F_{y,pres}$ on γ .

Determination of forces acting at the upper wall follows a similar process; $g_{x,visc}$ as well as $G_{x,visc}$ are both the same as at the lower wall, i.e. $g_{x,visc} = f_{x,visc}$, $G_{x,visc} = F_{x,visc}$. Pressure does not generate any forces in the x -direction but generates force in the y -direction that is equal and opposite to the pressure force at the lower wall, i.e. $G_{x,pres} = 0$, $G_{y,pres} = -F_{y,pres}$.

We complete this discussion by assessing the range of validity of the small- α solution. To do so, we compare pressure gradient corrections determined analytically and numerically. The error has been defined as a norm of the form

$$\left\| \frac{dp_1}{dx} \right\|_{max} = \sup \left| \left(\frac{dp_1}{dx} \right)_a - \left(\frac{dp_1}{dx} \right)_c \right|, \tag{4.30}$$

where subscripts ‘‘a’’ and ‘‘c’’ correspond to the asymptotic and complete solutions, respectively. Results displayed in Figure 4.3 demonstrate that the range of validity of the asymptotic solution extends up to $\alpha = O(1)$ if Re is small ($Re = 0.1$); at $Re = 200$ this range decreases to $\alpha = O(10^{-1})$.

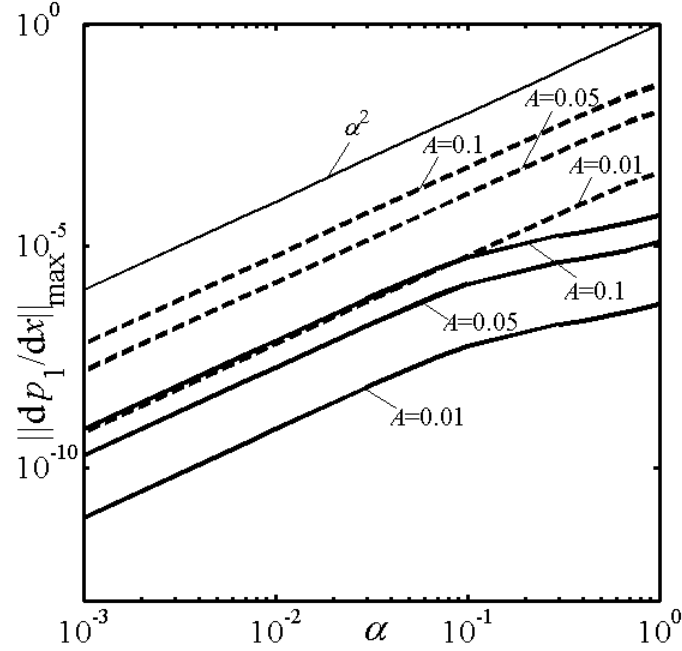


Figure 4.3: Variations of the norm $\|dp_1/dx\|_{max}$ as a function of the wave number α for the flow Reynolds numbers $Re = 0.1$ (dashed lines) and $Re = 200$ (solid lines) and phase speed $c = 1.3$.

4.3 Waves with Small Amplitudes

Further insight into the mechanics of the flow response can be gained by considering waves with small amplitudes. We start with the model problem described by Eq. (4.7) and regularize the solution domain using a transformation of the form

$$\xi = x, \quad \eta = (y - 1) \left[1 - \frac{1}{2} A \cos(\alpha x) \right]^{-1} + 1. \quad (4.31)$$

Field equations after transformation take the form

$$\begin{aligned} \frac{\partial^2 u_T}{\partial \eta^2} + [I_1 - I_2(u_T - c) - I_3 v_T] \frac{\partial u_T}{\partial \eta} + I_4 \frac{\partial^2 u_T}{\partial \xi \partial \eta} + \\ I_5 \frac{\partial^2 u_T}{\partial \xi^2} - I_6(u_T - c) \frac{\partial u_T}{\partial \xi} - I_6 \frac{\partial p_T}{\partial \xi} - I_2 \frac{\partial p_T}{\partial \eta} = 0, \end{aligned} \quad (4.32a)$$

$$\begin{aligned} \frac{\partial^2 v_T}{\partial \eta^2} + [I_1 - I_2(u_T - c) - I_3 v_T] \frac{\partial v_T}{\partial \eta} + I_4 \frac{\partial^2 v_T}{\partial \xi \partial \eta} + \\ I_5 \frac{\partial^2 v_T}{\partial \xi^2} - I_6(u_T - c) \frac{\partial v_T}{\partial \xi} - I_3 \frac{\partial p_T}{\partial \eta} = 0, \end{aligned} \quad (4.32b)$$

$$\frac{\partial u_T}{\partial \xi} + I_7 \frac{\partial u_T}{\partial \eta} + I_8 \frac{\partial v_T}{\partial \eta} = 0, \quad (4.32c)$$

$$\begin{aligned} u(\xi, 1) = v(\xi, 1) = 0, \quad u(\xi, -1) = 0, \quad v(\xi, -1) = c A \alpha \sin(\alpha \xi), \\ \left(\frac{1}{2} L_1 \int_{-1}^1 u_T d\eta \right) \Big|_{mean} = \frac{4}{3} \end{aligned} \quad (4.32d)$$

with definitions of all coefficients given in Appendix C. Assume that the waves have very small amplitude, i.e. $A \rightarrow 0$. The unknowns can be represented as expansions of the form

$$\begin{aligned} (u_T, v_T) = (\tilde{u}_0, \tilde{v}_0) + A(\tilde{u}_1, \tilde{v}_1) + A^2(\tilde{u}_2, \tilde{v}_2) + O(A^3), \\ p_T = \tilde{p}_0 + A\tilde{p}_1 + A^2\tilde{p}_2 + O(A^3), \end{aligned} \quad (4.33)$$

and the flow rate constraint can be expressed as

$$\left(L_1 \int_{\eta=-1}^{\eta=1} [\tilde{u}_0 + A\tilde{u}_1 + A^2\tilde{u}_2 + O(A^3)] d\eta \right) \Big|_{mean} = \frac{8}{3}. \quad (4.34)$$

Substitution of (4.33) into (4.32) and separation of terms of the same orders of magnitude result in a sequence of problems with the leading order system having the form of

$$\frac{\partial^2 \tilde{u}_0}{\partial \eta^2} - Re \tilde{v}_0 \frac{\partial \tilde{u}_0}{\partial \eta} + \frac{\partial^2 \tilde{u}_0}{\partial \xi^2} - Re(\tilde{u}_0 - c) \frac{\partial \tilde{u}_0}{\partial \xi} - Re \frac{\partial \tilde{p}_0}{\partial \xi} = 0, \quad (4.35a)$$

$$\frac{\partial^2 \tilde{v}_0}{\partial \eta^2} - Re \tilde{v}_0 \frac{\partial \tilde{v}_0}{\partial \eta} + \frac{\partial^2 \tilde{v}_0}{\partial \xi^2} - Re(\tilde{u}_0 - c) \frac{\partial \tilde{v}_0}{\partial \xi} - Re \frac{\partial \tilde{p}_0}{\partial \eta} = 0, \quad \frac{\partial \tilde{u}_0}{\partial \xi} + \frac{\partial \tilde{v}_0}{\partial \eta} = 0, \quad (4.35b-c)$$

$$\tilde{u}_0(\xi, \pm 1) = \tilde{v}_0(\xi, \pm 1) = 0, \quad \int_{\eta=-1}^{\eta=1} \tilde{u}_0 d\eta = \frac{4}{3}. \quad (4.35d-e)$$

It can be shown that solution of (4.35) has the form

$$\frac{d\tilde{p}_0}{d\xi} = -2Re^{-1}, \quad \tilde{u}_0 = 1 - \eta^2, \quad \tilde{v}_0 = 0, \quad \tilde{p}_0 = -2Re^{-1}\xi \quad (4.36a-d)$$

where pressure has been normalized with condition $\tilde{p}_0 = 0$ at $\xi = 0$.

System $O(A)$ has the form

$$\frac{\partial^2 \tilde{u}_1}{\partial \eta^2} + \frac{\partial^2 \tilde{u}_1}{\partial \xi^2} - Re(1 - c - \eta^2) \frac{\partial \tilde{u}_1}{\partial \xi} + 2Re \tilde{v}_1 \eta - Re \frac{\partial \tilde{p}_1}{\partial \xi} =$$

$$\cos(\alpha \xi)[2 - \alpha^2(\eta^2 - \eta)] - \alpha Re \sin(\alpha \xi)[\eta^4 - \eta^3 + (c - 1)\eta^2 + (1 - c)\eta], \quad (4.37a)$$

$$\frac{\partial^2 \tilde{v}_1}{\partial \eta^2} + \frac{\partial^2 \tilde{v}_1}{\partial \xi^2} - Re(1 - c - \eta^2) \frac{\partial \tilde{v}_1}{\partial \xi} - Re \frac{\partial \tilde{p}_1}{\partial \eta} = 0,$$

$$\frac{\partial \tilde{u}_1}{\partial \xi} + \frac{\partial \tilde{v}_1}{\partial \eta} = -\alpha \sin(\alpha \xi)(\eta^2 - \eta), \quad (4.37b-c)$$

$$\tilde{u}_1(\xi, 1) = \tilde{v}_1(\xi, 1) = 0, \quad \tilde{u}_1(\xi, -1) = 0, \quad \tilde{v}_1(\xi, -1) = c \alpha \sin(\alpha \xi), \quad (4.37d-f)$$

$$\int_{\eta=-1}^{\eta=1} \tilde{u}_1 d\eta = \left(\frac{2}{3} - c\right) \cos(\alpha \xi). \quad (4.37g)$$

The solution of (4.37) has the form

$$[\tilde{u}_1(\xi, \eta), \tilde{v}_1(\xi, \eta), \tilde{p}_1(\xi, \eta)] = [\tilde{u}_1^{(1)}(\eta), \tilde{v}_1^{(1)}(\eta), \tilde{p}_1^{(1)}(\eta)] e^{i\alpha \xi} +$$

$$[\tilde{u}_1^{(-1)}(\eta), \tilde{v}_1^{(-1)}(\eta), \tilde{p}_1^{(-1)}(\eta)] e^{-i\alpha \xi}, \quad (4.38)$$

where $\tilde{u}_1^{(-1)}, \tilde{v}_1^{(-1)}, \tilde{p}_1^{(-1)}$ are complex conjugates of $\tilde{u}_1^{(1)}, \tilde{v}_1^{(1)}, \tilde{p}_1^{(1)}$. Substitution of (4.38) into (4.37), separation of Fourier modes and elimination of $\tilde{u}_1^{(1)}$ and $\tilde{p}_1^{(1)}$ lead to the problem for $\tilde{v}_1^{(1)}$ of the form

$$D^4 \tilde{v}_1^{(1)} + \alpha[-i Re(1 - c - \eta^2) - 2\alpha] D^2 \tilde{v}_1^{(1)} +$$

$$\alpha[\alpha^3 + i \alpha^2 Re(1 - c - \eta^2) - 2i Re] \tilde{v}_1^{(1)} = 0, \quad (4.39a)$$

$$\tilde{v}_1^{(1)}(1) = 0, \quad \tilde{v}_1^{(1)}(-1) = -\frac{1}{2} i c \alpha, \quad D \tilde{v}_1^{(1)}(1) = 0, \quad D \tilde{v}_1^{(1)}(-1) = i \alpha, \quad (4.39b-e)$$

where $D = d/d\eta$. System (4.39) has been solved numerically using the standard Galerkin method and $\tilde{u}_1^{(1)}$ and $\tilde{p}_1^{(1)}$ have been determined a posteriori using the following formulae

$$\tilde{u}_1^{(1)} = i \alpha^{-1} D \tilde{v}_1^{(1)} + \frac{1}{2}(\eta^2 - \eta), \quad (4.40a)$$

$$\begin{aligned} Re \tilde{p}_1^{(1)} &= \alpha^{-2} D^3 \tilde{v}_1^{(1)} + \\ &Re[-i \alpha^{-1}(1 - c - \eta^2) - Re^{-1}] D \tilde{v}_1^{(1)} - 2i Re \alpha^{-1} \eta \tilde{v}_1^{(1)}. \end{aligned} \quad (4.40b)$$

System $O(A^2)$ has the form

$$\begin{aligned} \frac{\partial^2 \tilde{u}_2}{\partial \eta^2} + \frac{\partial^2 \tilde{u}_2}{\partial \xi^2} - Re(1 - c - \eta^2) \frac{\partial \tilde{u}_2}{\partial \xi} + 2Re \eta \tilde{v}_2 - Re \frac{\partial \tilde{p}_2}{\partial \xi} = \\ \left\{ \frac{1}{2} \alpha^2 \cos(\alpha \xi)(\eta - 1) - \frac{1}{2} \alpha Re \sin(\alpha \xi)[- \eta^3 + \eta^2 + (1 - c)\eta + c - 1] + Re \tilde{v}_1 \right\} \frac{\partial \tilde{u}_1}{\partial \eta} + \\ Re[\tilde{u}_1 - \cos(\alpha \xi)(1 - c - \eta^2)] \frac{\partial \tilde{u}_1}{\partial \xi} + \\ \alpha \left\{ Re \sin(\alpha \xi) \tilde{u}_1 + \frac{1}{2} \alpha [\cos^2(\alpha \xi) + 2\sin^2(\alpha \xi)] \right\} (\eta^2 - \eta) + \\ \alpha \sin(\alpha \xi)(\eta - 1) \frac{\partial^2 \tilde{u}_1}{\partial \xi \partial \eta} + \cos(\alpha \xi) \frac{\partial^2 \tilde{u}_1}{\partial \xi^2} + Re \cos(\alpha \xi) \eta \tilde{v}_1 - \\ Re \cos(\alpha \xi) \frac{\partial \tilde{p}_1}{\partial \xi} - \frac{1}{2} \alpha Re \sin(\alpha \xi)(\eta - 1) \frac{\partial \tilde{p}_1}{\partial \eta} + \\ \frac{1}{2} \{ \alpha Re \sin(\alpha \xi) \cos(\alpha \xi) [\eta^4 - \eta^3 + (c - 1)\eta^2 + (1 - c)\eta] - \\ \cos^2(\alpha \xi) + \alpha^2 \sin^2(\alpha \xi)(\eta - 1)^2 \}, \end{aligned} \quad (4.41a)$$

$$\begin{aligned} \frac{\partial^2 \tilde{v}_2}{\partial \eta^2} + \frac{\partial^2 \tilde{v}_2}{\partial \xi^2} - Re(1 - c - \eta^2) \frac{\partial \tilde{v}_2}{\partial \xi} - Re \frac{\partial \tilde{p}_2}{\partial \eta} = \\ \left\{ \frac{1}{2} \alpha^2 \cos(\alpha \xi)(\eta - 1) - \frac{1}{2} \alpha Re \sin(\alpha \xi)[- \eta^3 + \eta^2 + (1 - c)\eta + c - 1] + Re \tilde{v}_1 \right\} \frac{\partial \tilde{v}_1}{\partial \eta} + \\ \alpha \sin(\alpha \xi)(\eta - 1) \frac{\partial^2 \tilde{v}_1}{\partial \xi \partial \eta} + \cos(\alpha \xi) \frac{\partial^2 \tilde{v}_1}{\partial \xi^2} + \end{aligned}$$

$$Re[\tilde{u}_1 - \cos(\alpha\xi)(1 - c - \eta^2)] \frac{\partial \tilde{v}_1}{\partial \xi} - \frac{1}{2} Re \cos(\alpha\xi) \frac{\partial \tilde{p}_1}{\partial \eta}, \quad (4.41b)$$

$$\begin{aligned} \frac{\partial \tilde{u}_2}{\partial \xi} + \frac{\partial \tilde{v}_2}{\partial \eta} &= \frac{1}{2} \alpha \sin(\alpha\xi)(\eta - 1) \frac{\partial \tilde{u}_1}{\partial \eta} - \frac{1}{2} \cos(\alpha\xi) \frac{\partial \tilde{v}_1}{\partial \eta} - \\ &\quad \frac{1}{2} \alpha \sin(\alpha\xi) \cos(\alpha\xi)(\eta^2 - \eta), \end{aligned} \quad (4.41c)$$

$$\tilde{u}_2(\xi, \pm 1) = \tilde{v}_2(\xi, \pm 1) = 0, \quad \int_{\eta=-1}^{\eta=1} \tilde{u}_2 d\eta = \left(\frac{1}{3} - \frac{1}{2}c\right) \cos^2(\alpha\xi). \quad (4.41d-e)$$

The solution of (4.41) has the form

$$[\tilde{u}_2(\xi, \eta), \tilde{v}_2(\xi, \eta), \tilde{p}_2(\xi, \eta) - A_{pc}\xi] = \sum_{n=-2}^{n=2} [\tilde{u}_2^{(n)}(\eta), \tilde{v}_2^{(n)}(\eta), \tilde{p}_2^{(n)}(\eta)] e^{in\alpha\xi}. \quad (4.42)$$

Substitution of (4.42) into (4.41) and extraction of mode zero leads to the following system

$$D^2 \tilde{u}_2^{(0)} + 2Re \eta \tilde{v}_2^{(0)} - Re A_{pc} = g_1, \quad D^2 \tilde{v}_2^{(0)} - Re D \tilde{p}_2^{(0)} = g_2, \quad D \tilde{v}_2^{(0)} = g_3, \quad (4.43a-c)$$

$$\tilde{u}_2^{(0)}(\xi, \pm 1) = \tilde{v}_2^{(0)}(\xi, \pm 1) = 0, \quad \int_{\eta=-1}^{\eta=1} \tilde{u}_2^{(0)} d\eta = \frac{1}{6} - \frac{1}{4}c \quad (4.43d-e)$$

with definitions of the relevant functions given in Appendix C. System (4.43) can be solved resulting in

$$\tilde{v}_2^{(0)} = -\frac{1}{4}(\eta - 1)D(\tilde{v}_1^{(-1)} + \tilde{v}_1^{(1)}), \quad (4.44a)$$

$$\tilde{u}_2^{(0)} = \frac{1}{2} Re A(\eta^2 - 1) + \int_{-1}^{\eta} K(\theta) d\theta - \frac{1}{2}(\eta + 1) \int_{-1}^1 K(\eta) d\eta, \quad (4.44b)$$

$$Re \tilde{p}_2^{(0)} = -\frac{1}{4}[(\eta - 1)(D^2 - \alpha^2) + D](\tilde{v}_1^{(-1)} + \tilde{v}_1^{(1)}) +$$

$$\frac{1}{4} \alpha^2 \int (\tilde{v}_1^{(-1)} + \tilde{v}_1^{(1)}) d\eta - Re \tilde{v}_1^{(-1)} \tilde{v}_1^{(1)} -$$

$$\frac{1}{4} i \alpha Re[-\eta^3 + \eta^2 + c(1 - \eta) + \eta - 1](\tilde{v}_1^{(-1)} - \tilde{v}_1^{(1)}) -$$

$$i \alpha Re \int (\tilde{u}_1^{(-1)} \tilde{v}_1^{(1)} - \tilde{u}_1^{(1)} \tilde{v}_1^{(-1)}) d\eta +$$

$$\begin{aligned} & \frac{1}{4} i \alpha Re \int \left[(-\eta^2 + 2\eta + c - 1) \left(\tilde{v}_1^{(-1)} - \tilde{v}_1^{(1)} \right) \right] d\eta \\ & + \frac{1}{4} Re \left(\tilde{p}_1^{(-1)} + \tilde{p}_1^{(1)} \right) + const, \end{aligned} \quad (4.44c)$$

$$Re A_{pc} = \frac{3}{2} \int_{-1}^1 \left[\int_{-1}^{\eta} K(\theta) d\theta \right] d\eta - \frac{3}{12} + \frac{3}{8} c, \quad (4.44d)$$

where

$$K(\eta) = \int_{-1}^{\eta} \left[g_1 - 2Re \eta v_2^{(0)} \right] d\eta. \quad (4.44e)$$

4.4 Arbitrary Waves

We shall now discuss the system response to waves with arbitrary form, amplitude and wave speed. We start with the sinusoidal waves described by Eq. (4.7).

4.4.1 Sinusoidal Waves on One Wall

The overall channel geometry is described as

$$Y_U = 1, \quad Y_L = -1 + A \cos[\alpha(X - ct)] \quad (4.45a)$$

which, after the Galileo transformation, can be expressed as

$$y_U = 1, \quad y_L = -1 + A \cos(\alpha x). \quad (4.45b)$$

Figure 4.4 illustrates the variations of the pressure gradient correction $Re(dp_1/dx)$ as a function of the phase speed c .

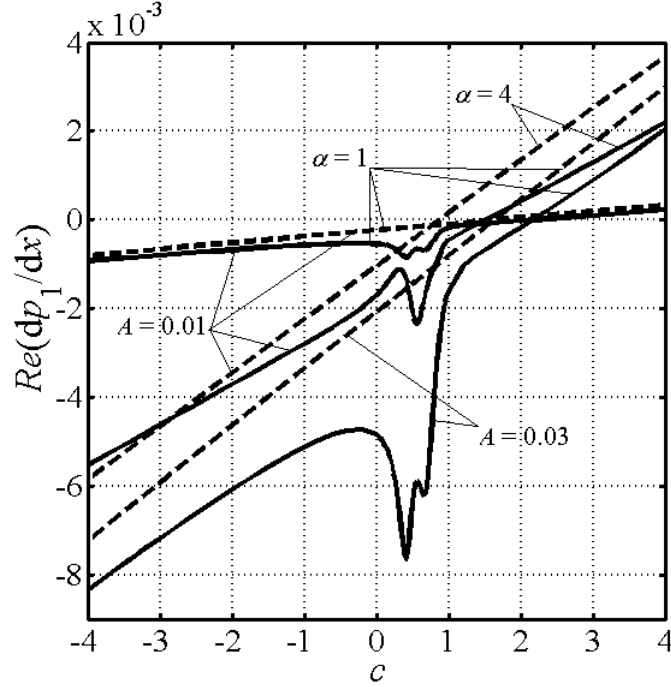


Figure 4.4: Variations of $Re(dp_1/dx)$ as a function of phase speed c for the wave form defined by (4.45) for selected α and A . Dashed and solid lines correspond to $Re = 1$ and $Re = 200$, respectively.

The stationary corrugation ($c = 0$) represents the reference case. Such corrugation generates pressure losses whose magnitude increases with an increase of both A and α . The drag decreases for waves propagating in the downstream directions with a sufficiently high phase speed, and the magnitude of the decrease is larger for waves with larger α and A . The qualitative character of the system response is not affected by the Reynolds number in the range of Re studied but the quantitative character is affected by Re as the surface vibrations are more effective in reducing drag at small Re . In general, the pressure gradient correction increases with c , from negative values at negative c to positive values at large enough c . This pattern is altered for $c \in (0,1)$ but only when Re is large enough. The reader may note that in such case the wave speed is equal to the fluid velocity in the interior of the channel. Results displayed in Figure 4.4 demonstrate that use of waves with certain values of c in this range results in a significant drag increase, and this increase is larger for larger A . Results displayed in Figure 4.5 demonstrate that the drag increase occurs only for $\alpha = O(1)$ with the largest effect taking place when $\alpha \in$

(2,3). A sufficient reduction of α eliminates this effect as well as a sufficient increase of α .

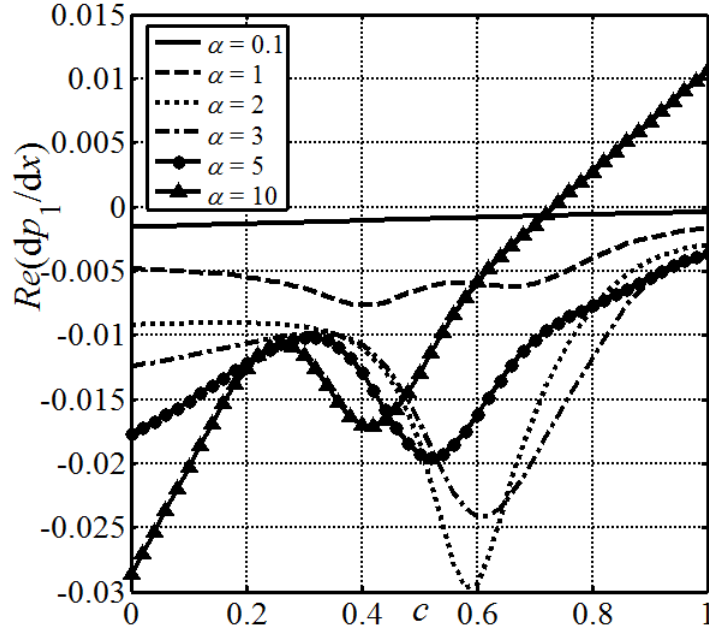


Figure 4.5: Variations of $Re(dp_1/dx)$ as a function of the phase speed c for the wave profile defined by (4.45) with $Re = 200$ and $A = 0.03$, and different wave numbers α .

We are interested in determining the source for the strange behavior occurring when $c \in (0,1)$. We choose conditions the same as the dotted line in Figure 4.5. We shall look at the variations of forces per unit length of the channel acting on the fluid in this range as well as the velocity fields for selected values of wave speed. Figure 4.5 displays variations of forces per unit length of the channel acting on the fluid at the upper and lower walls as functions of the wave speed c . It can be seen that the x -component of pressure force acting on the fluid at the lower wall has a positive value. This value drops rapidly in the range of $c \in (0.4,0.6)$ when wave propagates with a phase speed similar to the flow velocity. In addition the x -component of viscous force acting on the fluid at lower wall has a negative value which becomes less opposing in the range mentioned above. The total effect can be determined by the variations of $F_{x,total}$. It has been shown that $F_{x,total}$ reaches the most negative value at $c \approx 0.58$ which justifies the drag increase observed in Figure 4.5. The situation is the same at the upper wall except that the x -

component of pressure force acting on the fluid at upper wall is zero due to the upper wall being smooth.

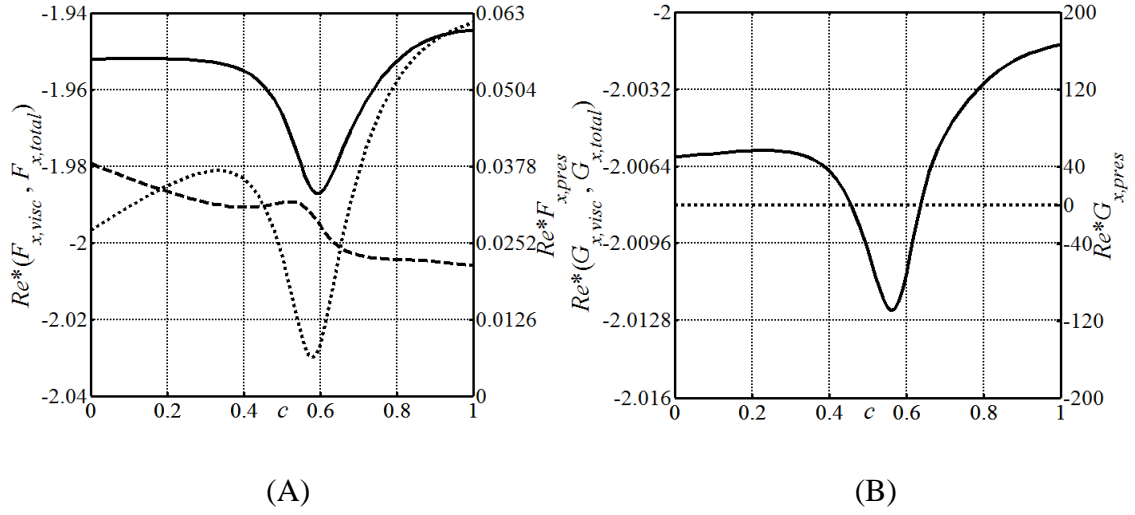
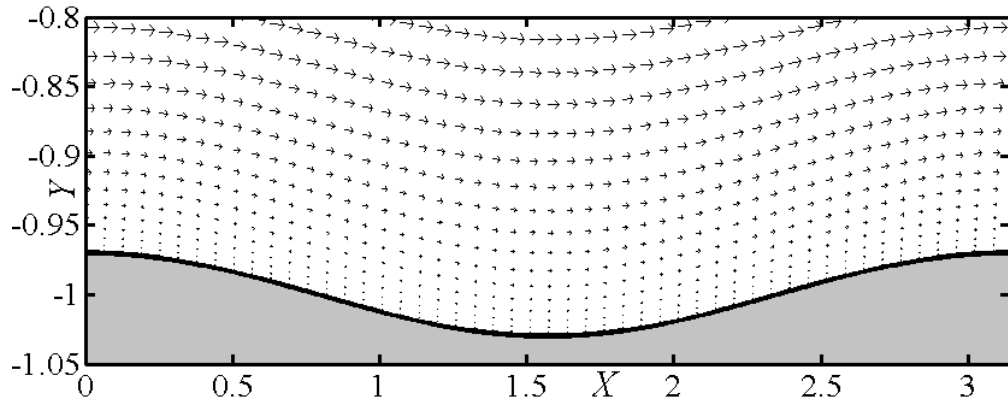


Figure 4.6: Variations of forces per unit length of the channel acting on the fluid at (A) the lower and (B) the upper walls as functions of the wave speed c for the wave form described by Eq. (4.45) with Reynolds number $Re = 200$, wave amplitude $A = 0.03$, and wave number $\alpha = 2$. Dashed, dotted, and solid lines correspond to viscous forces $(F_{x,visc}, G_{x,visc})$, pressure forces $(F_{x,pres}, G_{x,pres})$, and total forces $(F_{x,total} = F_{x,visc} + F_{x,pres}, G_{x,total} = G_{x,visc} + G_{x,pres})$, respectively.

Figure 4.7 illustrates the velocity field near the lower wall in a vibrating channel with the same conditions as in Figure 4.6 for selected values of wave speed and, thus, provides a more direct tool for assessment of different types of vibrations.



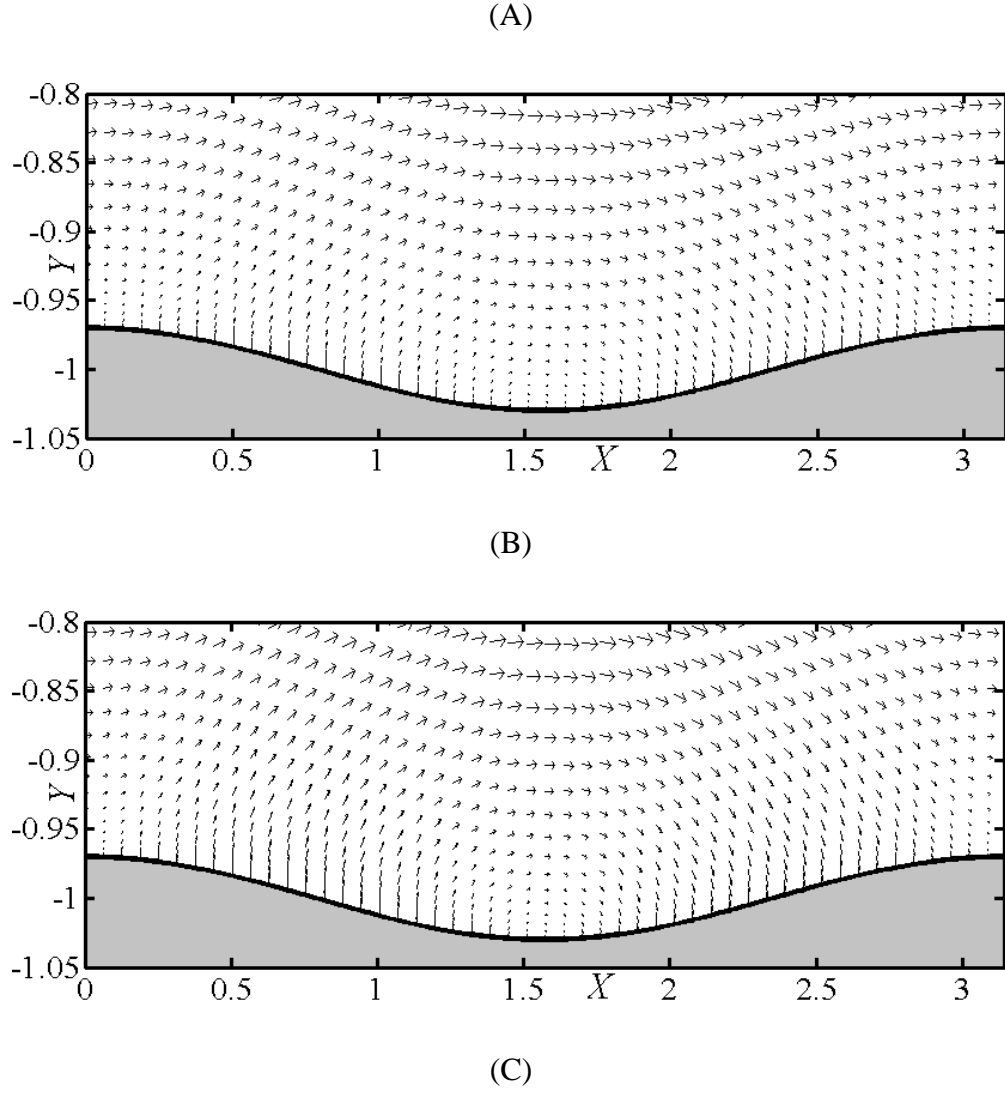


Figure 4.7: Plots of velocity field in a vibrating channel whose geometry is described by Eq. (4.45) with $\alpha = 2$, $A = 0.03$, $Re = 200$. Figures 4.7 A–C correspond to $c = 0$, $c = 0.58$, and $c = 1$, respectively.

Figure 4.8 illustrates plots of pressure field for conditions the same as Figure 4.7 but for $Re = 1$. Pressure has been normalized by assuming that $p_T = 0$ at $(X, Y) = (0, 0)$. This figure may provide useful information.

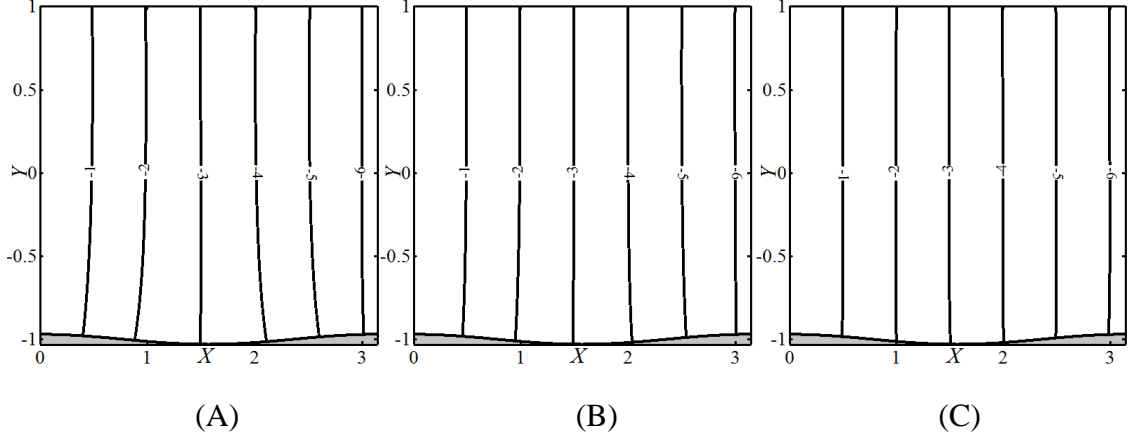


Figure 4.8: Plots of $Re * p_T$ in a vibrating channel whose geometry is described by Eq. (4.45) with $\alpha = 2$, $A = 0.03$, $Re = 1$. Figures 4.8 A–C correspond to $c = 0$, $c = 0.58$, and $c = 1$, respectively.

Figure 4.9 illustrates plots of pressure field for conditions the same as Figure 4.7.

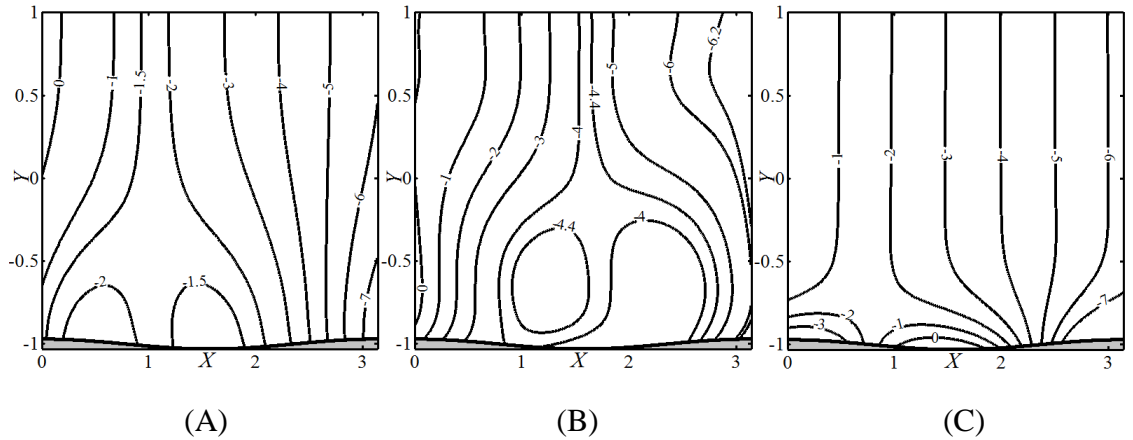


Figure 4.9: Plots of $Re * p_T$ in a vibrating channel whose geometry is described by Eq. (4.45) with $\alpha = 2$, $A = 0.03$, $Re = 200$. Figures 4.9 A–C correspond to $c = 0$, $c = 0.58$, and $c = 1$, respectively.

Effects of α can be assessed using the results displayed in Figure 4.10. The magnitude of the drag reduction increases nearly monotonically with an increase of both the phase speed c and the wave number α and the thick line separates the drag-increasing and the drag-reducing waves. Such smooth variations are replaced with the rapid re-adjustment for $c \in (0,1)$ and $\alpha > 0.8$ and a “local” increase of the drag, but only when Re is high enough.

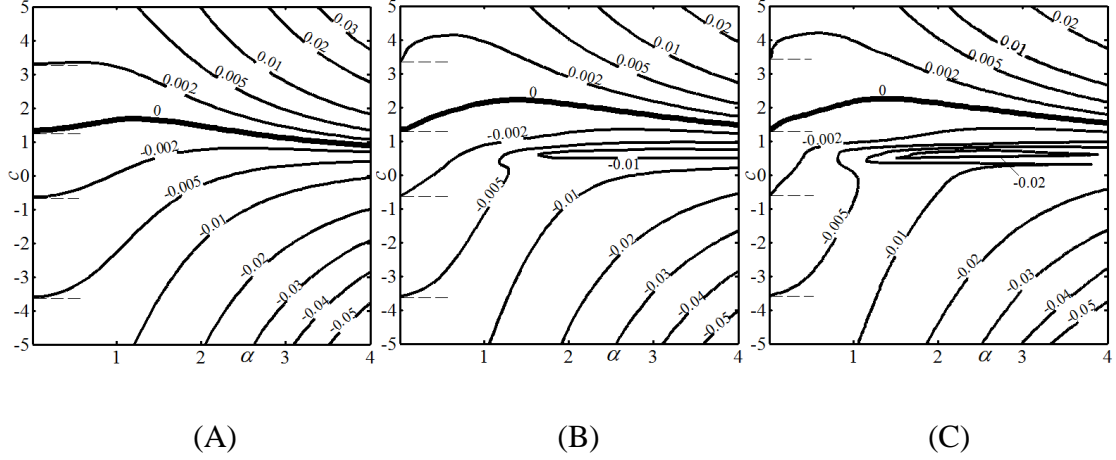


Figure 4.10: Variations of $Re(dp_1/dx)$ as a function of the phase speed c and the wave number α for the wave form defined by (6.1) with $A = 0.03$ and: (A) $Re = 1$; (B) $Re = 100$; (C) $Re = 200$.

We shall look again at different effects contributing to the creation of forces acting on the fluid. Figures 4.11–4.13 display the distributions of $f_{x,visc}$, $f_{x,form}$, $f_{x,inter}$, and $g_{x,visc}$ as well as their mean values for different Reynolds numbers and for waves with different phase speeds. Subscripts x, v and x, f and x, i correspond to x -component of viscous, form, and interaction forces, respectively. Subscript m identifies mean values.

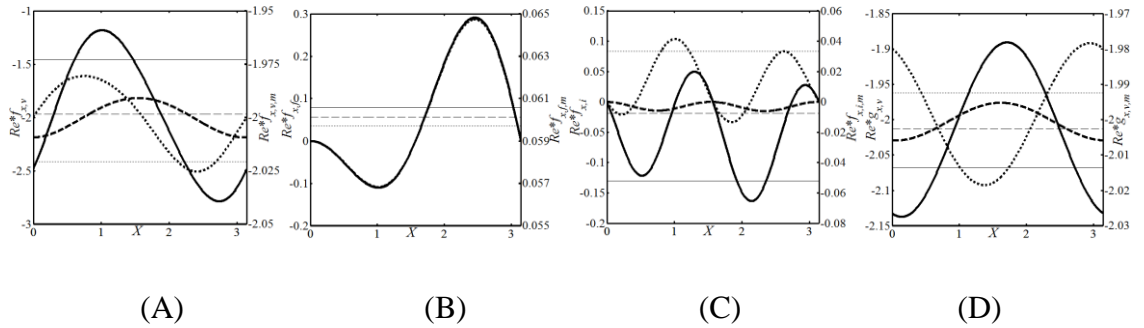


Figure 4.11: Distributions of (A) the x -component of the shear force $f_{x,visc}$ and (B) the x -component of the form force $f_{x,form}$ and (C) the x -component of the interaction force $f_{x,inter}$ acting on the fluid at the lower wall and (D) the x -component of the shear force $g_{x,visc}$ acting on the fluid at the upper wall for the wave profile described by (4.45) with $A = 0.03$, $Re = 1$, and $\alpha = 2$. The solid, dashed, and dotted lines correspond to $c = -5$,

$c = 0$, and $c = 5$, respectively. Thick and thin lines identify local and mean values, respectively.

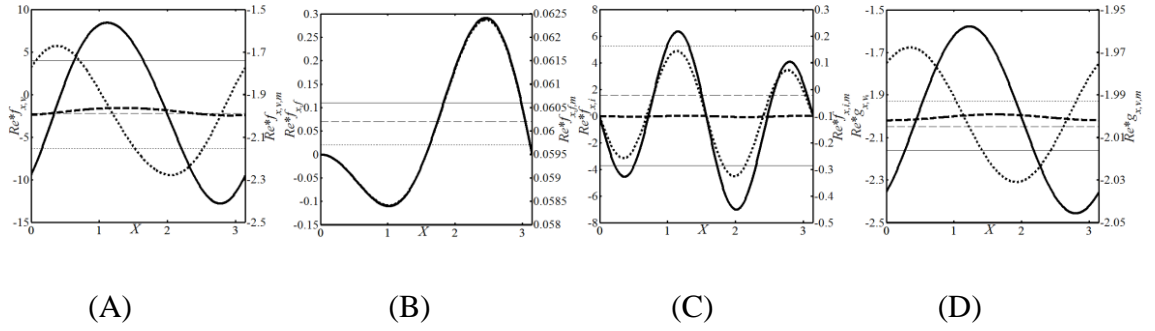


Figure 4.12: Distributions of (A) the x -component of the shear force $f_{x,visc}$ and (B) the x -component of the form force $f_{x,form}$ and (C) the x -component of the interaction force $f_{x,inter}$ acting on the fluid at the lower wall and (D) the x -component of the shear force $g_{x,visc}$ acting on the fluid at the upper wall for the wave profile described by (4.45) with $A = 0.03$, $Re = 100$, and $\alpha = 2$. The solid, dashed, and dotted lines correspond to $c = -5$, $c = 0$, and $c = 5$, respectively. Thick and thin lines identify local and mean values, respectively.

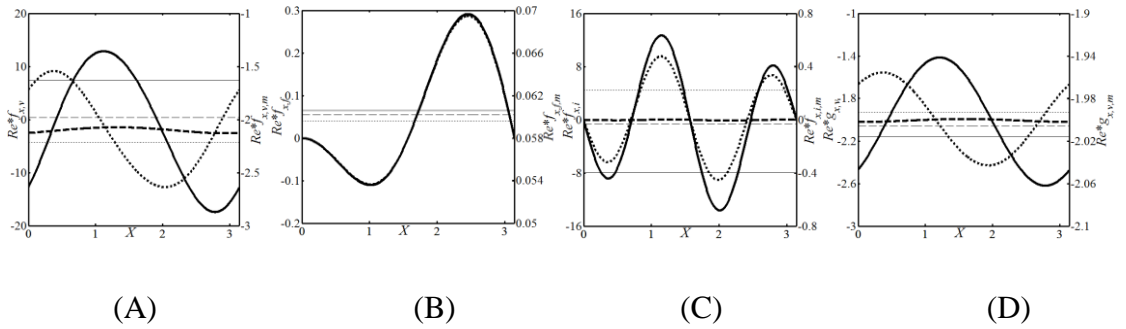


Figure 4.13: Distributions of (A) the x -component of the shear force $f_{x,visc}$ and (B) the x -component of the form force $f_{x,form}$ and (C) the x -component of the interaction force $f_{x,inter}$ acting on the fluid at the lower wall and (D) the x -component of the shear force $g_{x,visc}$ acting on the fluid at the upper wall for the wave profile described by (4.45) with $A = 0.03$, $Re = 200$, and $\alpha = 2$. The solid, dashed, and dotted lines correspond to $c = -5$, $c = 0$, and $c = 5$, respectively. Thick and thin lines identify local and mean values, respectively.

Figure 4.12 displays variations of mean values for $f_{x,visc}$, $f_{x,form}$, $f_{x,inter}$, $g_{x,visc}$, and $f_{x,total}$ as functions of the wave speed c .

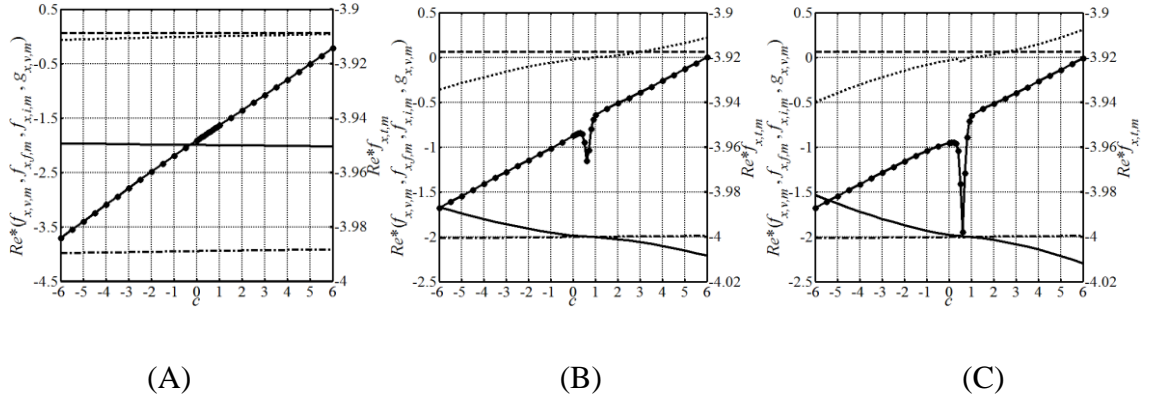


Figure 4.14: Variations of mean values of local forces as functions of the wave speed c . Conditions in Figures 4.14 A–C are the same as conditions in Figures 4.11–4.13, respectively. Solid, dashed, dotted, and dash-dotted lines and line with circles on it correspond to $f_{x,v,m}$, $f_{x,f,m}$, $f_{x,i,m}$, $g_{x,v,m}$, and $f_{x,t,m}(= f_{x,v,m} + f_{x,f,m} + f_{x,i,m} + g_{x,v,m})$, respectively.

It can be seen that $f_{x,visc}$ becomes a more opposing forces as c increases. $f_{x,inter}$ becomes a less opposing force as c increases in the range of $c \in (-5,1)$ and it appears as a reinforcing force as c increases in the range of $c \in (1,5)$. The magnitude of mean value of $f_{x,form}$ reduces as c increases. $g_{x,visc}$ becomes a less opposing force as c increases. The total effect can be shown by the variations of $f_{x,total,mean}$.

4.4.2 Sinusoidal Waves on Both Walls

We shall assume that both walls vibrate in the same manner and determine the effect of the phase shift between the upper and lower waves. The channel geometry is described as

$$Y_U = 1 + A \cos[\alpha(X - ct)], \quad Y_L = -1 + A \cos[\alpha(X - ct) + \phi] \quad (4.46a)$$

where ϕ stands for the phase shift. Galileo transformation leads to the following expression for geometry

$$y_U = 1 + A \cos(\alpha x), \quad y_L = -1 + A \cos(\alpha x + \phi). \quad (4.46b)$$

Figure 4.15 illustrates the variations of the $Re(dp_1/dx)$ as a function of ϕ .

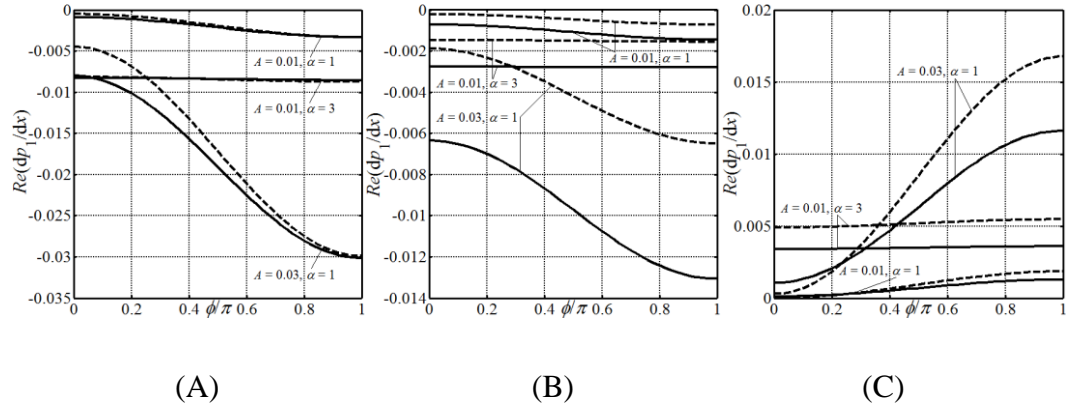


Figure 4.15: Variations of $Re(dp_1/dx)$ as a function of the phase shift ϕ for the wave form defined by (4.46) for selected α and A and: (A) $c = -5$; (B) $c = 0$; (C) $c = 5$. Dashed and solid lines correspond to $Re = 1$ and $Re = 200$, respectively.

It has been verified that when there is no vibration in the channel or when waves propagate in direction opposite to the flow direction, pressure loss increases as the phase shift between the waves on the upper and lower walls increases. This means that, in these cases, wavy channels have the lowest pressure losses and the converging-diverging channels have the highest pressure losses. It has also been demonstrated that when waves propagate in direction similar to the flow direction, drag reduction increases as the phase shift increases. So in this case, converging-diverging channels have better drag-reducing effects comparing to the wavy ones.

Figure 4.16 illustrates the variations of $Re(dp_1/dx)$ as functions of ϕ and c and thus provides a better tool for assessment of the effectiveness of different phase shifts between wave patterns. This Figure illustrates that effects of the phase shifts are more significant for higher magnitudes of phase speed.

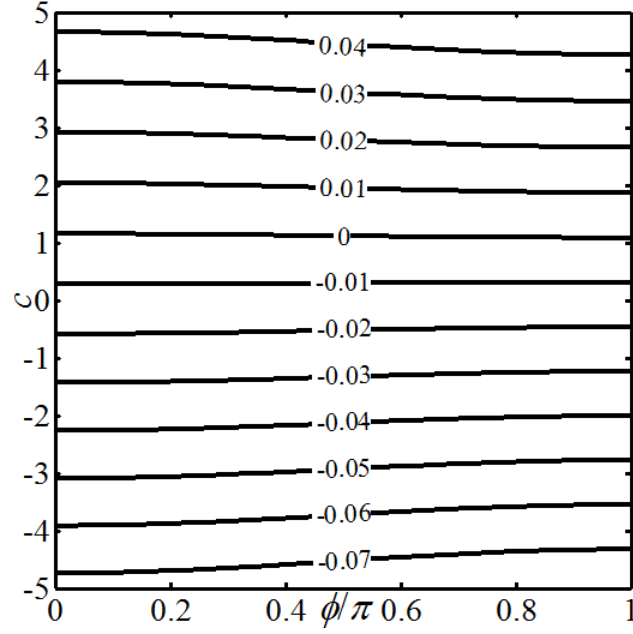


Figure 4.16: Variations of $Re(dp_1/dx)$ as a function of phase shift ϕ and the phase speed c for the wave form defined by (4.46) with $\alpha = 3$, $A = 0.03$ for $Re = 1$.

4.4.3 Different Wave Profiles

We shall now turn our attention to the analysis of the effects of wave profiles. As our interest is in the maximization of the drag reduction, we shall inquire if changing the wave inclination from the upstream-tilted to the downstream-tilted provides any advantage. Waves with triangular shapes shown in Figure 4.17 have been selected for this test. The reader may note that this particular wave profile has to be positioned in such a way so that it does not affect the mean channel opening.

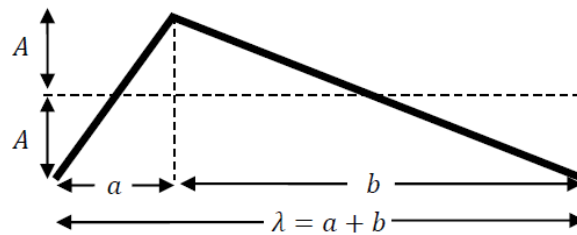


Figure 4.17: Triangular wave profiles used in the study. A , λ and $\alpha = 2\pi/\lambda$ denote the wave amplitude, wavelength and wave number, respectively.

Figure 4.18 illustrates the variations of $Re(dp_1/dx)$ as a function of a/λ , with $a < \lambda/2$ corresponding to the waves tilting upstream, when only one wall vibrates. The symmetric waves (no tilting) produce the smallest pressure losses for the negative phase speeds. Waves with positive c produce the highest drag reduction when tilted in the downstream direction.

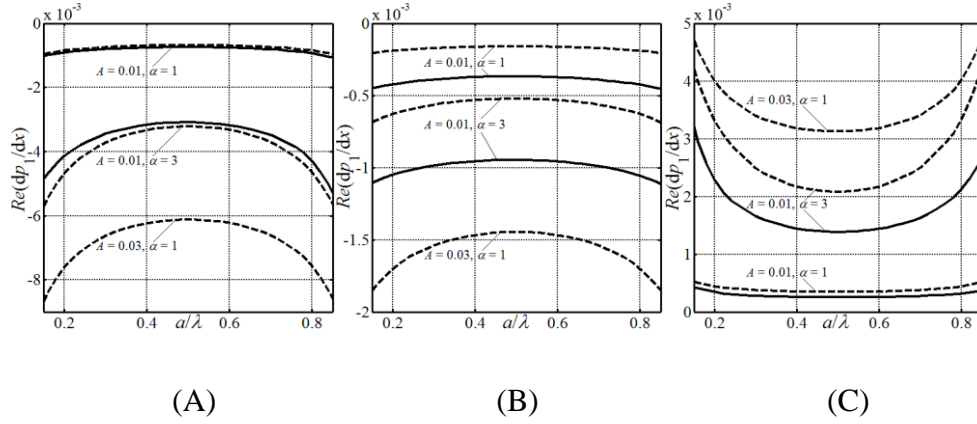


Figure 4.18: Variations of $Re(dp_1/dx)$ as a function of a/λ for waves with triangular profiles (see Figure 4.17) for selected α and A with: (A) $c = -5$; (B) $c = 0$; (C) $c = 5$. Dashed and solid lines correspond to $Re = 1$ and $Re = 200$, respectively. The reader may note that $a < \lambda/2$ corresponds to the waves tilting upstream.

We shall now place triangular waves on both walls and investigate the effect of the phase shift between both waves. The resulting channel geometry is illustrated in Figure 4.19.

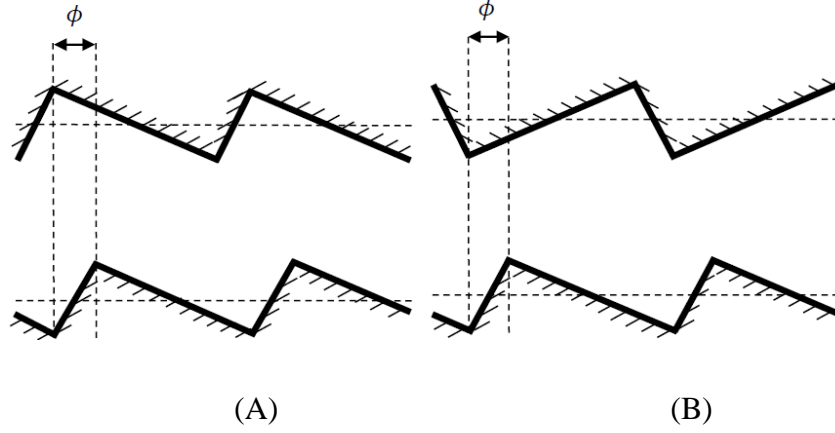


Figure 4.19: Channel with triangular waves at both walls. The parametrization of each wave is the same as in Figure 4.17.

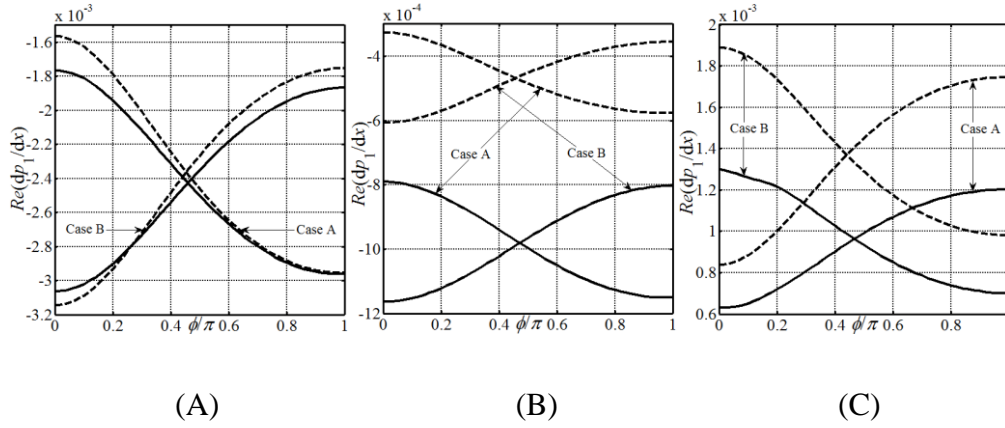


Figure 4.20: Variations of $Re(dp_1/dx)$ as a function of the phase shift ϕ for wave forms defined in Figure 4.19 for $\alpha = 1$, $A = 0.01$, $a/\lambda = 0.1$ and: (A) $c = -5$; (B) $c = 0$; (C) $c = 5$. Cases A and B correspond to configurations A and B in Figure 4.19. Dashed and solid lines correspond to $Re = 1$ and $Re = 200$, respectively.

Data presented in Figure 4.20 demonstrate that the drag reduction is maximized when the waves propagate in the downstream direction and their relative position corresponds to $\phi = \pi$ (Case A) and $\phi = 0$ (Case B) i.e. they produce a bulge which propagates in the downstream direction; such channel assumes the diverging-converging form in the reference frame moving with the wave. The losses can be minimized for waves propagating in the upstream direction when the relative position of both waves

corresponds to $\phi = 0$ (Case A) and $\phi = \pi$ (Case B) i.e. the channel assumes a wavy form in the moving reference frame.

Section 5

5 Conclusions

An efficient algorithm for the analysis of flows in channels with vibrating walls has been developed. The algorithm is able to simulate waves with arbitrary profiles propagating along or against the flow direction. The spatial discretization is based on the Fourier expansions in the flow direction and on the Chebyshev expansions in the transverse direction. Use of the Galileo transformation eliminates the need for any time discretization. The domain irregularity associated with the waves is accounted for by using the immersed boundary conditions concept. The field equations are discretized using a regular, rectangular computational domain while the vibrating channel is immersed inside this domain. A Galerkin procedure is used to develop algebraic equations corresponding to the field equation. The tau procedure is used to provide space for the inclusion of the flow boundary conditions. The forms of these conditions suitable for the inclusion in the algorithm have been constructed using Fourier expansions based on the shape of the vibrating wall. This has led to construction of internal constraints which are then used to close the system of equations. Use of an iterative solution method based on values of nonlinear terms from the previous iteration resulted in a first order fixed-point method. A special linear solver, which takes advantage of the structure of the coefficient matrix, has been used. It has been demonstrated that the algorithm does deliver the spectral accuracy. The absolute error increases for more demanding wave shapes due to the reduction in the convergence rates of the Fourier expansions used for the construction of the boundary relations. It has been demonstrated that accuracy can be increased by using additional boundary relations in excess to that required for the closure of the system of equations, leading to the over-determined formulation. The resulting system is solved in such a way that the part associated with the field equation is solved exactly while the part associated with the boundary relations solved in the least square sense. The best results are obtained when the number of boundary relations used in the

computation is approximately 50% larger than the number of Fourier modes used to discretize the field equation.

Analysis of drag generation in conduits with vibrating walls has been carried out analytically using both long wavelength and small amplitude approximations. These solutions have been validated by comparing analytical results with numerical solution of the complete field equations. Detailed analyses of different cases, i.e. waves propagation along one wall and both walls have been carried out. Different wave profiles have been considered in order to find forms of waves which minimize pressure losses in vibrating channels. The results show dependence of the pressure losses on the phase speed of the waves, with the waves propagating in the downstream direction reducing the pressure gradient required to maintain a fixed flow rate. A drag increase is observed when the waves propagate with a phase speed similar to the flow velocity. Analytical solution demonstrates that the drag changes result from the nonlinear interactions and vary proportionally to A^2 for small enough A , where A stands for the wave amplitude.

There are several conditions limiting applicability of the results reported in this thesis. Single-phase flow considered in this thesis is always laminar as Reynolds number is kept sufficiently small. In addition, no flow separation has been considered. Only waves with sinusoidal and simple Fourier-transformable geometries have been studied. The wave amplitude, the wave number and the wave phase speed can assume values below certain critical thresholds as otherwise numerical error begins to increase rapidly.

References

- [1] J.M. Floryan, H. Rasmussen, Numerical analysis of viscous flows with free surfaces, *Appl. Mech. Rev.* 42 (1989) 323–341.
- [2] R. Scardovelli, S. Zaleski, Direct numerical simulation of free surface and interfacial flow, *Ann. Rev. Fluid Mech.* 31 (1999) 567–603.
- [3] J.M. Hyman, Numerical methods for tracking of interfaces, *Physica* 12D (1984) 396–407.
- [4] J.Glimm, J.W. Grove, X.L. Li, K.M. Shyue, Y. Zeng, Q. Zhang, Three-dimensional front tracking, *SIAM J. Sci. Computing*, 19 (1998) 703–727.
- [5] C.W. Hirt, B.D. Nichols, Volume of fluid (VOF) method for the dynamics of free boundaries, *J. Comp. Phys.* 39 (1981) 201–225.
- [6] F.H. Harlow, J.E. Welch, Numerical study of large amplitude free surface motions, *Phys. Fluids* 9 (1996) 842–851.
- [7] J.A. Sethian, *Level set methods and fast marching methods: evolving interfaces in computational geometry, Fluid Mechanics, Computer Vision and Materials Science*, Cambridge University Press, 1999.
- [8] J.A. Sethian, P. Smereka, Level set methods for fluid interfaces, *Ann. Rev. Fluid Mech.* 35 (2003) 341–372.
- [9] I. Inculet, J.M. Floryan, R. Haywood, Dynamics of water droplets break-up in electric fields, *IEEE Transactions on Industry Applications* 28 (1992) 1203–1209.
- [10] J.M. Floryan, Conformal-mapping-based coordinate generation for flows in periodic configurations, *J. Comp. Phys.* 62 (1986) 221–247.
- [11] J.M. Floryan, C. Zemach, Schwarz-Christoffel transformations - a general approach, *J. Comp. Phys.* 72 (1987) 347–371.
- [12] J.M. Floryan, C. Zemach, Schwarz-Christoffel methods for conformal mappings of regions with a periodic boundary, *J. Comp. Applied Math* 46 (1993) 77–102.
- [13] M. Hamed, J.M. Floryan, Numerical simulation of unsteady nonisothermal capillary interfaces, *J. Comp. Phys.* 145 (1998) 110–140.

- [14] A. Cabal, J. Szumbariski, J.M. Floryan, Numerical simulation of flows over corrugated walls, *Comp. & Fluids* 30 (2001) 753–776.
- [15] S.Z. Husain, J.M. Floryan, Spectrally-accurate algorithm for moving boundary problems for the Navier-Stokes equations, *J. Comp. Phys.* 229 (2010) 2287–2313.
- [16] A. Mohammadi, J.M. Floryan, Pressure losses in grooved channels, *J. Fluid Mech.* 725 (2013) 23–54.
- [17] A. Mohammadi, J.M. Floryan, Groove optimization for drag reduction, *Phys. Fluids* 25 (2013) 113601.
- [18] A. Mohammadi, J.M. Floryan, Effects of longitudinal grooves on the Couette–Poiseuille flow, *Theor. Comput. Fluid Dyn.* 28 (2014) 549–572.
- [19] A. Mohammadi, J.M. Floryan, Numerical analysis of laminar-drag-reducing grooves, *ASME J. Fluids Eng.* 137 (2014) 041201.
- [20] H.V. Moradi, J.M. Floryan, Flows in annuli with longitudinal grooves, *J. Fluid Mech.* 716 (2013) 280–315.
- [21] C.S. Peskin, The fluid dynamics of heart valves: experimental, theoretical and computational methods, *Ann. Rev. Fluid Mech.* 14 (1981) 235–259.
- [22] C.S. Peskin, The immersed boundary method, *Acta Numerica* 11 (2002) 479–517.
- [23] R. Mittal, G. Iaccarino, Immersed boundary methods, *Annu. Rev. Fluid Mech.* 37 (2005) 239–261.
- [24] J. Deng, X.M. Shao, A.L. Ren, A new modification of the immersed-boundary method for simulating flows with complex moving boundaries, *Int. J. of Num. Meth. Fluids*, 52 (2006) 1195–1213.
- [25] K. Taira, T. Colonius, The immersed boundary method: a projection approach, *J. Comp. Phys.* 225 (2007) 2118–2137.
- [26] J. Kim, D. Kim, H. Choi, An immersed boundary finite-volume method for simulation of flows in complex geometries, *J. Comp. Phys.* 171 (2001) 132–150.
- [27] J. Szumbariski, J.M. Floryan, A direct spectral method for determination of flows over corrugated boundaries, *J. Comp. Phys.* 153 (1999) 378–402.
- [28] S.Z. Husain, J.M. Floryan, Immersed boundary conditions method for unsteady flow problems described by the Laplace operator, *Int. J. Numer. Meth. Fluids* 56 (2007) 1765–1786.

- [29] S.Z. Husain, J.M. Floryan, Implicit spectrally-accurate method for moving boundary problems using immersed boundary conditions concept, *J. Comp. Phys.* 227 (2008) 4459–4477.
- [30] S.Z. Husain, J.M. Floryan, Gridless spectral algorithm for Stokes flow with moving boundaries, *Comput. Methods Appl. Mech. Engrg.* 198 (2008) 245–259.
- [31] S.Z. Husain, J.M. Floryan, Spectrally-accurate algorithm for moving boundary problems for the Navier-Stokes equations, *J. Comp. Phys.* 229 (2010) 2287–2313.
- [32] A. Mohammadi, J.M. Floryan, P.N. Kaloni, Spectrally accurate method for analysis of stationary flows of second-order fluids in rough micro-channels, *Int. J. Numer. Meth. Fluids* 66 (2010) 509–536.
- [33] M.F. Bakhsheshi, J.M. Floryan, P.N. Kaloni, Spectral method for analyzing motions of Ellis fluid over corrugated boundaries, *J. Fluids Eng.* 133 (2011) 021401.
- [34] D.C. Del Rey Fernandez, S.Z. Husain, J.M. Floryan, Immersed boundary conditions method for heat conduction problems in slots with time-dependent geometry, *Int. J. Numer. Meth. Fluids* 67 (2010) 478–500.
- [35] A. Mohammadi, J.M. Floryan, Spectral algorithm for the analysis of flows in grooved channels, *Int. J. Numer. Meth. Fluids* 69 (2012) 606–638.
- [36] H.V. Moradi, J.M. Floryan, Algorithm for analysis of flows in ribbed annuli, *Int. J. Numer. Meth. Fluids* 68 (2012) 805–838.
- [37] S.Z. Husain, J.M. Floryan, J. Szumbariski, Over-determined formulation of the immersed boundary conditions method, *Comput. Methods Appl. Mech. Engrg.* 199 (2009) 94–112.
- [38] S.Z. Husain, J.M. Floryan, Effective solvers for the immersed boundaries method. *Computers & Fluids* 84 (2013) 127–140.
- [39] S.Z. Husain, J.M. Floryan, Efficient over-determined implementation of the immersed boundary conditions method, *Computers & Fluids* 105 (2014) 194–203.
- [40] J.M. Floryan, Centrifugal instability of Couette flow over a wavy wall, *Phys. Fluids* 14 (2002) 312–322.
- [41] J.M. Floryan, Vortex instability in a diverging-converging channel, *J. Fluid Mech.* 482 (2003) 17–50.

- [42] J.M. Floryan, Two-dimensional instability of flow in a rough channel, *Phys. Fluids*. 17 (2005) 044101.
- [43] J.M. Floryan, Three-dimensional instabilities of laminar flow in a rough channel and the concept of hydraulically smooth wall, *Eur. J. Mech. B/Fluids* 26 (2007) 305–329.
- [44] J.M. Floryan, C. Floryan, Traveling wave instability in a diverging-converging channel, *Fluid Dyn. Res.* 42 (2010) 025509.
- [45] J.M. Floryan, M. Asai, On the transition between distributed and isolated surface roughness and its effect on the stability of channel flow, *Phys. Fluids* 23 (2011) 104101.
- [46] H.V. Moradi, J.M. Floryan, Stability of flow in a channel with longitudinal grooves, *J. Fluid Mech.* 757 (2014) 613–648.
- [47] J.J. Riley, M. Gad-el-Hak, R.W. Metcalfe, Compliant coatings, *Ann. Rev. Fluid Mech.* 20 (1988) 393–420.
- [48] F. Laadhari, L. Skandaji, R. Morel, Turbulence reduction in a boundary layer by a local spanwise oscillating surface, *Phys. Fluids* 6 (1994) 3218–3220.
- [49] H. Choi, P. Moin, J. Kim, Active turbulence control for drag reduction in wall-bounded flows, *J. Fluid Mech.* 262 (1994) 75–110.
- [50] Y. Mito, N. Kasagi, DNS study of turbulence modification with streamwise-uniform sinusoidal wall-oscillation, *Int. J. Heat Fluid Flow* 19 (1998) 470–481.
- [51] T. Endo, N. Kasagi, Y. Suzuki, Feedback control of wall turbulence with wall deformation, *Int. J. Heat Fluid Flow* 21 (2000) 568–575.
- [52] S. Kang, H. Choi, Active wall motions for skin-friction drag reduction, *Phys. Fluids* 12 (2000) 3301–3304.
- [53] T. Endo, N. Kasagi, Active control of wall turbulence with wall deformation, *JSME Int. J. Ser. B Fluids Thermal Eng.* 44 (2001) 195–203.
- [54] C. Lee, J. Kim, Control of the viscous sublayer for drag reduction, *Phys. Fluids* 14 (2002) 2523–2529.
- [55] C. Kim, W.P. Jeon, J. Park, M. Choi, Effects of a localized time-periodic wall motion on a turbulent boundary layer, *Phys. Fluids* 15 (2003) 265–268.

- [56] L. Meijing, J.G. Brasseur, Non-steady peristaltic transport in finite-length tubes, *J. Fluid Mech.* 248 (1993) 129–151.
- [57] Y. Aboelkassem, A.E. Staples, Flow transport in a microchannel induced by moving wall contractions: a novel micropumping mechanism, *Acta Mech.* 223 (2012) 463–480.
- [58] T. Hayat, N. Ali, S. Asghar, An analysis of peristaltic transport for flow of a Jeffrey fluid, *Acta Mech.* 193 (2007) 101–112.
- [59] E.F. El-Shehawy, N.T. El-Dabe, I.M. El-Desoky, Slip effects on the peristaltic flow of a non-Newtonian Maxwellian fluid, *Acta Mech.* 186 (2006) 141–159.
- [60] N. Ali, M. Sajid, Z. Abbas, T. Javed, Non-Newtonian fluid flow induced by peristaltic waves in a curved channel, *Eur. J. Mech B-Fluids* 29 (2010) 387–394.
- [61] A. Ramachandra Rao, M. Mishra, Nonlinear and curvature effects on peristaltic flow of a viscous fluid in an asymmetric channel, *Acta Mech.* 168 (2004) 35–39.
- [62] J. Høpfner, K. Fukagata, Pumping or drag reduction?, *J. Fluid Mech.* 635 (2009) 171–187.
- [63] J.W. Gibbs, Fourier's Series, *Nature* 59 (1898) 200.
- [64] J.W. Gibbs, Fourier's Series, *Nature* 59 (1899) 606.
- [65] H. Wilbraham, On a certain periodic function, *The Cambridge and Dublin Mathematical Journal* 3 (1848) 198–201.
- [66] C. Canuto, M.Y. Hussaini, A. Quarteroni, T.A. Zang, *Spectral Methods: Fundamentals in Single Domains*, Springer-Verlag, Berlin Heidelberg, 2006.
- [67] J.C. Manson, D.C. Handscomb, *Chebyshev Polynomials*, CRC Press, Boca Raton, Florida, 2003.
- [68] D.J. Jeffrey, A.D. Rich, The evaluation of trigonometric integrals avoiding spurious discontinuities, *ACM Trans. Math. Software* 20(1) (1994) 124–135.
- [69] S. Zandi, A. Mohammadi & J.M. Floryan, Spectrally-Accurate Algorithm for the Analysis of Flows in Two-Dimensional Vibrating Channels, *J. Comp. Phys.* 301 (2015) 425–455.

Appendices

Appendix A

Evaluation of the inner products

- (I) Evaluation of the inner product of the Chebyshev polynomial of order j and the first derivative of the Chebyshev polynomial of order k , e.g. $\langle T_j, DT_k \rangle$.

The first derivative of the Chebyshev polynomial of order k can be expressed in terms of the remaining Chebyshev polynomials in the form of

$$DT_k = 2k \sum_{x=0}^{x=k-1} \frac{1}{C_x} T_x, \quad k - x = \text{odd}, \quad k \geq x + 1 \quad (\text{A.1})$$

where C_x is defined as

$$C_x = \begin{cases} 2, & x = 0, \\ 1, & x \geq 1. \end{cases} \quad (\text{A.2})$$

Inner product of (A.1) with T_j gives

$$\langle T_j, DT_k \rangle = 2k \sum_{x=0}^{x=k-1} \frac{1}{C_x} \langle T_j, T_x \rangle, \quad k - x = \text{odd}, \quad k \geq x + 1. \quad (\text{A.3})$$

Insertion of (3.25) into (A.3) results in a final form of the inner product, i.e.

$$\langle T_j, DT_k \rangle = k\pi, \quad k - j = \text{odd}, \quad k \geq j + 1. \quad (\text{A.4})$$

- (II) Evaluation of the inner product of the Chebyshev polynomial of order j and the second derivative of the Chebyshev polynomial of order k , e.g. $\langle T_j, D^2T_k \rangle$.

Second derivative of the Chebyshev polynomial of order k can be expressed in terms of the remaining Chebyshev polynomials in the form of

$$D^2 T_k = \sum_{x=0}^{x=k-2} \frac{1}{c_x} k(k^2 - x^2) T_x, \quad k - x = \text{even}, \quad k \geq x + 2. \quad (\text{A.5})$$

Its inner product with the Chebyshev polynomial T_j can be expressed as

$$\langle T_j, D^2 T_k \rangle = \sum_{x=0}^{x=k-2} \frac{1}{c_x} k(k^2 - x^2) \langle T_j, T_x \rangle, \quad k - x = \text{even}, \quad k \geq x + 2. \quad (\text{A.6})$$

The simplified form of (A.6) can be obtained with the help of Eq. (3.25) which results in

$$\langle T_j, D^2 T_k \rangle = k(k^2 - j^2) \frac{\pi}{2}, \quad k - j = \text{even}, \quad k \geq j + 2. \quad (\text{A.7})$$

(III) Evaluation of the inner product of the Chebyshev polynomial of order j and the third derivative of the Chebyshev polynomial of order k , e.g. $\langle T_j, D^3 T_k \rangle$.

Taking derivative of (A.5) with respect to \hat{y} leads to a relation for the third derivative of Chebyshev polynomial T_k in the form

$$D^3 T_k = \sum_{x=0}^{x=k-2} \frac{1}{c_x} k(k^2 - x^2) D T_x, \quad k - x = \text{even}, \quad k \geq x + 2. \quad (\text{A.8})$$

Substitution of (A.1) into the above equation, leads to the following relation for the third derivative of Chebyshev polynomial T_k

$$D^3 T_k = \sum_{x=0}^{x=k-2} \frac{1}{c_x} k(k^2 - x^2) \left[2x \sum_{z=0}^{z=x-1} \frac{1}{c_z} T_z \right], \quad \begin{cases} k - x = \text{even}, & k \geq x + 2, \\ x - z = \text{odd}, & x \geq z + 1. \end{cases} \quad (\text{A.9})$$

Taking inner product of (A.9) with T_j and using (3.25) result in a relation for inner product of a Chebyshev polynomial of j th order and its third derivative of k th order, i.e.

$$\langle T_j, D^3 T_k \rangle = \sum_{x=0}^{x=k-2} \frac{1}{c_x} k(k^2 - x^2) \pi x, \quad \begin{cases} k - x = \text{even}, & k \geq x + 2, \\ x - j = \text{odd}, & x \geq j + 1. \end{cases} \quad (\text{A.10})$$

(IV) Evaluation of the inner product of the Chebyshev polynomial of order j and the fourth derivative of the Chebyshev polynomial of order k , e.g. $\langle T_j, D^4 T_k \rangle$.

Evaluation of the forth derivative of the Chebyshev polynomial of order k begins with taking the second derivative of (A.5) with respect to \hat{y} , i.e.

$$D^4 T_k = \sum_{x=0}^{x=k-2} \frac{1}{c_x} k(k^2 - x^2) D^2 T_x, \quad k - x = \text{even}, \quad k \geq x + 2. \quad (\text{A.11})$$

Replacing $D^2 T_x$ with (A.5) gives

$$D^4 T_k = \sum_{x=0}^{x=k-2} \frac{1}{c_x} k(k^2 - x^2) \left[\sum_{z=0}^{z=x-2} \frac{1}{c_z} x(x^2 - z^2) T_z \right],$$

$$\begin{cases} k - x = \text{even}, & k \geq x + 2, \\ x - z = \text{even}, & x \geq z + 2. \end{cases} \quad (\text{A.12})$$

Taking the inner product of (A.12) with the Chebyshev polynomial T_j leads to

$$\langle T_j, D^4 T_k \rangle = \sum_{x=0}^{x=k-2} \frac{1}{c_x} k(k^2 - x^2) \left[x(x^2 - j^2) \frac{\pi}{2} \right],$$

$$\begin{cases} k - x = \text{even}, & k \geq x + 2 \geq j + 4, \\ x - j = \text{even}, & x \geq j + 2. \end{cases} \quad (\text{A.13})$$

(V) Evaluation of the inner product of the Chebyshev polynomial of order j with $u_0 T_k$,
i.e. $\langle T_j, u_0 T_k \rangle$.

Evaluation begins by expressing u_0 in terms of the Chebyshev polynomials, i.e.

$$u_0(\hat{y}) = \sum_{m=0}^{m=M} U_m T_m(\hat{y}) \quad (\text{A.14})$$

where U_m 's are the coefficients of the expansion and M denotes the length of the expansion. The reference velocity u_0 has the form (see Eq. (3.28))

$$u_0(\hat{y}) = -a^2 \hat{y}^2 - 2ab\hat{y} + 1 - b^2 \quad (\text{A.15})$$

where

$$a = \Gamma^{-1}, \quad b = -\Gamma^{-1} + 1 + y_t. \quad (\text{A.16})$$

This leads to the expansion coefficients of the form

$$U_0 = 1 - \frac{a^2}{2} - b^2, \quad U_1 = -2ab, \quad U_2 = -\frac{a^2}{2}. \quad (\text{A.17})$$

The inner product $\langle T_j, u_0 T_k \rangle$ takes the form

$$\langle T_j, u_0 T_k \rangle = \int_{-1}^1 \sum_{m=0}^{m=2} T_j U_m T_m T_k \omega dy = \sum_{m=0}^{m=2} U_m \left(\int_{-1}^1 T_j T_m T_k \omega dy \right). \quad (\text{A.18})$$

Use of the following property of the Chebyshev polynomials

$$T_j T_m = \frac{1}{2} (T_{j+m} + T_{|j-m|}) \quad (\text{A.19})$$

in (A.18) leads to

$$\begin{aligned} \langle T_j, u_0 T_k \rangle &= \frac{1}{2} \sum_{m=0}^{m=2} U_m \left[\int_{-1}^1 T_{j+m} T_k \omega dy + \int_{-1}^1 T_{|j-m|} T_k \omega dy \right] = \\ &= \frac{1}{2} \sum_{m=0}^{m=2} U_m [\langle T_{j+m}, T_k \rangle + \langle T_{|j-m|}, T_k \rangle]. \end{aligned} \quad (\text{A.20})$$

(VI) Other inner products

Evaluation of the inner-product $\langle T_j, (u_0 - c) T_k \rangle$ takes advantage of the following relation

$$\langle T_j, (u_0 - c) T_k \rangle = \langle T_j, u_0 T_k \rangle - c \langle T_j, T_k \rangle. \quad (\text{A.21})$$

Evaluation of the inner products on the right hand side of (A.21) has already been explained.

Evaluation of the inner products $\langle T_j, u_0 D^2 T_k \rangle$ and $\langle T_j, (u_0 - c) D^2 T_k \rangle$ takes advantage of the following relations

$$\langle T_j, u_0 D^2 T_k \rangle = \frac{1}{2} \sum_{m=0}^{m=2} U_m [\langle T_{j+m}, D^2 T_k \rangle + \langle T_{|j-m|}, D^2 T_k \rangle], \quad (\text{A.22})$$

$$\langle T_j, (u_0 - c) D^2 T_k \rangle = \langle T_j, u_0 D^2 T_k \rangle - c \langle T_j, D^2 T_k \rangle. \quad (\text{A.23})$$

Evaluation of the inner product $\langle T_j, D^2 u_0 T_k \rangle$ begins with evaluation of $D^2 u_0$, i.e.

$$D^2 u_0(y) = -2a^2. \quad (\text{A.24})$$

The inner product $\langle T_j, D^2 u_0 T_k \rangle$ reduces to the following form

$$\langle T_j, D^2 u_0 T_k \rangle = -2a^2 \langle T_j, T_k \rangle \quad (\text{A.25})$$

where evaluation of the product on the right hand side has already been explained.

Appendix B

Definitions of functions used in Subsection 4.2

$$F_1 = \eta_{xx} G_3^{-1} = [-\alpha^2 G_1 A \cos(\xi) + 2\alpha^2 A^2 \sin^2(\xi)](\eta - 1) G_2^{-1} = \frac{1}{4} \alpha^2 [-G_1 A \cos(\xi) + 2A^2 \sin^2(\xi)](\eta - 1) + O(\alpha^4), \quad (\text{B.1a})$$

$$F_2 = \text{Re } \eta_x G_3^{-1} = -\alpha \text{Re } A \sin(\xi) G_1 (\eta - 1) G_2^{-1} = -\frac{1}{4} \alpha \text{Re } G_1 A \sin(\xi) (\eta - 1) + O(\alpha^3), \quad (\text{B.1b})$$

$$F_3 = \text{Re } \eta_y G_3^{-1} = 2 \text{Re } G_1 G_2^{-1} = \frac{1}{2} \text{Re } G_1 - \frac{1}{8} \text{Re } G_1 (G_2 - 4) + O(\alpha^4), \quad (\text{B.1c})$$

$$F_4 = 2\alpha \eta_x G_3^{-1} = -2\alpha^2 A \sin(\xi) G_1 (\eta - 1) G_2^{-1} = -\frac{1}{2} \alpha^2 G_1 A \sin(\xi) (\eta - 1) + O(\alpha^4), \quad (\text{B.1d})$$

$$F_5 = \alpha^2 G_3^{-1} = \alpha^2 G_1^2 G_2^{-1} = \frac{1}{4} \alpha^2 G_1^2 + O(\alpha^4), \quad (\text{B.1e})$$

$$F_6 = \alpha \text{Re } G_3^{-1} = \alpha \text{Re } G_1^2 G_2^{-1} = \frac{1}{4} \alpha \text{Re } G_1^2 + O(\alpha^3), \quad (\text{B.1f})$$

$$F_7 = \eta_x = -\alpha A (\eta - 1) \sin(\xi) G_1^{-1}, \quad F_8 = \eta_y = 2 G_1^{-1}, \quad (\text{B.1g-h})$$

$$G_1 = 2 - A \cos(\xi), \quad G_2 = 4 + \alpha^2 A^2 \sin^2(\xi) (\eta - 1)^2, \quad G_3 = \eta_x^2 + \eta_y^2, \quad (\text{B.1i-k})$$

$$H_1 = -\frac{1}{80} \eta^6 + \frac{3}{32} \eta^4 - \frac{1}{8} \eta^3 - \frac{27}{280} \eta^2 + \frac{1}{8} \eta + \frac{17}{1120},$$

$$H_2 = -\frac{1}{80} \eta^6 + \frac{1}{4} \eta^3 + \frac{9}{560} \eta^2 - \frac{1}{4} \eta - \frac{1}{280}, \quad (\text{B.2a-b})$$

$$H_3 = \frac{1}{12} \eta^4 - \frac{1}{6} \eta^3 - \frac{1}{10} \eta^2 + \frac{1}{6} \eta + \frac{1}{60}, \quad H_4 = -\frac{1}{12} \eta^4 + \frac{1}{10} \eta^2 - \frac{1}{60}, \quad (\text{B.2c-d})$$

$$H_5 = \frac{1}{24} \eta^6 - \frac{1}{4} \eta^4 + \frac{1}{6} \eta^3 + \frac{69}{280} \eta^2 - \frac{1}{6} \eta - \frac{4}{105},$$

$$H_6 = \frac{1}{60}\eta^6 - \frac{1}{3}\eta^3 - \frac{3}{140}\eta^2 + \frac{1}{3}\eta + \frac{1}{210}, \quad (\text{B.2e-f})$$

$$H_7 = -\frac{1}{8}\eta^4 + \frac{1}{6}\eta^3 + \frac{3}{20}\eta^2 - \frac{1}{6}\eta - \frac{1}{40}, \quad H_8 = -\frac{1}{30}\eta^6 + \frac{1}{6}\eta^4 - \frac{11}{70}\eta^2 + \frac{1}{42}, \quad (\text{B.2g-h})$$

$$H_9 = -\frac{1}{4}\eta^3 + \frac{3}{4}\eta - \frac{1}{2}, \quad H_{10} = \frac{1}{4}\eta^3 - \frac{3}{8}\eta^2 + \frac{1}{8}, \quad H_{11} = \frac{1}{2}\eta^3 - \frac{1}{2}\eta^2 - \frac{1}{2}\eta + \frac{1}{2} \quad (\text{B.2i-k})$$

Appendix C

Definitions of functions used in Subsection 4.3

$$I_1 = \eta_{xx} L_3^{-1} = [-\alpha^2 L_1 A \cos(\alpha\xi) + 2\alpha^2 A^2 \sin^2(\alpha\xi)](\eta - 1) L_2^{-1} =$$

$$\frac{1}{4} \alpha^2 [-2A \cos(\alpha\xi) + A^2 (\cos^2(\alpha\xi) + 2\sin^2(\alpha\xi))](\eta - 1) + O(A^3), \quad (\text{C.1a})$$

$$I_2 = \text{Re } \eta_x L_3^{-1} = -\alpha \text{Re } A \sin(\alpha\xi) L_1 (\eta - 1) L_2^{-1} =$$

$$-\frac{1}{4} (2A - A^2 \cos(\alpha\xi)) \alpha \text{Re } \sin(\alpha\xi) (\eta - 1) + O(A^3), \quad (\text{C.1b})$$

$$I_3 = \text{Re } \eta_y L_3^{-1} = 2 \text{Re } L_1 L_2^{-1} =$$

$$\frac{1}{4} \text{Re} [4 - 2A \cos(\alpha\xi) - A^2 \alpha^2 \sin^2(\alpha\xi) (\eta - 1)^2] + O(A^3), \quad (\text{C.1c})$$

$$I_4 = 2\eta_x L_3^{-1} = -2\alpha A \sin(\alpha\xi) L_1 (\eta - 1) L_2^{-1} =$$

$$-\frac{1}{2} (2A - A^2 \cos(\alpha\xi)) \alpha \sin(\alpha\xi) (\eta - 1) + O(A^3), \quad (\text{C.1d})$$

$$I_5 = L_3^{-1} = L_1^2 L_2^{-1} =$$

$$1 - A \cos(\alpha\xi) + \frac{1}{4} A^2 [\cos^2(\alpha\xi) - \alpha^2 \sin^2(\alpha\xi) (\eta - 1)^2] + O(A^3), \quad (\text{C.1e})$$

$$I_6 = \text{Re } L_3^{-1} = \text{Re } L_1^2 L_2^{-1} =$$

$$\frac{1}{4} \text{Re} [4 - 4A \cos(\alpha\xi) + A^2 (\cos^2(\alpha\xi) - \alpha^2 \sin^2(\alpha\xi) (\eta - 1)^2)] + O(A^3), \quad (\text{C.1f})$$

$$I_7 = \eta_x = -\alpha A (\eta - 1) \sin(\alpha\xi) L_1^{-1} =$$

$$-\frac{1}{4} (2A + A^2 \cos(\alpha\xi)) \alpha \sin(\alpha\xi) (\eta - 1) + O(A^3), \quad (\text{C.1g})$$

$$I_8 = \eta_y = 2L_1^{-1} = 1 + \frac{1}{2}A \cos(\alpha\xi) - \frac{1}{4}A^2 \cos^2(\alpha\xi) + O(A^3), \quad (\text{C.1h})$$

$$L_1 = 2 - A \cos(\alpha\xi), \quad L_2 = 4 + \alpha^2 A^2 \sin^2(\alpha\xi) (\eta - 1)^2, \quad L_3 = \eta_x^2 + \eta_y^2, \quad (\text{C.1i-k})$$

$$\begin{aligned} g_1 = & -\frac{1}{4}\alpha^2(\eta - 1)D\left(\tilde{u}_1^{(-1)} + \tilde{u}_1^{(1)}\right) - \frac{1}{2}\alpha^2\left(\tilde{u}_1^{(-1)} + \tilde{u}_1^{(1)}\right) + \\ & \frac{1}{2}i\alpha \operatorname{Re}(-2\eta^2 + \eta + 1 - c)\left(\tilde{u}_1^{(-1)} - \tilde{u}_1^{(1)}\right) + \\ & \frac{1}{4}i\alpha \operatorname{Re}[-\eta^3 + \eta^2 + c(1 - \eta) + \eta - 1]D\left(\tilde{u}_1^{(-1)} - \tilde{u}_1^{(1)}\right) + \\ & \frac{1}{2}\operatorname{Re}\eta\left(\tilde{v}_1^{(-1)} + \tilde{v}_1^{(1)}\right) + \operatorname{Re}\left(\tilde{v}_1^{(1)}D\tilde{u}_1^{(-1)} + \tilde{v}_1^{(-1)}D\tilde{u}_1^{(1)}\right) \\ & + \frac{1}{2}i\alpha \operatorname{Re}\left(\tilde{p}_1^{(-1)} - \tilde{p}_1^{(1)}\right) + \frac{1}{4}i\alpha \operatorname{Re}(\eta - 1)D\left(\tilde{p}_1^{(-1)} - \tilde{p}_1^{(1)}\right) - \\ & \frac{1}{4}[1 + \alpha^2(-4\eta^2 + 5\eta - 1)], \end{aligned} \quad (\text{C.2a})$$

$$\begin{aligned} g_2 = & -\frac{1}{4}\alpha^2(\eta - 1)D\left(\tilde{v}_1^{(-1)} + \tilde{v}_1^{(1)}\right) - \\ & \frac{1}{4}i\alpha \operatorname{Re}[\eta^3 - \eta^2 + c(\eta - 1) - \eta + 1]D\left(\tilde{v}_1^{(-1)} - \tilde{v}_1^{(1)}\right) + \\ & \operatorname{Re}D\left(\tilde{v}_1^{(-1)}\tilde{v}_1^{(1)}\right) - \frac{1}{2}\alpha^2\left(\tilde{v}_1^{(-1)} + \tilde{v}_1^{(1)}\right) + i\alpha \operatorname{Re}\left(u_1^{(-1)}v_1^{(1)} - u_1^{(1)}v_1^{(-1)}\right) + \\ & \frac{1}{2}i\alpha \operatorname{Re}(1 - c - \eta^2)\left(\tilde{v}_1^{(-1)} - \tilde{v}_1^{(1)}\right) - \frac{1}{4}\operatorname{Re}D\left(\tilde{p}_1^{(-1)} + \tilde{p}_1^{(1)}\right), \end{aligned} \quad (\text{C.2b})$$

$$g_3 = -\frac{1}{4}i\alpha(\eta - 1)D\left(\tilde{u}_1^{(-1)} - \tilde{u}_1^{(1)}\right) - \frac{1}{4}D\left(\tilde{v}_1^{(-1)} + \tilde{v}_1^{(1)}\right) \quad (\text{C.2c})$$

Appendix D

Copyright release

This is a License Agreement between Sahab Zandi ("You") and Elsevier ("Elsevier"). The license consists of your order details, the terms and conditions provided by Elsevier, and the payment terms and conditions.

License Number:	3718420651152
License date:	Sep 24, 2015
Licensed content publisher:	Elsevier
Licensed content publication:	Journal of Computational Physics
Licensed content title:	Spectrally-accurate algorithm for the analysis of flows in two-dimensional vibrating channels
Licensed content author:	S. Zandi, A. Mohammadi, J.M. Floryan
Licensed content date:	15 November 2015
Licensed content volume number:	301
Number of pages:	31
Start Page:	425
End Page:	455
Type of Use:	reuse in a thesis/dissertation
Portion:	full article
Format:	both print and electronic

Are you the author of this Elsevier article?	Yes
Will you be translating?	No
Title of your thesis/dissertation:	Flows in vibrating channels
Expected completion date:	Sep 2015
Estimated size (number of pages):	120
Elsevier VAT number:	GB 494 6272 12
Price:	0.00 USD
VAT/Local Sales Tax:	0.00 USD / 0.00 GBP
Total:	0.00 USD

Curriculum Vitae

Name:	Sahab Zandi
Post-secondary Education and Degrees:	<p>University of Tehran Tehran, Iran 2009–2013 B.Sc. (Mechanical Engineering)</p> <p>The University of Western Ontario London, Ontario, Canada 2013–2015 M.Sc. (Mechanical Engineering)</p>
Honours and Awards:	Western Graduate Research Scholarship 2013–2015
Related Work Experience	Teaching & Research Assistant The University of Western Ontario 2013–2015

Publications (Journals):

Zandi, S. & Floryan, J. M. (2015). Pressure Losses in Vibrating Channels. In preparation for submission to the *Journal of Fluid Mechanics*.

Zandi, S., Mohammadi, A. & Floryan, J. M. (2015). Spectrally-Accurate Algorithm for the Analysis of Flows in Two-Dimensional Vibrating Channels. *Journal of Computational Physics* 301, 425–455, DOI: 10.1016/j.jcp.2015.08.025.

Publications (Conferences):

Zandi, S., Mohammadi, A. & Floryan, J. M. (2015). On the Analysis of Flows in Vibrating Channels. *68th Annual Meeting of the American Physical Society Division of Fluid Dynamics*, November 22–24, Boston, Massachusetts, USA, Bul. Amer. Phys. Soc., v.60, No.21.

Zandi, S., Mohammadi, A. & Floryan, J. M. (2015). Spectral Algorithm for Analysis of Flows in Vibrating Channels. *Proceedings of the 25th Canadian Congress of Applied Mechanics (CANCAM 2015)*, May 31–June 4, London, Ontario, Canada.

Zandi, S. & Floryan, J. M. (2015). Drag Reduction in Channels with Vibrating Walls. *Thousand Islands Fluid Dynamics Meeting (TIM 2015)*, May 1–3, Gananoque, Ontario, Canada.